

MEMORIAL BRIDGE HYDROKINETIC POWER GENERATION: VFG & GHT

*Eryka Black, Daniel Kupferschmid, Timothy Osborn,
Taylor Smith & Matthew Wilkening
Ocean Projects TECH 797
Project Planning and Design CIE 784/788
University of New Hampshire
College of Engineering and Physical Sciences
April 29th, 2013*

ACKNOWLEDGEMENTS

This work is the result of research sponsored in part, by the New Hampshire Sea Grant College Program through NOAA grant # NA10OAR4170082, and the UNH Marine Program.

Our team would like to thank the entirety of the Ocean Engineering, Mechanical Engineering and Civil Engineering Departments at the University of New Hampshire, with a special thanks to Dr. Kenneth Baldwin, Dr. Martin Wosnik, Dr. Barry Fussell, Dr. Erin Bell, Dr. Larry Harris, Michael deLeon, Pete Bachant, and Dr. Yannis Korkolis for their time, advice, and support.

We also wish to thank Ben Brickett, and his wonderful employees for aiding us in our experiment on such short notice out of the kindness of their hearts. As well as New England Wire Technologies for donating material, equipment, and time to make this project possible.

ABSTRACT

Hydrokinetic power constitutes the greatest portion of “green energy” production, at 35% of all green energy production as of 2011 in the United States. However, hydrokinetic power is fading as a power source relative to other sources in the US. The United States may be slowly lagging behind the rest of the world in terms of hydro production, however micro siting hydrokinetic turbines in the hidden gems of energy in the world may help to bring hydropower in the US back to the top, and underneath the Memorial Bridge may be one of such gems.

In order to capture the hydrokinetic power from the Piscataqua River, A turbine was selected to convert power from the water into mechanical shaft power, and a new type of electrical generator was investigated. The generator which was analyzed was a variable flux generator (VFG). The type of turbine which was selected was a Gorlov helical turbine (GHT). The turbine had a diameter of 1 m, a height of 1.32 m, a NACA0020 blade profile, a cord length of 14 cm, a solidity of .14, and a blade overlap of .5.

Some of the generator characteristics were unable to be solved for due to “real life” issues, however, the force vs. engagement profile over an engagement distance of 0 to 1.5 in was found for a generation 1 VFG with 6 cores and 6 magnets. Torque, RPM, current, voltage, and resistance were measured over a RPM range of 50 to 100 RPM at an engagement of 1 in. It would have been preferable for data to have been collected over engagement distances ranging from 0 to 1.5 in, and with RPMs ranging from 0 to 150 RPM assuming a 1 to 1 gear ratio between the turbine and the generator.

It was determined that, assuming a power requirement of 12 MW hours/year, the turbine which was chosen would be able to meet 48% of the bridge’s power requirements, assuming operation at maximum efficiency and neglecting electrical losses. It is strongly recommended that at least three turbines are used underneath the bridge in order to meet the yearly energy requirement.

TABLE OF CONTENTS

Acknowledgements	2
Abstract	3
Table of Contents	3
List of Figures	6
1 Introduction	8
2 Project Background	9
3 Fall Semester	12
3.1 Initial Analysis	12
3.2 Design Modification.....	13
3.2.1 Turbine Selection	13
3.2.2 Turbine Design.....	13
3.2.3 Turbine Support Structure.....	13
3.2.3a Material Properties.....	13
3.2.3b Biofouling	13
3.2.4 Variable Flux Generator	13
3.3 Static Magnetic Force Experiment.....	19
3.3.1 Objectives.....	19
3.3.2 Summary Of Results.....	19
3.3.3 Theory	20
3.3.4 Experimental Methods	22
3.3.5 Results and Discussion	25
4 Spring Semester	28
4.1 Revised Method of Engagement	28
4.2 Bench Test Experiment	30
4.2.1 Objectives.....	30
4.2.2 Theory	30
4.2.2a Applying Maxwell's Field Equations to this Geometry	32
4.2.2a Calculating the Voltage.....	35
4.2.3 Experimental Methods	37
4.2.4 Results and Discussion	42
4.3 Support Structure Analysis.....	45
4.3.1 Finding the Forces and Loads.....	45
4.3.2 Geometric Constraints	47

4.3.3 Designing the Frame.....	48
4.3.3a Maintenance Platform	49
4.3.3b Trapezoidal Frame.....	50
4.3.3c Sizing of the Beams	52
4.3.3d Beam Deflection.....	53
5 Future Work.....	55
6 References	57
7 Appendices	58
7.1 Data Tables	58
7.2 Equipment List.....	60
7.2 Sample Calculations	67
7.2 Solidworks Drawings	77

LIST OF FIGURES

FIGURE 1: UNH TIDAL ENERGY TEST SITE WATER VELOCITY PROFILE.....	9
FIGURE 2: MEMORIAL BRIDGE WATER VELOCITY PROFILE.....	9
FIGURE 3: MEAN POWER DENSITY MEASURED IN W/m^2 FOR WATER DEPTHS RANGING FROM 1.55 TO 17.53 M BELOW WATER SURFACE. THE HIGHEST MEAN POWER DENSITY EXISTS AT A WATER DEPTH OF 6.55 M.....	10
FIGURE 4: PROPOSED STRUCTURE SIDE ELEVATION WITH STEEL PILINGS.....	11
FIGURE 5: FIXED PITCH PROPELLER (LEFT) AND KAPLAN (RIGHT) REACTION TYPE TURBINES.....	13
FIGURE 6: TURGO (LEFT) AND PELTON (RIGHT) IMPULSE TYPE TURBINES.....	14
FIGURE 7: EXAMPLES OF SOME OF THE VARIOUS TURBINES RESEARCHED DURING THE TURBINE SELECTION PROCESS.....	15
FIGURE 8: ELEVATION VIEW OF THE TURBINE.....	16
FIGURE 9: LOCATION OF THE TRANSFER PLATE ON THE PIER.....	16
FIGURE 10: OUTPUT FORCE [LBS] VS. ENGAGEMENT LENGTH [IN].....	20
FIGURE 11: MAGNETO-RESISTIVE CIRCUIT OF THE SYSTEM.....	21
FIGURE 12: MODEL OF THE THEORETICAL SYSTEM.....	22
FIGURE 13: BIRD'S EYE VIEW OF THE MEASUREMENT DEVICE.....	23
FIGURE 14: SIDE VIEW OF MAGNET ENGAGED WITH THE YOKE/CORE.....	24
FIGURE 15: SCHEMATIC OF THE SETUP, SHOWING THE ENGAGEMENT DISTANCE (A) AND YOLK HEIGHT (B) THAT WERE CONTROLLED.....	24
FIGURE 16: CALIBRATION CURVE OF 100 LB LOAD CELL.....	25
FIGURE 17: COMPARISON OF THEORETICAL AND EXPERIMENTAL FORCES. NOTE THE DISCREPANCY IN RATE OF FORCE DROP OFF.....	25
FIGURE 18: OUTPUT FORCE [LBS] VS. ENGAGEMENT LENGTH [IN] WHERE HEIGHT DIFFERENCE IS 0.23 IN.....	26
FIGURE 19: OUTPUT FORCE [LBS] VS. ENGAGEMENT LENGTH [IN] WHERE HEIGHT DIFFERENCE IS 0.48 IN.....	27
FIGURE 20: OUTPUT FORCE [LBS] VS. ENGAGEMENT LENGTH [IN] WHERE HEIGHT DIFFERENCE IS 0.52 IN.....	27
FIGURE 21: OUTPUT FORCE [LBS] VS. ENGAGEMENT LENGTH [IN] WHERE HEIGHT DIFFERENCE IS 0.645 IN.....	28
FIGURE 22: SCHEMATIC OF THE PROPOSED ACTIVATION MECHANISM.....	29
FIGURE 23: GENERIC MAGNETIC MODEL DESCRIBING THE PATH OF MAGNETIC FLUX.....	31
FIGURE 24: SCHEMATIC OF MAGNETIC MODEL.....	32
FIGURE 25: DESCRIPTION OF THE CROSS SECTIONAL AREA OF THE GAP.....	33
FIGURE 26: A) ASSEMBLED VIEW OF ADAPTER. B) EXPLODED VIEW OF ADAPTER.....	37
FIGURE 27: A) ASSEMBLED VIEW OF BRONZE SLEEVE. B) EXPLODED VIEW OF BRONZE SLEEVE.....	37
FIGURE 28: LINEAR ENGAGEMENT WAS PROVIDED BY THE COMBINATION OF THE PINS AND THE KEYWAY.....	38
FIGURE 29: A) ASSEMBLED VIEW OF ADAPTER WITH ROTOR, DRIVE SHAFT, BALL BEARINGS, AND REQUIRED HARDWARE. B) EXPLODED VIEW OF FIGURE 29.A.....	39
FIGURE 30: EXPLODED VIEW OF MAGNETS IN MAGNET MOUNTS ABOUT THE ROTOR.....	40
FIGURE 31: EXPERIMENTAL SETUP FOR MEASURING FORCE AT DIFFERENT ENGAGEMENTS.....	41
FIGURE 32: EXPERIMENTAL SETUP OF BENCH TEST PROCEDURE.....	41
FIGURE 33: DATA ACQUISITION BOARD THAT ALLOWED FOR DATA TO BE RECORDED.....	42
FIGURE 34: LVDT CALIBRATION.....	42
FIGURE 35: AVERAGE INPUT POWER FOR ENGAGEMENT OF 1 INCH.....	43
FIGURE 36: AVERAGE POWER GENERATED BY THE VFG AT 1 INCH DISENGAGEMENT.....	43
FIGURE 37: AVERAGE VFG EFFICIENCY FOR 1 INCH DISENGAGEMENT.....	44
FIGURE 38: TORQUE (Nm) MEASURED AT EACH OF THE 5 RPM SPEEDS OVER 1 SECOND TIME INTERVAL.....	44
FIGURE 39: WATER VELOCITY PROFILE BENEATH THE MEMORIAL BRIDGE.....	45
FIGURE 40: POWER DENSITY VS. DEPTH.....	47
FIGURE 41: HEIGHT CLEARANCE OF THE PIER CAP TO THE BRIDGE.....	48
FIGURE 42: PLAN VIEW OF THE STRUCTURE.....	48
FIGURE 43: ELEVATION VIEW.....	49
FIGURE 44: PLAN VIEW OF THE TRAPEZOIDAL FRAME.....	49
FIGURE 45: 3D MODEL OF THE TURBINE STRUCTURE.....	50
FIGURE 46: TURBINE LOAD.....	51
FIGURE 47: WATER LOAD.....	51
FIGURE 48: GENERATOR LOAD.....	52
FIGURE 49: MID-FRAME MEMBER SIZES.....	52

FIGURE 50: TOP-LEVEL MEMBER SIZES.....	53
FIGURE 51: DEFLECTED SHAPE DUE TO WATER LOADING.....	54
FIGURE 52: DEFLECTED SHAPE DUE TO TURBINE LOAD.....	54
FIGURE 53: SCHEMATIC OF GORLOV TURBINE SHOWING ANGLE OF TWIST.....	55

1 INTRODUCTION

The goal of the Memorial Bridge project is to deploy a hydrokinetic turbine beneath the Memorial Bridge in the Piscataqua River in Portsmouth, New Hampshire to siphon electrical power from the water beneath the Memorial Bridge. The mechanical energy harvested by the turbine will provide electrical energy to the various power needs of the bridge to ensure its safety, sustainability and security. To do this, there will be high-efficiency LED aesthetic, traffic, aerial, and marine navigation lighting. The power requirements to ensure the safety of the bridge are structural monitoring systems, performance sensors, data acquisition and communication. The bridge will be kept secure with surveillance cameras that monitor marine and homeland security needs. There will also be informational and educational monitoring and displays available at a kiosk on the New Hampshire side of the river. With all of these power needs, the assembly is required to generate 12 megawatt-hours yearly.

To generate this power, investigation of a turbine, support structure, and generator is vital. This entails selecting a suitable location for a turbine, selecting a proper type of turbine, designing housing for the turbine, and designing a power efficient generator.

The turbine type was selected based from research of common hydrokinetic turbines. Once the turbine type was selected, the position and size of the turbine was selected based from power density curves provided from last year's report. The turbine specifications were selected based from existing data taken from Peter Bachant and Martin Wosnik's experiments with crossflow turbines. Separately, a variable flux generator was designed and partially tested. The tests correlated RPM, torque, output voltage, current, and resistance. The objective of collecting a relationship between those parameters was to calculate the efficiency of the generator, apply the results to the power curves taken from Peter and Martin's experiments, and solve for a relationship between RPM and engagement distance which maximizes the electrical power output of the combined system. Eventually, a future senior project would be assigned to making a control system for the VFG using the parameters calculated by our experiment.

2 PROJECT BACKGROUND

Compared to wind and solar power, tidal power provides a more predictable source of renewable energy. Due to constant advances in tidal power technology, tidal energy is also becoming a more economically and environmentally appealing way of sustainably harvesting energy. With the improvements in the field of tidal energy, the idea of implementing this type of renewable energy source proves to be a good idea in both an educational and informational sense. Therefore, when given a chance to design and construct a hydropower system beneath the non-lifting New Hampshire side of the Memorial Bridge, a project was presented that held many great opportunities.

First of all, this location is ideal for tidal power generation. The Memorial Bridge is located over the Piscataqua River, which is a tidal estuary with one of the highest rated tidal flows in North America. And it is the only site in the area with enough flow to make power generation feasible, which is evident in the comparison of the water velocity profiles from the Piscataqua River and the UNH Tidal Energy Test Site between Newington and Dover. A comparison of the existing current velocities at both locations is shown in the figures below.

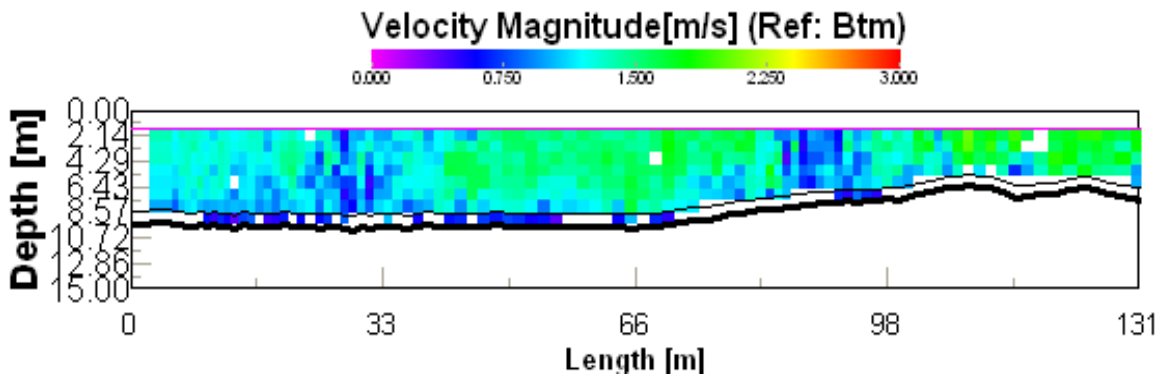


Figure 1: UNH Tidal Energy Test Site water velocity profile.

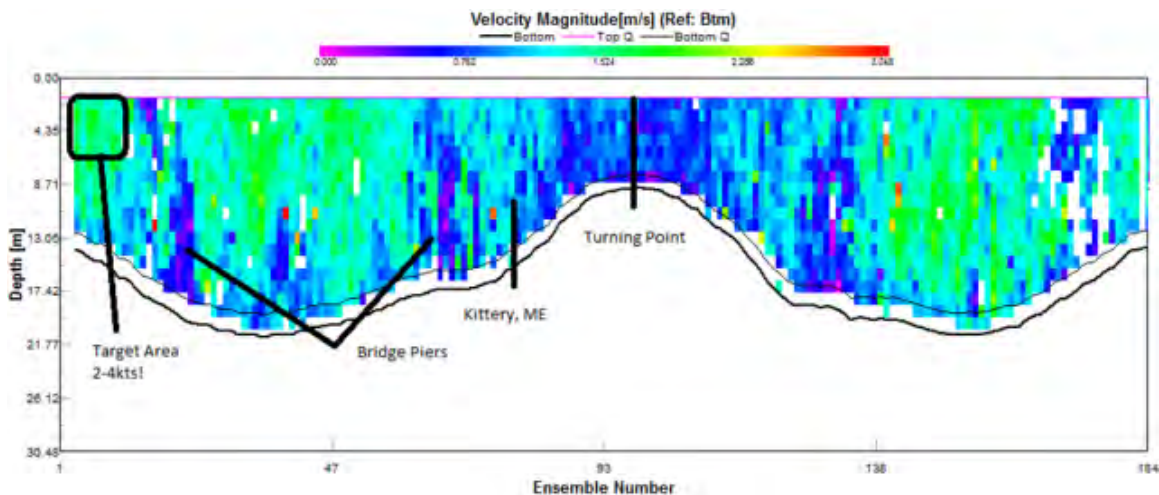


Figure 2: Memorial Bridge water velocity profile.

In addition to having more occurrences of higher flow velocities, the flow at the proposed turbine site is outside of the shipping lane. This provides an additional reason that makes this site so attractive.

Another reason that makes this project such an excellent opportunity is that the Memorial Bridge is in the process of being repaired. The New Hampshire DOT and Archer Western Contractors have both agreed to implement a transfer plate in the construction of the new pier cap. This simplifies the installation of a support structure by eliminating the need for additional construction if, in the future, it is decided to implement this hydropower system once reconstruction of the bridge is completed.

The goal behind having this tidal power generation is to make the Memorial Bridge self-sustaining. There are a variety of proposed sensors that will allow for weather data acquisition, structural monitoring of the bridge, and real-time data regarding the operation of the turbine system. The power generated by the turbine will power the sensors, monitoring equipment, and more noticeably the aesthetic lighting on the bridge.

The objective of the project is to show the public how this tidal energy will be used. When the aesthetic lighting is being powered by tidal energy, the lights will change color going from white to green. This will allow the public to visibly see when green energy is being used and will show how advanced and sustainable the bridge will be.

This was a project continued from spring of 2012, which provided a proposed hydrokinetic turbine support structure, as well as Piscataqua River current data. One of the useful diagrams from last year's report (shown below) provided the depths of the river that experience the highest power density. They also noted that the Piscataqua River has a flow greater than 2 knots (1m/s) approximately 2/3 of the time. This information was considered to be very important when it was time to select a turbine.

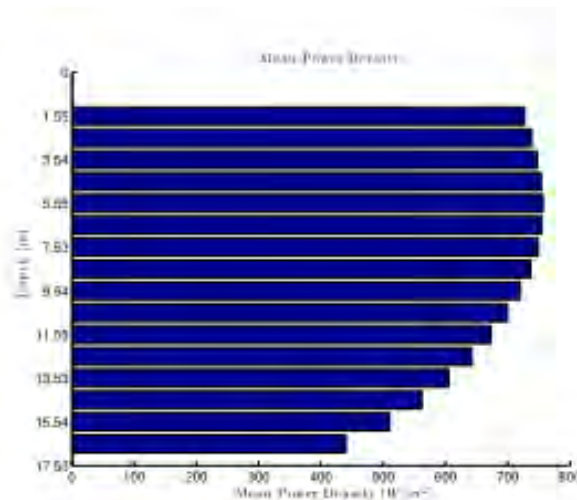


Figure 3: Mean power density measured in W/m^2 for water depths ranging from 1.55 to 17.53 m below water surface. The highest mean power density exists at a water depth of 6.55 m.

The report also included proposed designs for modular encasements to house FFP axial flow rim-mounted direct-drive turbines. The turbine supporting structure was initially suggested to encase three turbines in modular boxes shown in the following figure.

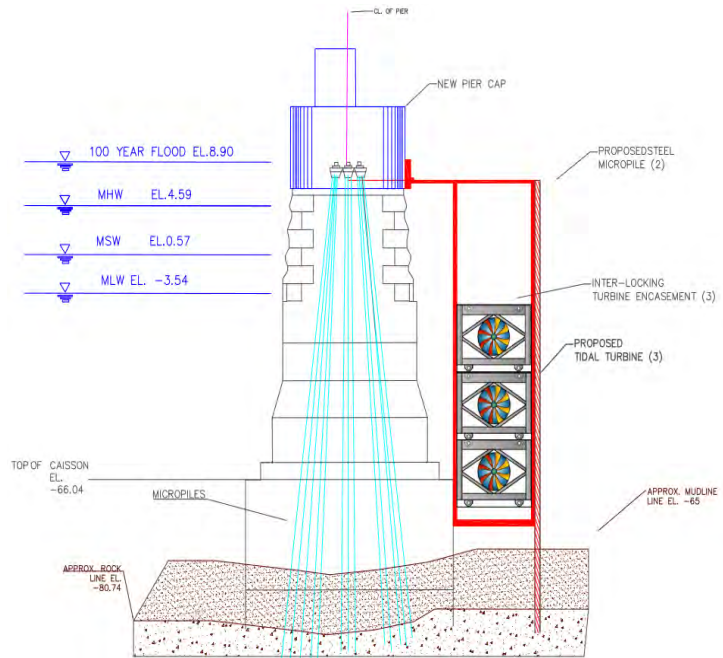


Figure 4: Proposed structure side elevation with steel pilings.

Though this design was thorough, it would only allow for the turbines to spin when subjected to unidirectional flow. This one-dimensional turbine operation proved to be a problem given that the current passing underneath the Memorial Bridge is bidirectional. This proposed turbine housing structure was altered to eliminate this problem with the additional research and design performed by this year's team, which will ultimately provide a solid stepping stone for the group that inherits this project in the future.

3 FALL SEMESTER

3.1 INITIAL ANALYSIS

The Memorial Bridge Hydrokinetic Power Generation report from last year neglected to propose a process of harvesting the mechanical energy provided by the hydrokinetic turbine and converting it into electrical energy. However, their report provided useful data regarding the Piscataqua River flow conditions at the proposed bridge pier location of the turbine, which helped to determine the necessary steps to reach the projects goal.

One of the initial objectives included determining a detailed final design of the proposed support structure complete with dimensions that agreed with the existing mounting capabilities. This would involve determining any impacts on the surrounding bridge structure such as loads and drag estimates on the structure, as well as determining the location of electrical and sensor cables. Another objective was to investigate the most efficient deployment of the turbines. This would require the selection of a turbine that would meet the existing site conditions and have the capability of generating the power necessary to operate the bridge's aesthetic lighting, traffic/aerial/marine navigation lighting, bridge safety monitoring, surveillance cameras, and informational/educational monitoring/displays. Once the proper turbine was selected, it would need to be sized based on mean power density of the flow over the range of highest power density, and coefficient of performance of the turbine. From this sizing, the angle of twist and factor of safety can be found (using the amount of power required).

Once these goals were met, the next step would be to construct a physical scale model of the bridge pier and turbine frame and establishing a means to tow the model in the UNH Tow Tank to provide response behavior for the full scale design. The best way to test the structure's response would require the model to match the Reynolds scaling of the actual design (which would determine the towing velocity). This could be done by analyzing the mean power density over a water depth range with the highest power density (relative to the turbine height) while taking blockage into account. The Tow Tank experiment would also require the team to find the best way of actuating the generator with less than one inch engagement using either hydraulics (i.e. hydraulic governor/accumulator or pump) or a hydrofoil lifting mechanism. Engaging the generator's magnets using these methods would require knowledge of the force on the magnets with respect to engagement to be known.

With all of this analysis complete, the placement of the performance sensors on the turbine structure could be decided. These sensors provide for real time data acquisition at a nearby kiosk that will measure turbine performance, electrical output, local current velocity, turbine rpms, and underwater surveillance cameras showing the turbine from different angles.

To meet each of these five objectives, the plan of action for the project team was outlined. The first step was to decide the elevation of the turbines by researching the location of regions with the most energy density provided by last year's report (shown in Figure 3), the EPRI current report, and 2007 Piscataqua current data provided by NOAA. Next, calculations of the drag forces on the support structure and the hydrokinetic turbines were to be performed. This was then followed by researching experiments involving the study of bridge piers in a tow tank and measuring the loads on the frame at critical locations. Finally,

we sought to incorporate methods of enhancing the turbine's ability of harnessing of tidal energy into the new bridge pier design. The final step in this plan was to build an electric generator for the turbine in order to convert the mechanical energy into electrical energy.

3.2 DESIGN MODIFICATIONS

As stated briefly in the introduction, the turbine encasement design was altered. The design was based off of using free flow power (FFP) axial flow rim-mounted direct-drive turbines. However, it was found that free flow power is undesirable because requires a large support structure, unidirectional flow, and submerged generators, which would require waterproof encasement that is known to be extremely expensive. Therefore, the design process began with selecting a turbine which would ultimately decide the necessary turbine support structure as well as the placement of the generator.

3.2.1 TURBINE SELECTION

Many hydrokinetic turbines were researched and compared to choose the best turbine to meet the power requirements based on the site's existing conditions. Turbines are classified into three specific categories: fixed pitch propeller/Kaplan, Turgo/Pelton, and cross-flow turbines. The first category consists of reaction turbines that are frequently used in low head with high speed and unidirectional flow requiring full submersion. Some examples of the reaction turbine are inclined axis, floating mooring and rigid mooring turbines. None of these were selected because they all have an axial flow orientation, spinning only when facing parallel to the direction of flow, meaning they will only work well in a unidirectional flow.

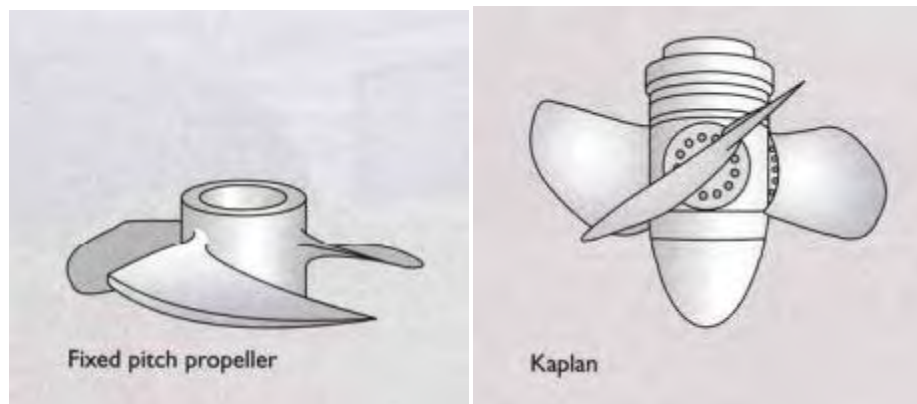


Figure 5: Fixed pitch propeller (left) and Kaplan (right) reaction type turbines.

Turgo and Pelton are impulse turbines used in medium or low head, low flow speeds, and unidirectional flow while only needing to be partially submerged. This type of turbine is also relatively inexpensive to maintain.

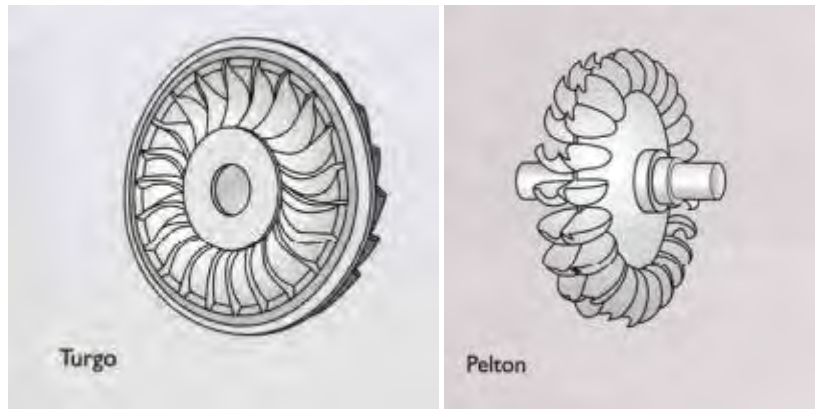


Figure 6: Turgo (left) and Pelton (right) impulse type turbines.

Finally, cross-flow type turbines may be implemented in a wide range of flow head and speed types. They are also capable of operating fully submerged, and always rotate the same direction regardless of the flow direction. Of these three classifications of turbines, the cross-flow turbine variants were selected. While the reaction type turbine were recommended from previous year's reports, it was found that the increased efficiency of those types of turbines were more than compensated for by the increase of capacity factor of the cross-flow turbines. The impulse turbines were not selected because they generate power from the surface of the water; however, the power density of the water is greater at deeper parts of the river. Furthermore, impulse turbines have a limited swept area because they are only partially submerged, which further decreases power output.

With the cross-flow turbine type selected, the next step was to choose a specific cross-flow turbine. The Darrieus and H-Darrieus turbines do not generate enough power. The Darrieus type turbine is self-limiting, which means it will not exceed its maximum rated speed. This turbine can also have problems during startup depending on the position of the hydrofoils relative to the flow direction. Though it has more structurally sound foils, their curved blades make for a lower efficiency. This turbine is ordinarily used for wind power generation under circumstances where efficiency is not relevant but safety is (such as monitoring weather conditions). While the H-Darrieus is more efficient than the Darrieus turbine, it also suffers from startup issues. However, unlike the Darrieus, it is less structurally sound, the H-Darrieus turbine does not benefit from being self-limiting, unlike the Darrieus turbine.

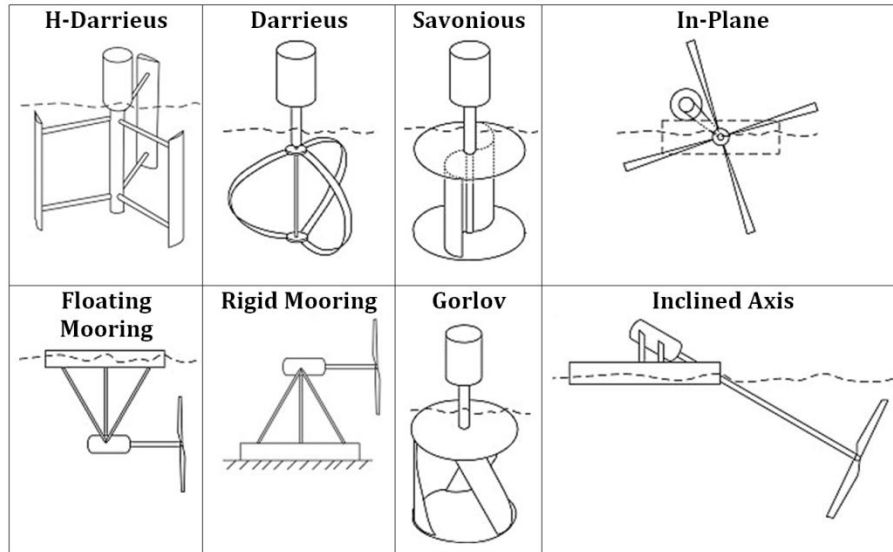


Figure 7: Examples of some of the various turbines researched during the turbine selection process.

The Savonius cross-flow type turbine is a relatively simple design that is generally less expensive than most other cross-flow options. However, through comparison the Savonius is not as efficient as other cross-flow turbines, has potential startup problems, and more importantly, is a drag based device that would put an overwhelming amount of strain on the bridge in order to operate effectively. The Gorlov helical turbine (GHT) is nothing more than an H-Darrieus turbine with curved blades. Its omnidirectional simplistic design has the benefit of transmitting a uniform torque to the shaft, which benefits both the lifespan of the shaft and also allows the power produced by the generator to be more uniform in amplitude. Though this turbine tends to be less structurally sound than other turbines, due to the oscillation of the position of maximum torque along the blades as the turbine spins, and is also more expensive to manufacture, it is the only turbine which was researched that does not have difficulty starting up under any circumstances.

Of these four cross-flow type turbines, the Gorlov helical turbine stood out as the most preferable option. The need for a turbine that does not require any additional components to begin rotating quickly became apparent during the research process. While the simplicity and safety of the Savonius and Darrieus turbines were desirable, efficiency was deemed more important than any other aspect of the turbine. Therefore, the Gorlov helical turbine was chosen as the turbine to be used underneath the Memorial Bridge.

3.2.2 TURBINE DESIGN

Research proved a three blade Gorlov to be the most suitable design. These blades are often made from a strong and lightweight composite material resistant to salt water, usually either fiberglass or aluminum, and can also be hollow. The material proposed for this turbine was suggested to be aluminum with a possible salt water resistant coating. With a 2.5m high by 1m diameter Gorlov helical turbine available in Chase Hall for testing, this was used to temporarily size the turbine to be used beneath the bridge, centered at a water depth of 6.55m (where the mean power density is highest).

There were other design features that were not implemented into the design due to either lack of information available (seen often in patents, in which the idea is shown but the full description of its benefits is not explained) or time constraints. The first of which was the cylindrical distributor, which is mounted for rotation with the turbine shaft and concentrates the flow field near the hydrofoils. It was said to apparently increase turbine efficiency but little other information about its downfalls was found. Another consideration was to design for multiple turbines with plural shafts. This usually involves either using multiple generators that are individually associated with each of the turbines or connecting the shafts via suitable transmission to a single generator (single rotor combination). To implement either of these into the turbine design would increase design complexity and was ultimately found to be an unrealistic design. Also looked into was Catamaran installation, which is a vessel enclosing a turbine that rises and falls with fluctuating water levels to ensure that the turbine remains in the area of greatest velocity. This idea was not pursued further due to reasons similar to those listed for the plural shaft design.

3.2.3 TURBINE SUPPORT STRUCTURE

When given the opportunity to design a tidal turbine structure off of the Memorial Bridge pier, existing parameters were provided from Dr. Erin Bell and the NHDOT.

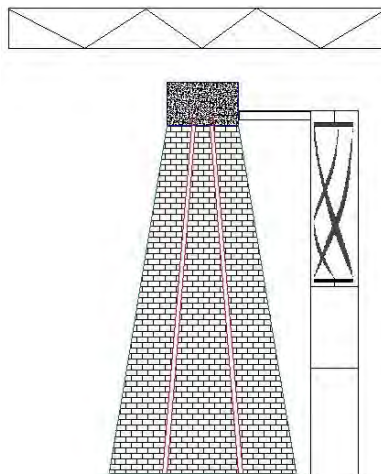


Figure 8: Elevation view of the turbine.



Figure 9: Location of the transfer plate on the pier.

As you can see in Figure 8, the red micro piles go through the pier up to the pier cap. During construction, the NHDOT, in conjunction with Archer Western, has offered to provide anchorage for the frame support by attaching a transfer plate to the pier. There will be rebar attached to the micro piles, which will then be attached to a green transfer plate for future work. With the addition of this transfer plate as shown in Figure 9, there will be no drilling into the pier which would cause an effect on the strength of the pier.

The NHDOT had also given our team information about the connection to the base of the water bed. There will be a pin connection to the bottom of the rock line. The pin connection will guarantee less environmental issues within the river bed. There will be minimum sediment disturbance when compared to drilling a foundation for the support.

3.2.3a MATERIAL PROPERTIES

When deciding what material property to use for the frame, A36 mild steel and T6 aluminum were compared. The factors that were taken into effect were the yield strength (in units of psi), modulus of elasticity (in units of ksi), as well as the corrosion of the material. The yield strength of a material is the stress at which a material will begin to deform plastically. Before the material reaches its yield strength, it will deform elastically and will return to its original shape when the applied stress is removed. Modulus of elasticity is the tendency of an object to deform elastically when a force is applied to the material. A stiffer material will have a higher modulus of elasticity. The following table shows these properties for the two of the materials considered.

Table 1: Comparison between A36 Steel vs. T6 Aluminum.

	A36 Steel	T6 Aluminum	Comparison
Yield Strength (psi)	36,000	35,000	Too small of a difference to compare
Modulus of Elasticity (ksi)	29,000	10,100	T6 has a greater deflection. Not ideal for turbine structure
Corrosion Resistance	Rusts	Forms a protective layer.	Steel needs corrosion protection to prevent deterioration.

As you can see from Table 1, the yield strength of the aluminum and steel are very similar and does not affect the decision for the material property of the structure. The modulus of elasticity has a large difference which affects the decision. The idea for the frame structure was an open design that was capable of being supported with minimal bracing. The greater the modulus of elasticity, the less deflection the beam will have and the less bracing you will need within the structure.

Through this comparison, steel was chosen to be used as the material for the frame design of this structure. It was also decided that zinc coating will be added to the steel as to protect it from corrosion. Therefore, when deciding the material, corrosion was not a large deciding factor. However, A36 Steel alone does have a high corrosion rate especially when the steel is submerged in seawater. Seawater has a high in salt content in the form of various chlorides. Typical surface seawater has a pH of 8 due to excess amounts of carbonates. The depth of

the water also plays a part in the pH levels, for instance, the pH decreases with depth so the pH will be high at most locations on the frame.

The entire structure of the new Memorial Bridge will be built from steel that is naturally resistant to rust, which is different from the steel used in the old bridge. Although, any steel placed in the maritime environment is subject to corrosion. The new bridge will be galvanized with a high percentage zinc coating. This is the same method that will be used for the turbine frame design. The table below shows that the American Galvanizers Association (AGA) has found the corrosion of zinc and zinc-coated steel in sea water.

Table 2: Corrosion of zinc and zinc-coated steel in sea water.

Location and Water	Type of Zinc	Type of Test	Years	Corrosion Rate (µm/year)
New England Coast	99.1% zinc	Mean Tide Level	3	25
New England Coast	99.1% zinc	Immersion	3	16

From this table it can be noted that there is a higher corrosion rate at the tide level than deeper in the seawater. Since the turbine will be closer to the tide level, the amount of galvanizing added will need to be adjusted and it must be protected throughout the construction process.

3.2.3b BIO FOULING

Bio fouling, or biological fouling, is the accumulation of microorganisms, plants, algae, or animals on wetted surfaces. Bio fouling occurs everywhere but is most significant economically to the shipping industries, since high levels of fouling on a ship's hull significantly increases drag, which reduces the overall hydrodynamic performance of the vessel and increases the fuel consumption. Bio fouling has been considered as one of the precautions and an anti-fouling process for the structure will be used. Anti-fouling is the process of removing or preventing these accumulations from forming. There are two types of anti-fouling processes: non-toxic coatings and biocides.

Non-toxic coatings prevent attachments of microorganisms thus neglecting the use of biocides. These coatings are non-toxic because they are based on organic polymers and are ecologically friendly but have problems with mechanical strength and long term stability. The non-toxic coatings are mainly used on fast paced moving objects such as boats and thus are not recommended to be used for the turbine support structure.

Biocides are chemical substances that are able to deter or kill the microorganism's response for bio fouling. It is an anti-fouling surface coating that targets the microorganisms that initially create the biofilm, such as bacteria. The specific biocide chosen for this structure was a Tributyltin Moiety (TBT) Toxic because it is toxic to both microorganisms and larger aquatic organisms.

3.2.4 VARIABLE FLUX GENERATOR

The idea of using a variable flux generator (VFG) was proposed to perform the conversion of the mechanical energy harvested by the Gorlov helical turbine to electrical energy used to power the electrical needs of the bridge. The variable flux generator is a mechanism with the ability to increase the capacity factor of a turbine. It does this by allowing the turbine to spin in flow speeds that would ordinarily be below the cut in speed of the turbine (the speed at which the turbine stops spinning), which powers the generator. The variable flux generator also allows for less generator induced damping, making for an easier turbine startup. However, combining the VFG with the GHT is something no one has ever done before, so there was much time spent on researching both machines before being able to build a VFG test model to produce hard results. A hydrofoil actuating mechanism to initiate engagement was also considered at this time and is discussed in detail in section 4.1.

3.3 STATIC MAGNETIC FORCE EXPERIMENT

3.3.1 OBJECTIVES

The force vs. distance profile of a Neodymium 42 one inch cubic magnet and a steel yoke was measured over a distance of 0 to 1.5 inches between the magnet and yoke for varying heights of the yoke. For each of these heights, normal forces were measured so that frictional forces could be calculated. The yoke used was identical to the yokes used in the "Hydrokinetic Turbine Featuring Variable Flux Generation (VFG)" 2010 Tech 797 report.

The magnet was placed into Professor Fussell's modified measurement device. A yoke welded onto an aluminum bar was custom made to be compatible with this device. The design of this attachment allowed for the height of the yoke to be varied by changing the location of the nuts along the screws that held the yoke in place. A load cell was used to measure the magnetic attractive forces statically, in discrete intervals. The force measurements recorded provided graphs of force versus distance for the five different heights.

The results provided from this experiment will allow for forces to be determined at numerous levels of engagement which will aid in the modeling of a variable flux generator to be used with a hydrokinetic turbine off of the Memorial, Bridge in Portsmouth, NH.

3.3.2 SUMMARY OF RESULTS

Our objective was to gather data regarding the magnitude of the forces between the magnet and yoke for different levels of engagement and yoke heights. Therefore, our major results are graphs of the output force at the respective engagement distance, which ranged from 0 to 1.5 inches by 0.02 inch increments. A graph showing the attractive force measured for the corresponding engagement distance when the magnet was level with the yoke is shown below.

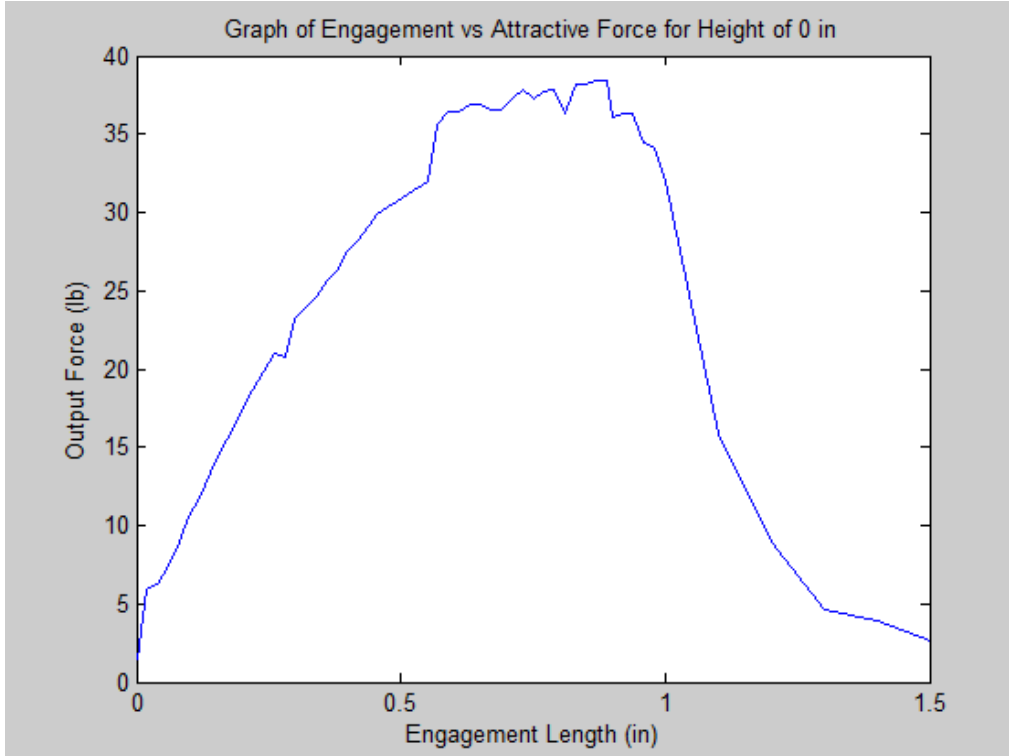


Figure 10: Output Force [lbs] vs. Engagement Length [in]

Note that the maximum force is about 47 lbs. This point occurs when the front surface of the magnet was approximately 0.8 inches from the front surface of the magnet. For each height the yoke was raised above the magnet, the length of engagement corresponding to the maximum force decreased by about 0.7 inches. It was also noted that the magnitude of the maximum force decreased as the height of the yoke increased. However, for all heights analyzed, the output force reduced exponentially to zero once the engagement length exceeded 1 inch. The graphical results composed agreed with our expectations.

3.3.3 THEORY

It was assumed that the magnet used was a Neodymium 42 magnet, one cubic inch in size with a magnetic flux density, B , field of 1.28 Teslas. The yoke was made of steel, and was assumed to have a gap length of 0 inches, a thickness of 1 inch, and a width of 3 inches. This brings the total width of one end segment of the “C” shape yoke to be 1 inch. The permeability ratio of the magnet (μ/μ_0) is assumed to be 1.05, the permeability of the steel yoke is approximately 0, and the permeability of air is assumed to be the permeability of free space ($4\pi \times 10^{-7}$). Assuming the above characteristics, a magnetic flux circuit was used to model the system Equations 1 and 2 given below.

$$\phi R_g + \phi R_g + \phi R_m = \frac{B \times L_m}{\mu_0} \quad 1$$

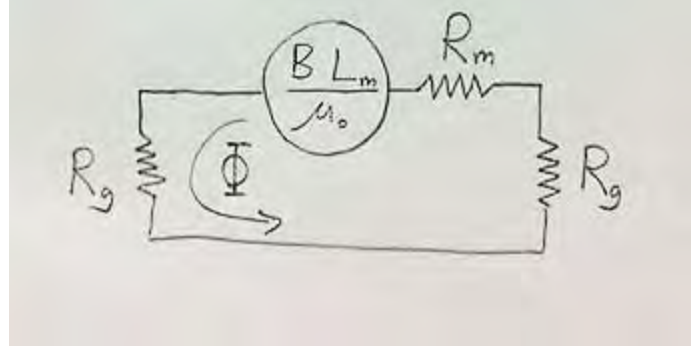


Figure 11: Magneto-resistive circuit of the system.

In the Equation 1, φ is the magnetic flux measured in Webers (Wb), R_g s are the resistances corresponding to the air gaps between the ends of the yoke and the poles of the magnet, R_m is the resistance of the magnet, B is the magnetic flux density of the magnet (1.28 T), L_m is the length the flux travels through the inside of the magnet, and μ_0 is the permittivity of free space.

$$F = -a_y \frac{\varphi^2}{\mu_0 S} \quad 2$$

F is the total force exerted by the magnet, $-a_y$ is the vector of the force (we only consider the force along the line intersecting the planes of symmetry of the yoke), and S is the area of a pole of the magnet.

The magnetic resistances can be expressed by the following two equations.

$$R_g = \frac{L_{avg}}{\mu_0 \times A_{yoke}} \quad 3$$

$$R_m = \frac{L_m}{\mu_0 \times A_{mag}} \quad 4$$

In Equations 3 and 4, A_{yoke} is the cross sectional area of the yoke, A_{mag} is the cross sectional area of the magnet, and L_{avg} is the average arclength travelled by the flux, which is approximated using "Ramanujan's arclength approximation":

$$C = \pi(3(a + b) - \sqrt{(3a + b)(a + 3b)}) \quad 5$$

$$L_{avg} = 0.7071 \times \frac{1}{4} C \quad 6$$

In the above equations, C is the circumference of an ellipse, "a" is the vertical radius of the ellipse, and "b" is the horizontal radius of the ellipse. The vector $-a_y$ was calculated assuming the force vector was oriented from the center of the outstretched portion of the magnet towards the center of the end segment of the yoke. Assuming "a" is half the length across one end of the yoke and "b" is the midpoint of the length of the outstretched magnet then $-a_y$ can be represented in scalar form as:

$$-a_y = \cos\left(\operatorname{atan}\left(\frac{a}{\frac{b}{2}}\right)\right) \quad b < a$$

$$-a_y = \cos\left(\operatorname{atan}\left(\frac{\frac{a}{2}}{b - \frac{b}{2}}\right)\right) \quad b > a$$

8

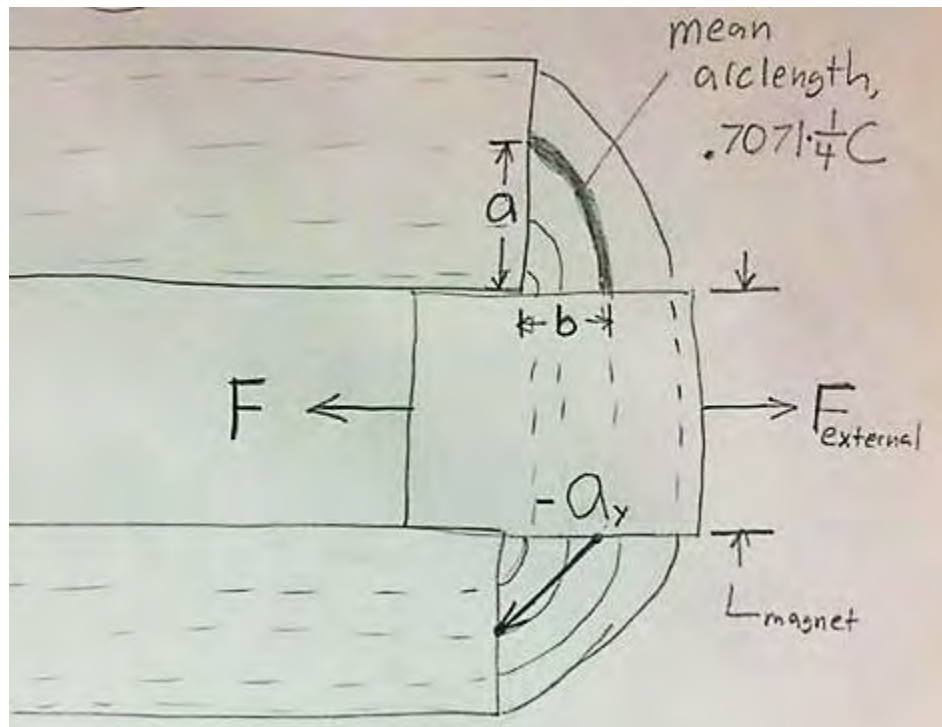


Figure 12: Model of the theoretical system.

The frictional force between the magnet and the yoke can be estimated using:

$$F_f = C_f \times N,$$

9

where F_f is the total force of friction, C_f is the coefficient of friction, and N is the normal force.

3.3.4 EXPERIMENTAL METHODS

An SMA load cell rated for 100 lbf was statically calibrated by hanging weights of a known mass with a string, or wire (for the heavier weights), over a range of 0 to 82 lbs. The weights used were measured using a scale we borrowed from Sheldon. Input voltage to the load cell was set to 10 V and output voltage was recorded using a digital multimeter. The load cell was then screwed into the device in the following figure.

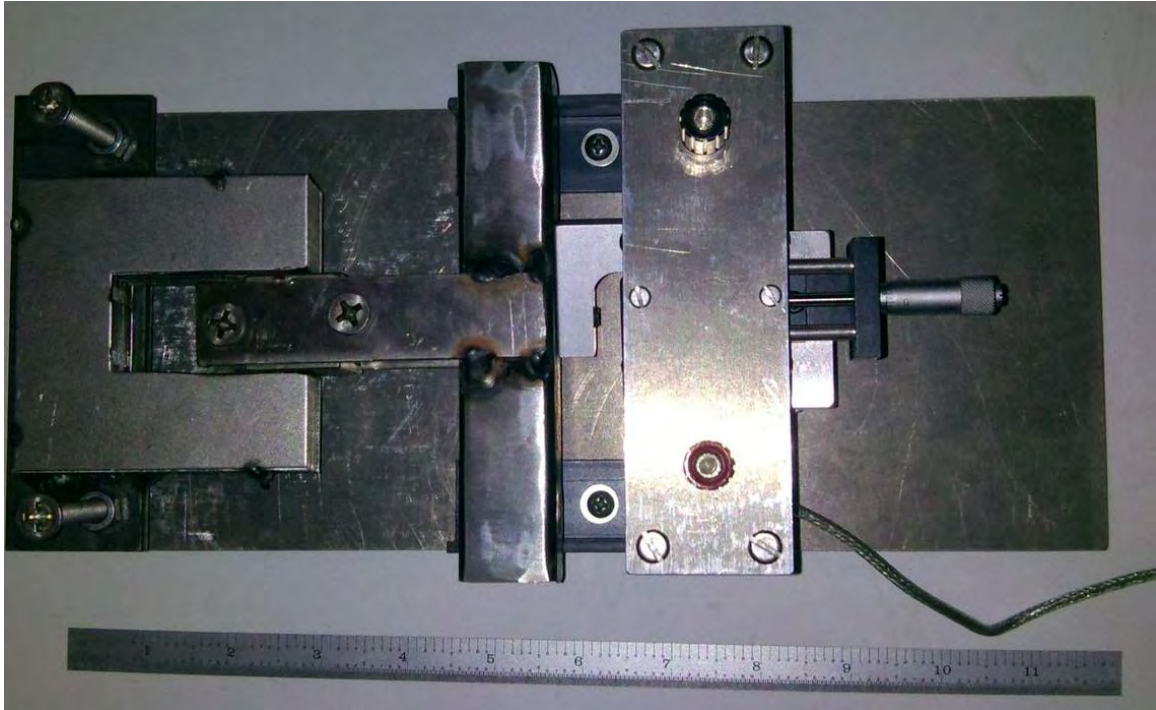


Figure 13: Bird's eye view of the measurement device.

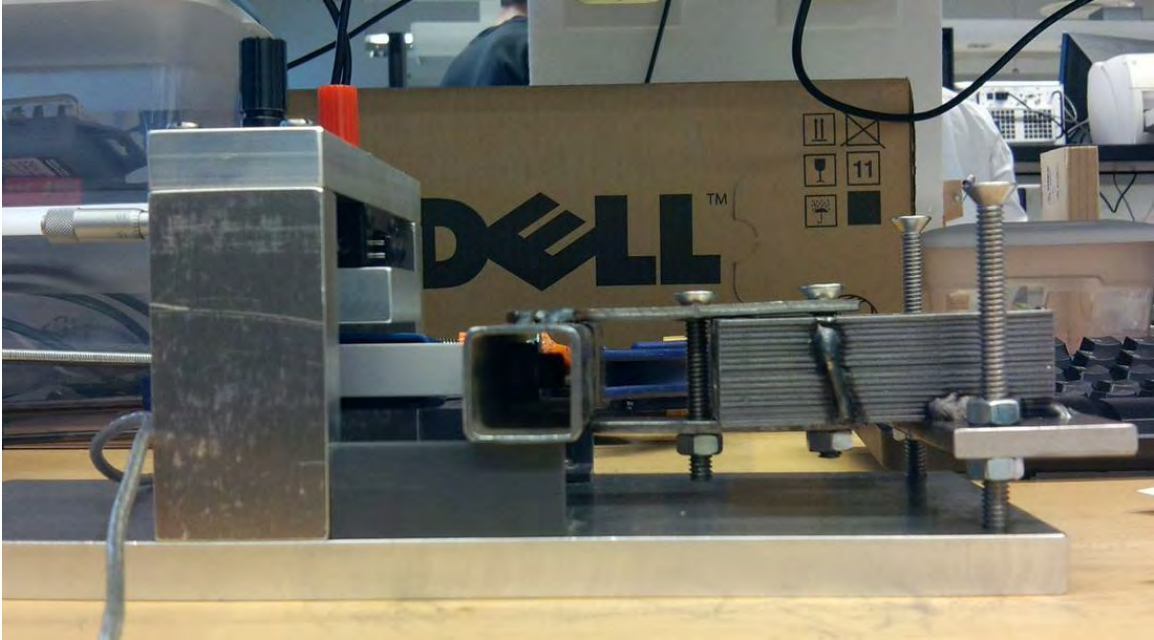


Figure 14: Side view of magnet engaged with the yoke/core.

At heights (B) of 0, 0.23, 0.455 and 0.52, the voltage across the load cell was measured for distances (A) between the outer edge of the magnet and the tips of the c-shaped core. These distances ranged from 0 to 1 inch by increments of 0.02 inches and 1 to 1.5 inches by increments of 0.1 inches. These two distances, A and B, are clarified in the following schematic.

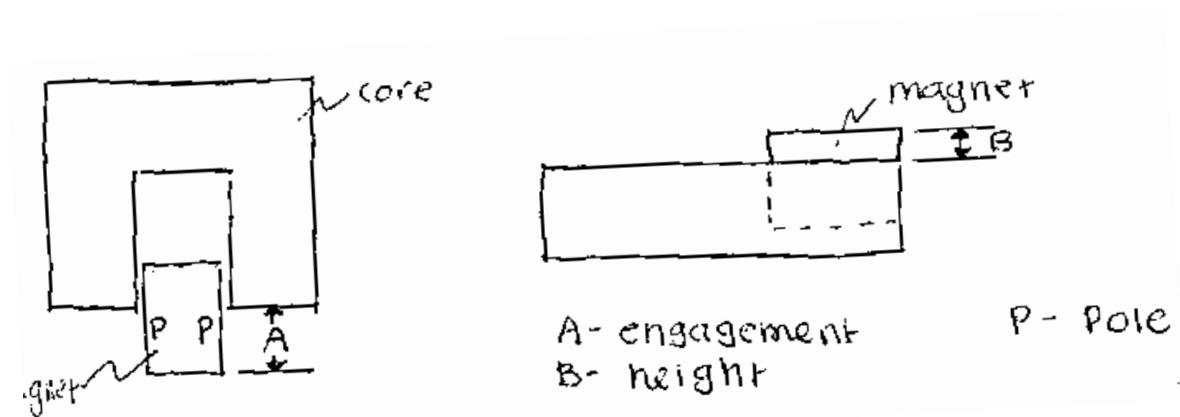


Figure 15: Schematic of the setup, showing the engagement distance (A) and yolk height (B) that were controlled.

Each time the magnet was set at a given height, a Chatillon mechanical force measurement device was pressed upon the end of a plank of wood which transmitted normal force to the magnet armature. Once enough force was applied, the magnet abruptly shifted horizontally from one side of the "C" core to the other. The forces recorded were used to calculate the frictional force between the magnet and steel.

3.3.5 RESULTS AND DISCUSSION

The load cell was statically calibrated using weights of a known mass over a range of 0 to 82 lbs, which covered the range of forces expected to be measured by the load cell in this experiment. The calibration data for the load cell is shown in the following figure.

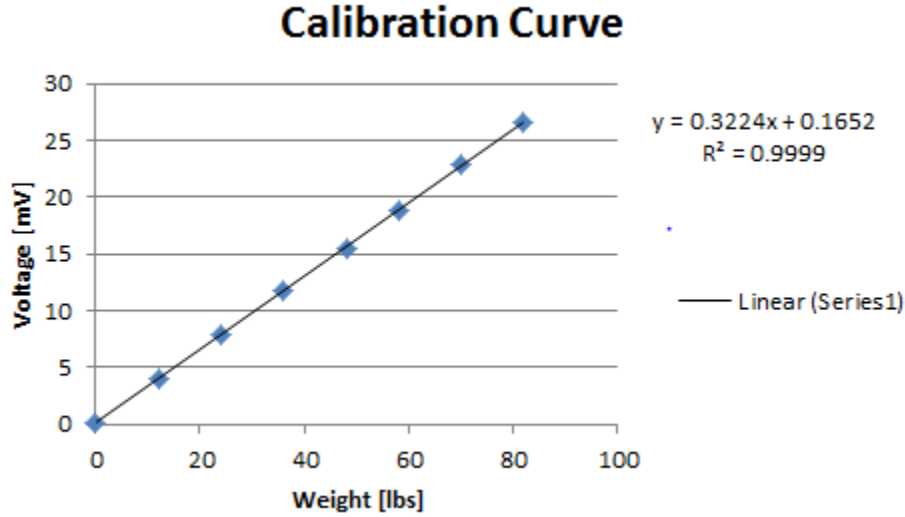


Figure 16: Calibration curve of 100 lb load cell.

This graph indicates that the sensitivity is 0.3224 mV/lb. The R^2 value is 0.9999, which indicates that the fit line accurately represents the data. Using this sensitivity, the raw voltage graphs were converted into graphs of engagement vs. attractive force.

The force vs. engagement graphs found experimentally, all have a similar shape to the theoretical force vs. engagement graph. While the shapes and magnitudes are similar, the time response of the theoretical prediction is significantly slower than what was seen from the experimental results, particularly when the magnet was completely outside of the yoke.

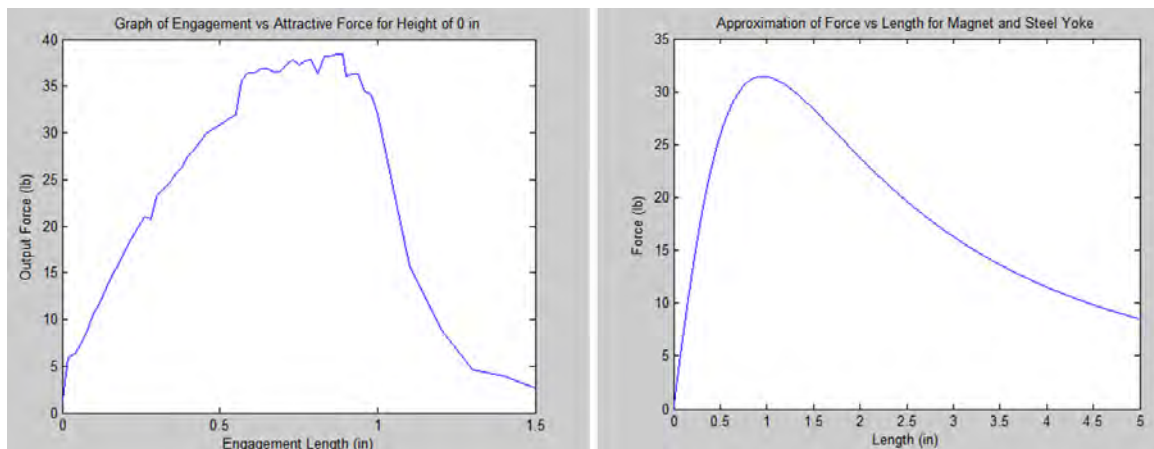


Figure 17: Comparison of theoretical and experimental forces. Note the discrepancy in rate of force drop off.

The reason the experimental time response was faster than the theoretical prediction is probably not due to experimental error, but it is more likely that the theoretical prediction

is inaccurate; experience with the experimental setup indicates that the force drop off is more similar to the experimental data than to the theoretical data. The reason why the theoretical plot is not accurate is most likely due to the difference in the force vectors from the one theoretical overall force vector.

The way the theoretical system was modeled, one overall force vector was meant to represent the total force on one pole of the magnet. However, this is not a good way to model the system because the individual force vectors from each magnetic molecule vary in both direction and magnitude. This variation causes the force vectors of the molecules that intersect the shorter, stronger lines of flux to be more angled in the direction of engagement. While the force vectors of the molecules that intersect the longer, weaker lines of flux are still angled in the direction of engagement, they are not angled as much as the force vectors of the molecules that intersect the shorter, stronger lines of flux. This discrepancy caused the theoretical prediction to be quite inaccurate.

The graphs for force vs. engagement length at different heights are shown below.

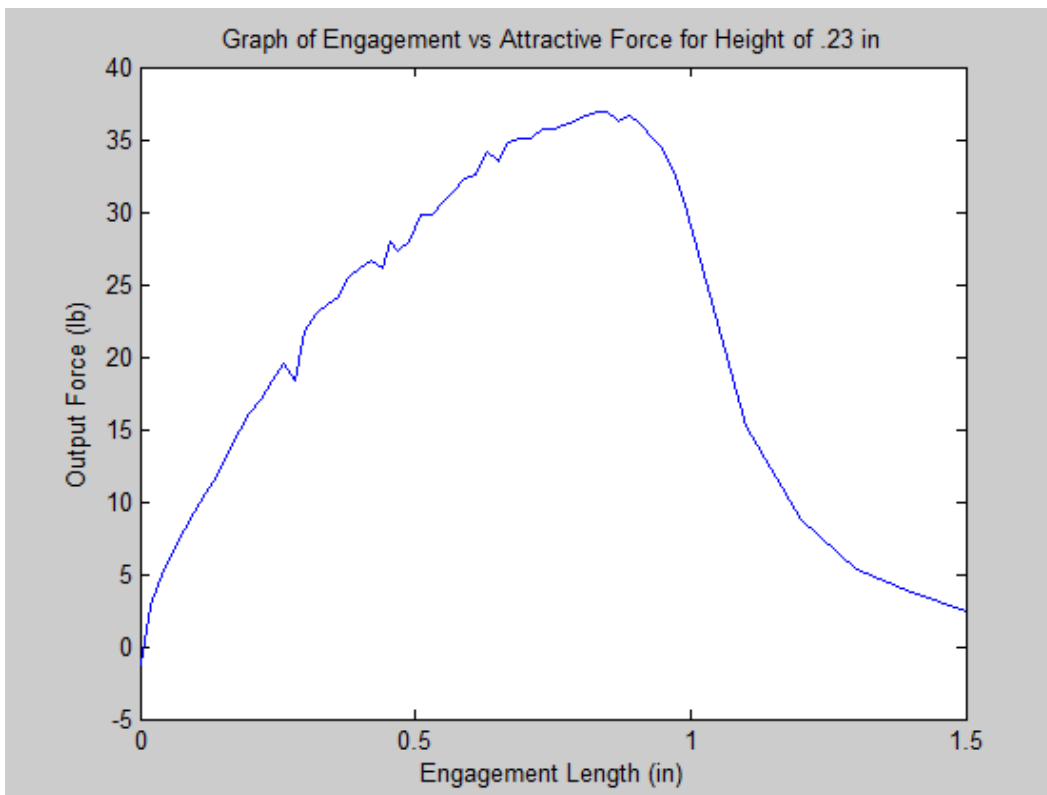


Figure 18: Output Force [lbs] vs. Engagement Length [in] where height difference is 0.23 in

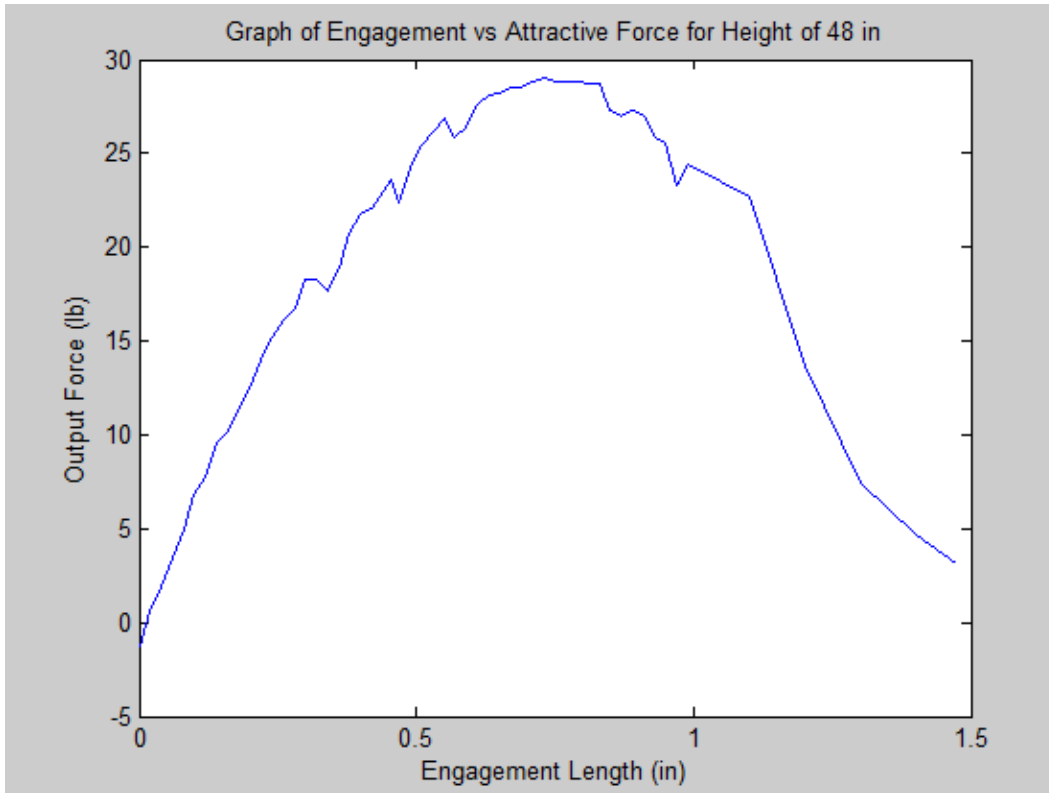


Figure 19: Output Force [lbs] vs. Engagement Length [in] where height difference is 0.48 in

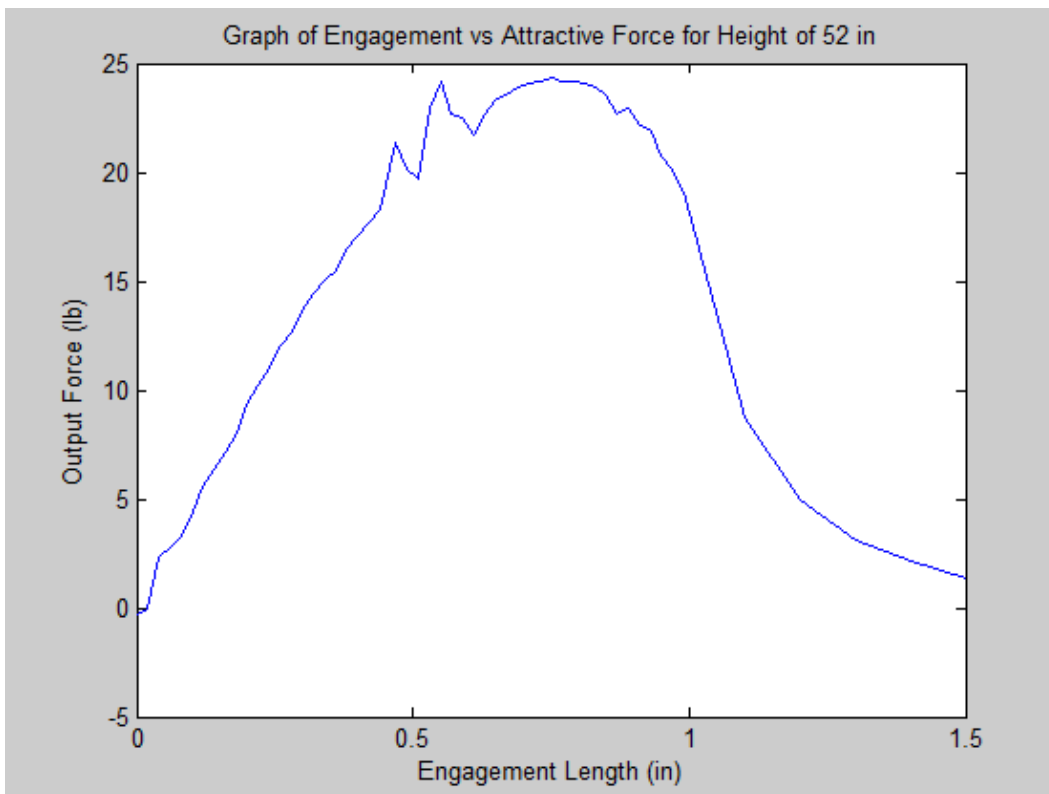


Figure 20: Output Force [lbs] vs. Engagement Length [in] where height difference is 0.52 in

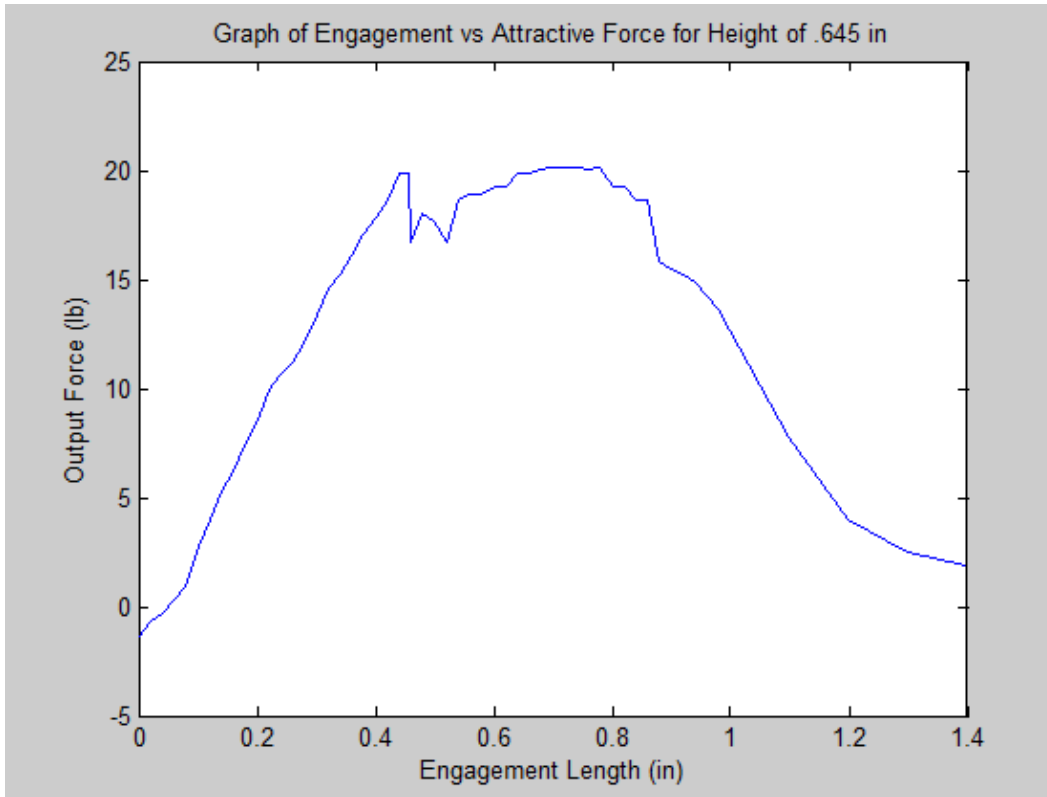


Figure 21: Output Force [lbs] vs. Engagement Length [in] where height difference is 0.645 in

As expected, the maximum force obtained was when there was no height difference between the magnet and the yoke. Note that the tops of the graphs appear to be jagged and not as high as the more continuous portions of the graphs would suggest. This region is where friction was experienced most by the magnet and the yoke.

Assuming the surface of the magnet was coated with zinc, the maximum amount of frictional force experienced in the system was no greater than 5 lb. This means that the maximum attraction between the yoke and the magnet did not exceed 43 lbs, and the engagement of maximum attractive force was between 0.7 and 0.8 inches, depending on the height of the magnet.

4 SPRING SEMESTER

4.1 REVISED METHOD OF ENGAGEMENT

The design for a hydrokinetic turbine that harvests tidal, mechanical energy and converts it into electrical energy to provide power for the Memorial Bridge went through many conceptual design stages. At the end of the fall semester the design plan involved a combination of three parts: a variable flux generator, a Gorlov turbine and a hydrofoil lifting mechanism. Though the design for the project still incorporates the use of variable flux generating technology in conjunction with a cross-flow Gorlov turbine in order to maximize power generation from current flow beneath the Memorial Bridge, a hydrofoil is no longer included in the design.

When the turbine is mounted underneath the Memorial Bridge, it will be important to know when to engage the generator. There are two ways in which the VFG can be engaged, passive actuation or active actuation. Passive actuation mechanisms use an input parameter such as time of day, flow speed, or RPM of the turbine to mechanically move the rotor axially relative to the stator. Active actuation mechanisms similarly use sensors to record an input parameter; however they adjust the rotor relative to the stator electronically and must expend energy in order to operate. The initial approach was to incorporate passive activation by attempting to control axial engagement using flow speed as the input parameter using a hydrofoil lifting mechanism (shown in Figure 22) to generate a lift force that would be transmitted to the rotor.

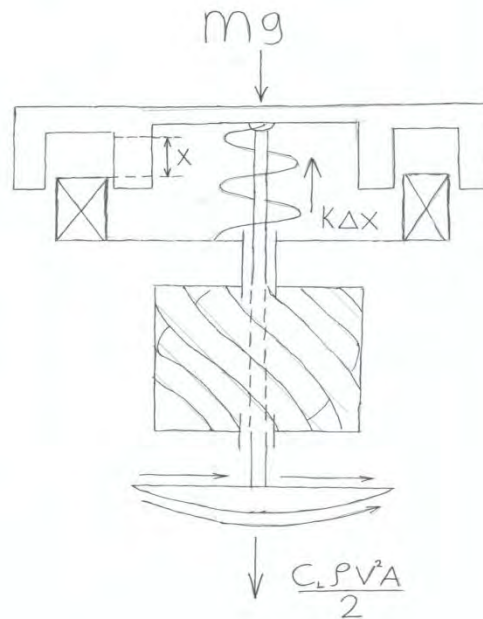


Figure 22: Schematic of the proposed activation mechanism.

This control system seemed appealing because it required no electronics to operate and would not draw power from the generator. The actuation mechanism would be controlled purely by the negative lift force of the river. In theory, the hydrofoil would be sized so that it would disengage the generator while river speeds were lower than the cut in speed of the turbine, but overcome the spring force when the river's flow exceeded the cut in speed:

$$K \Delta X_{engagement} = \frac{C_L \rho V_{cut\ in}^2 A}{2} \quad 10$$

In this equation, K is the spring constant with a unit of N/m, $\Delta X_{engagement}$ is the axial length of engagement in meters, C_L is the lift coefficient of the hydrofoil, ρ is the density of the fluid surrounding the hydrofoil, $V_{cut\ in}$ is the cut in speed of the turbine, A is the cross sectional area of the turbine perpendicular to the direction of the flow plane.

While the passive hydrofoil-based engagement mechanism seemed beneficial due to its ability to provide VFG activation independent of the turbine's generated power, it has proved to be an unrealistic element for design purposes. Due to the bidirectional current

flow, the hydrofoil would have to be symmetrical, which is such an uncommon shape that its design would detract from the objectives of the project.

The hydrofoil must also either be placed underneath, or to the side of the turbine in order for it to provide a lifting force. The reason for this is because the wake of the turbine would introduce turbulence to the hydrofoil which would cause it to behave differently depending on the direction of the water flow. If the foil is directly below the turbine's structure, the water flow underneath the turbine would cause the hydrofoil to may behave unexpectedly due to interfering vortices due to the boundary layer of the river bed and may not provide the necessary lift force. Also, the foil would require long members to transmit the negative lift to the generator that would create large moment arms with a high probability of buckling because they would be subjected to an intense bending stress induced by the water flow. If the foil is placed to the side of the turbine, the unexpected water flow issue would be remedied; however it would create a large moment on the support structure. The material cost of supporting the control mechanism would subsequently overshadow the profit made by incorporating VFG technology in the first place. It was also determined that with this orientation, it would be impossible to test the setup in the tow tank due to the size of the hydrofoil.

For these reasons, it was decided to use an active pump-based method of engagement to move the variable flux generator. By switching from a passive system to an active one, a tradeoff was made between consuming more power to operate the generator in order to simplify the design. Using an active engagement system would make use of existing sensors on the supporting structure of the turbine and would not require additional calculations involving fluid dynamics, mechanical advantage, gravitational forces, or additional underwater weight. The savings in start-up material costs may also outweigh the electrical losses induced by operating the pump.

4.2 BENCH TEST EXPERIMENT

4.2.1 OBJECTIVES

The purpose of the "table-top" experiment was to relate torque, RPM, output voltage, and linear engagement of the generator. This would theoretically correlate the torque resistance of the generator to the cut in speed of the turbine. This would then provide the information necessary to determine the proper disengagement length of the generator for when the water flow decreases below the cut in speed of the turbine. The bench test experiment would allow for the VFG to be characterized, which is essential before proceeding to testing the turbine with the generator.

4.2.2 THEORY

An electrical generator converts mechanical energy into electrical energy by spinning magnets relative to "yokes", or "cores" which are pieces of electrically conductive metal, usually iron or steel, the yokes are wound with copper wire as tightly and as many times as possible. As the magnets are moved near the yokes, a current is driven through the wire, and a voltage potential is generated. The voltage potential generated is best described using the integral form of Faraday's law and Ampere's law:

$$\text{Faraday's law: } \oint_C \vec{E} \cdot d\vec{l} = - \int_S \frac{\partial \vec{B}}{\partial t} \cdot d\vec{s} \quad 11$$

$$\text{Ampere's law: } \oint_C \vec{H} \cdot d\vec{l} = \int_S \vec{J} \cdot d\vec{s} \quad 12$$

Where the left side of the first equation represents the electrical field E integrated over any given closed loop C. The right side of the first equation represents the B field, or magnetic flux density integrated over the area of the closed loop C. The left side of the lower equation represents the magnetic field intensity H integrated over any given closed loop C. The right side of the lower equation represents the current travelling through the closed loop C. In intelligible terms, these equations can be combined, and written as:

$$\Delta V - IR \propto - \frac{d \mu_0 N I A_c}{dt L} \quad 13$$

Where ΔV is the voltage potential generated, R is the overall resistance of the wire (calculated as electrical resistivity*total length of wire/cross sectional area of wire), μ_0 is the permeability of free space, N is the number of wire turns, I is the current in the wire, A_c is some characteristic area of the yoke which the magnetic flux flows through, and L is the gap length between the magnet and the yoke. N, I, A_c , and L are all dependent on the geometry of the generator used, so they can vary depending on how the generator is built.

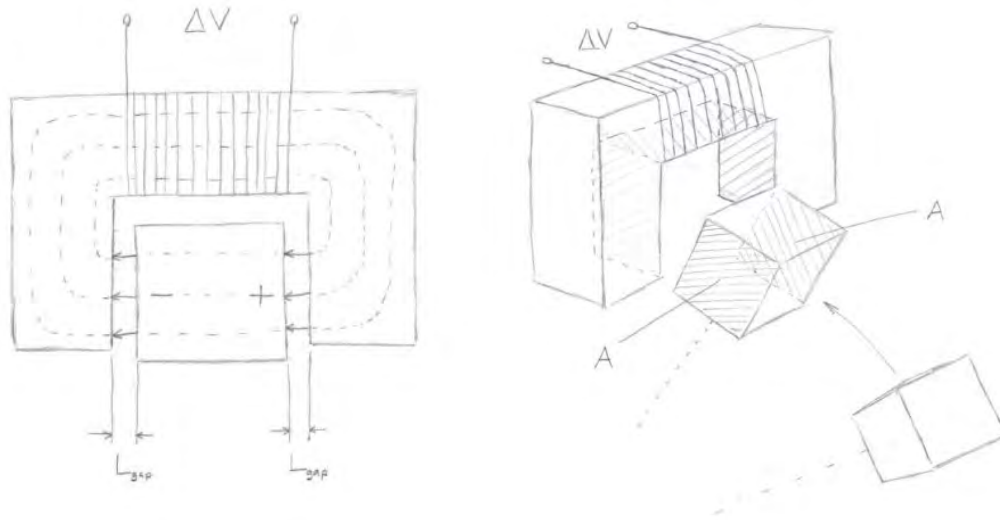


Figure 23: Generic Magnetic Model Describing the Path of Magnetic Flux.

What this equation really means, is that the power generated is proportional to how quickly the B field changes, which is a function of how fast the magnets rotate with respect to the yokes.

Using the Lorentz-Coulomb force equation, it can be shown that the electrical energy generated imparts a resistive torque on the generator, which can be written as:

$$\text{Lorentz - Coulomb force equation: } d\vec{F} = dq(\vec{E} + \vec{u} \times \vec{B}) \quad 14$$

Where F is force, q is charge, E is the electric field intensity, u is speed, and B is the magnetic flux density. In intelligible terms, this equation reduces to:

$$F = q\bar{u} \times \bar{B} \quad 15$$

What this equation really means is that there will be a force which resists the motion of the magnets. This force, distributed evenly on each magnet, creates a resistive torque, which can cause the turbine to stall. A greater B field will lead to a greater resistive torque, which will lead to a higher cut in speed of the turbine.

The lesson to take home from this segment of the report is that, the more power generated, the more resistive damping torque there is, and the more resistive torque there is, the higher the cut in speed of the turbine is, and the higher the cut in speed is, the lower the capacity factor is. The VFG is a mechanism which partially mitigates the correlation of power generation with capacity factor. VFGs axially displace the rotor of a generator from the stator in order to decrease the B field experienced by the yokes. This decreases the resistive torque transmitted to the turbine, and allows it to continue to generate electricity (albeit less efficiently) at lower flow speeds.

4.2.2a APPLYING MAXWELL'S FIELD EQUATIONS TO THIS GEOMETRY

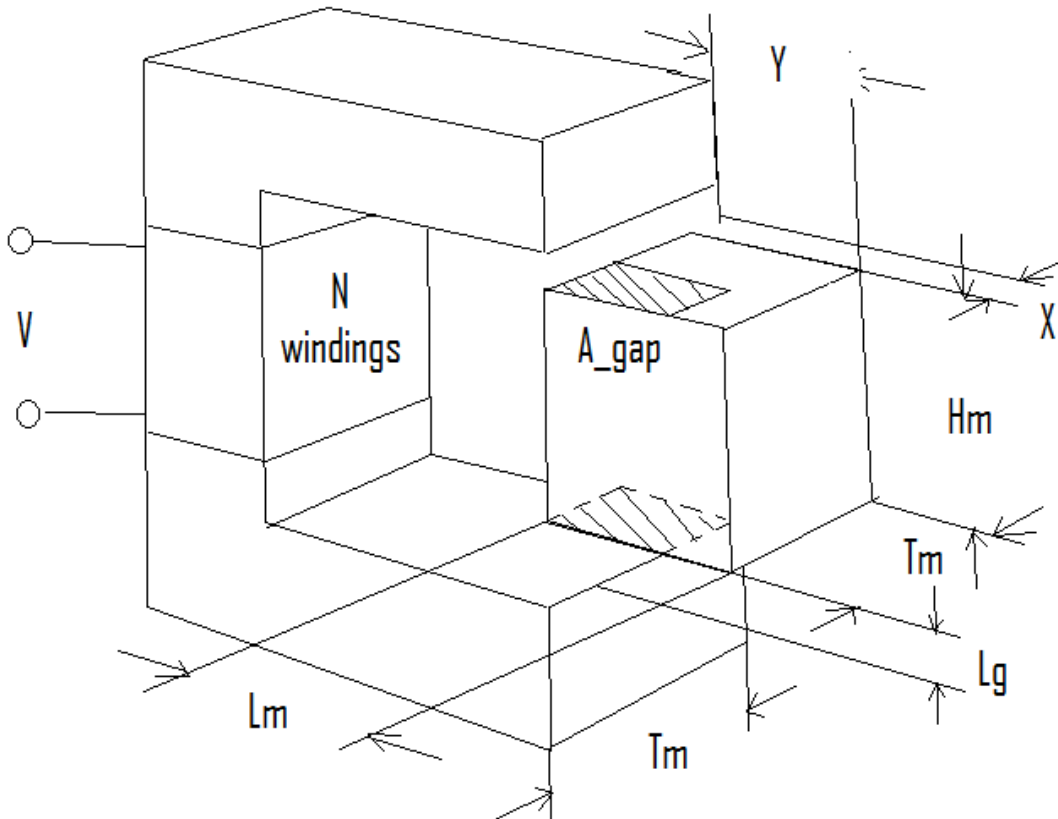


Figure 24: Schematic of Magnetic Model.

Ampere's law, assuming magneto quasi static:

$$\oint_C \vec{H} \cdot d\vec{l} = \int_S \vec{J} \cdot d\vec{s} \quad 16$$

By drawing a contour passing through the core, air gaps, and magnet, Ampere's law can be set up for the defined geometry from Figure 24:

$$\frac{B_{gap}}{\mu_0} L_g + \frac{B_{mag}}{\mu_m} H_m + \frac{B_{gap}}{\mu_0} L_g = NI \quad 17$$

Where the magnetic flux density of the magnet can be broken down to:

$$B_{mag} = \mu_m H + B_r \quad 18$$

Where H is the magnetic field passing through the magnet, and Br is the magnetic remanence. By applying Gauss' law, we can solve for the magnetic flux density (B) passing through the gap in terms of the magnetic flux density passing through the magnet

$$\text{Gauss' law, assuming } \mu_{core} = \infty: \quad \oint_C \vec{B} \cdot d\vec{s} = 0 \quad 19$$

$$B_{gap} A_{gap} = B_{mag} A_{mag} = B_{mag} L_m T_m \quad 20$$

The area of the gap can be interpreted in different ways. For these calculations, I specify an X and Y displacement of the magnet corresponding to radial and axial displacement of the VFG. I interpret the area of the gap to be:

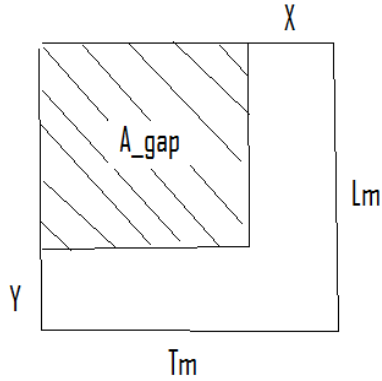


Figure 25: Description of the Cross Sectional Area of the Gap.

Where A_gap is:

$$A_{gap} = L_m T_m - L_m x - T_m y + xy \quad 21$$

This equation assumes that the core is at least as thick as the magnet is, and also assumes that the magnet is able to fit inside the core entirely without touching the windings. This area brings the magnetic flux density relation to:

$$B_{gap} (L_m T_m - L_m x - T_m y + xy) = B_{mag} L_m T_m \quad 22$$

Using the above relation, it is possible to solve for the magnetic flux density (B) passing through the gaps and the magnet.

$$B_{gap} = \frac{NI - \frac{B_r H_m}{\mu_m}}{\frac{2L_g}{\mu_0} + \frac{H_m(L_m T_m - L_m x - T_m y + xy)}{\mu_m L_m T_m}} \quad 23$$

$$B_{mag} = \frac{NI - \frac{B_r H_m}{\mu_m}}{\frac{H_m}{\mu_m} + \frac{2L_g L_m T_m}{\mu_0(L_m T_m - L_m x - T_m y + xy)}} \quad 24$$

With the magnetic flux density of the gaps and the magnet solved for, the forces acting on the magnet can be calculated using the method of co-energy.

$$\text{Co energy: } W'_m = \frac{1}{2} \int \mu H \cdot H dV = \frac{B^2 V}{2\mu} \quad 25$$

$$\text{2D definition of energy: } \frac{\partial W'_m}{\partial y} + \frac{\partial W'_m}{\partial x} = F \hat{x} + F \hat{y} \quad 26$$

$$W'_{m,magnet} = \frac{\left(NI - \frac{B_r H_m}{\mu_m}\right)^2 L_m T_m H_m}{2\mu_m \left(\frac{H_m}{\mu_m} + \frac{2L_g L_m T_m}{\mu_0(L_m T_m - L_m x - T_m y + xy)}\right)^2} \quad 27$$

$$W'_{m,gap} = \frac{\left(NI - \frac{B_r H_m}{\mu_m}\right)^2 L_g (L_m T_m - L_m x - T_m y + xy)}{2\mu_0 \left(\frac{2L_g}{\mu_0} + \frac{H_m(L_m T_m - L_m x - T_m y + xy)}{\mu_m L_m T_m}\right)^2} \quad 28$$

$$W'_{m,tot} = 2W'_{m,gap} + W'_{m,magnet} \quad 29$$

$$W'_{m,tot} = \frac{\left(NI - \frac{B_r H_m}{\mu_m}\right)^2 L_g (L_m T_m - L_m x - T_m y + xy)}{2\mu_0 \left(\frac{2L_g}{\mu_0} + \frac{H_m(L_m T_m - L_m x - T_m y + xy)}{\mu_m L_m T_m}\right)^2} + \frac{\left(NI - \frac{B_r H_m}{\mu_m}\right)^2 L_m T_m H_m}{2\mu_m \left(\frac{H_m}{\mu_m} + \frac{2L_g L_m T_m}{\mu_0(L_m T_m - L_m x - T_m y + xy)}\right)^2} \quad 30$$

To find the magnetic attractive force, it is necessary to take the derivative of the total co-energy with respect to distance. The most relevant parameter for us is the force in the Y direction, because this is the axial engagement force.

$$\begin{aligned}
\text{Engagement Force} &= \frac{\partial W'_{m,tot}}{\partial y} & 31 \\
&= -\frac{(NI - \frac{B_r H_m}{\mu_m})^2}{\mu_0} \left(\frac{L_g \left(L_m T_m \frac{\mu_m}{H_m} \right)^2 (T_m - x) \left(-T_m L_m + L_m x + T_m y + \frac{2L_g L_m T_m \mu_m}{\mu_0 H_m} - xy \right)}{\left(T_m L_m - L_m x - T_m y + \frac{2L_g L_m T_m \mu_m}{\mu_0 H_m} + xy \right)^3} \right. \\
&\quad \left. + \frac{2L_m^2 T_m^2 H_m L_g (T_m - x) (-T_m L_m + L_m x + y(T_m - x))}{\mu_m \left(\frac{2L_g L_m T_m}{\mu_0} + \frac{H_m}{\mu_m} (L_m T_m - L_m x - T_m y + xy) \right)^3} \right)
\end{aligned}$$

As you can see, the analytical solution to the engagement force becomes quite hairy when multiple displacement variables are involved. Furthermore, this solution does not account for flux leakage, otherwise known as “fringing”. What this means, is that as X and Y increase, the accuracy of this model decreases. According to this model, if either X or Y exceed T_m or H_m respectively, the magnetic attraction should drop to zero. Experimental evidence has shown otherwise; near the higher levels of disengagement, when the magnet is no longer inside the core, magnetic attraction still exists and the generator can even generate electricity, which means that a non-zero amount of flux passes through the magnets.

Because of the inaccuracy of the analytical solution in higher levels of disengagement, the dependency of the solution on current (which also varies with the time derivative of x), and the difficulty of acquiring such a solution, it is highly recommended that finite element analysis or the method of magnetic lumped models (including fringing effects) is used instead of finding the analytical solution to your geometry.

4.2.2b CALCULATING THE VOLTAGE

$$\text{Faraday's law: } \oint_C \vec{E} \cdot d\vec{l} = -\frac{d}{dt} \int_S \vec{B} \cdot d\vec{s} = -\frac{d}{dt} N\Phi = -\frac{d}{dt} \lambda \quad 32$$

Faraday's law is used to describe a relation between voltage potential and the time derivative of magnetic flux. The flux, or flux linkage, component can be expressed in different ways; fortunately the magnetic flux has already been calculated above. The voltage component can be seen as the total potential of the system:

$$-V + IR_{wires} = -\frac{d}{dt} NB_{mag}A_{mag} \quad 33$$

$$= -\frac{d}{dt} N \left(\frac{NI - \frac{B_r H_m}{\mu_m}}{\frac{H_m}{\mu_m} + \frac{2L_g L_m T_m}{\mu_0(L_m T_m - L_m x - T_m y + xy)}} \right) (L_m T_m)$$

Where V is the voltage generated, and R_{wires} is the total resistance of all the wires in the system. Simplifying:

$$-V + IR_{wires} = -\frac{d}{dt} \left(\frac{N \left(NI - \frac{B_r H_m}{\mu_m} \right)}{\frac{H_m}{\mu_m L_m T_m} + \frac{2L_g}{\mu_0(L_m T_m - L_m x - T_m y + xy)}} \right) \quad 34$$

Because x (radial displacement) and current can vary with respect to time (assuming y, the axial engagement, is unrelated to time) the chain rule is necessary:

$$V - IR_{wires} = \left(\frac{N \left(NI - \frac{B_r H_m}{\mu_m} \right)}{\frac{H_m}{\mu_m L_m T_m} + \frac{2L_g}{\mu_0(L_m T_m - L_m x - T_m y + xy)}} \right) \left(\frac{\partial}{\partial x} \frac{\partial x}{\partial t} + \frac{\partial}{\partial I} \frac{\partial I}{\partial t} \right) \quad 35$$

Solving this equation yields a result with a back EMF portion and an inductance portion:

$$V - IR_{wires} = \left(\frac{N \left(NI - \frac{B_r H_m}{\mu_m} \right) \left(\frac{2L_g}{\mu_0} \right) (L_m - y)}{\left(\frac{H_m}{\mu_m L_m T_m} (L_m T_m - L_m x - T_m y + xy) + \left(\frac{2L_g}{\mu_0} \right)^2 \right)^2} \right) \dot{x} \quad 36$$

$$+ \left(\frac{N^2}{\frac{H_m}{\mu_m L_m T_m} + \frac{2L_g}{\mu_0(L_m T_m - L_m x - T_m y + xy)}} \right) \dot{I}$$

$$V - IR_{wires} = K_b \dot{x} + L \dot{I} \quad 37$$

In simpler terms, a voltage will be produced from the damping of the back EMF term (K_b), and the inductance of the wires in the system (L). It is necessary to know the velocity of the magnets with respect to the cores (\dot{x}) and the time derivative of the current (\dot{I}) in order to solve this equation.

If the current is held steady and the resistance is found to be negligible, the voltage can be solved for in terms of speed of the magnets only. While these assumptions may cause a noticeable error, it will greatly simplify the expected power output calculations of the generator by creating a direct proportionality between the back EMF damping and the voltage.

4.2.3 EXPERIMENTAL METHODS

The test involved rotating six Neodymium 42 one inch cubic magnets with respect to six iron yokes at various, at measurable steady state RPMs and a given engagement length that was controlled with a hydraulic actuator. To ensure that the magnets spun properly along the stator, a variable length shaft was designed to transmit the torque while allowing the magnets to engage with the stator. The magnets were connected to the rotating disk using specially designed magnet holders that would not alter the form of the existing disk.

Before implementing the existing hydraulic actuator to the turbine/VFG system, the connection between the drive shaft and the hydraulic arm needed to be designed. The drive shaft, which would be connected to the shaft of the turbine with a right angle drive, had to remain linearly constrained.

The horizontal drive shaft was held in place by a base-mounted steel ball bearing to provide the shaft with the freedom to have rotational motion. This was important, because this would take the turbine's output shaft power and connect its rotational motion to the generator. However, the horizontal drive shaft needed to be prevented from having linear motion so that it would be permanently connected to the turbine's shaft to maintain rotational engagement 100% of the time, regardless of the level of linear engagement. This linearly static shaft required an adapter, which can be seen in Figure 26, that could transfer the drive shaft's rotational motion to the generator while allowing the generator to move linearly for engagement purposes.

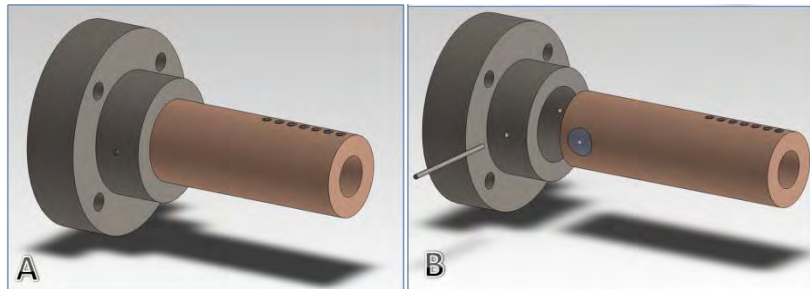


Figure 26: A) Assembled view of adapter. B) Exploded view of adapter.

It was decided that an oil-impregnated bronze sleeve, as seen in Figure 27, be used to slide over the horizontal drive shaft. It was imperative that the bronze sleeve have an interior diameter that was bored out to slide-fit the one-inch drive shaft well.

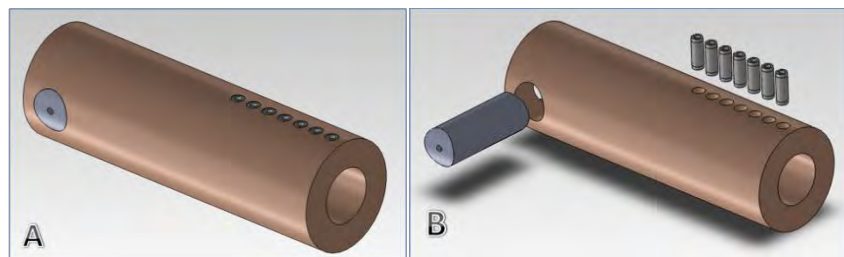


Figure 27: A) Assembled view of bronze sleeve. B) Exploded view of bronze sleeve.

This required that the interior diameter be bored out between 0.0005 and 0.001 inches larger than the drive shaft so that the drive shaft could easily slide in and out of the sleeve; however, any larger difference between the diameters would cause too much slop for the desired smooth linear motion. The bronze sleeve must have been oil-impregnated, because this bronze material provided self-lubrication while the C1045 steel drive shaft slid within the sleeve.

The rotational and linear motions were combined with the use of a keyed drive shaft and collinear, hardened steel pins that were press-fitted into the bronze sleeve. These pins slide-fit the keyway of the drive shaft, which allowed the rotation of the drive shaft to engage the sleeve while the sleeve slid linearly back and forth over the shaft. The sleeve acted as a rotational/translation adapter. Figure 28 provides a visual example of the pins fitting into the keyway. It still needed a means for connecting that rotational motion with the rotor.

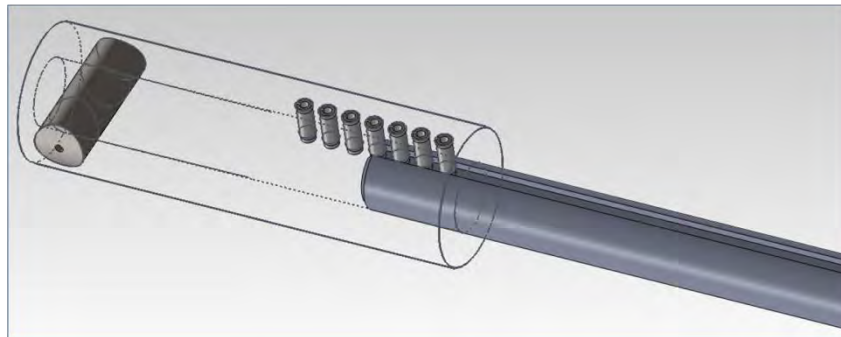


Figure 28: Linear engagement was provided by the combination of the pins and the keyway.

The existing rotor had four holes where bolts were designed to run through and lock the rotor between two 4-bolt flange bearings. This was accomplished by taking a high-strength 1045 steel rod, and lathing/milling it to specifications as seen in APPENDIX 4. Four larger bolts were used to attach the adapter mount to the rotor over the outer ball bearing. For proper engagement between the adapter sleeve and the adapter mount, the sleeve must slide-fit into the mount. The primary reason for making this a slide-fit rather than a press-fit was due to the need for a fail-safe. In a worst-case scenario, if the magnets were to cog up at a dangerously high RPM or even collide with the stator, the implementation of a shear pin would be desired. It is an inexpensive and simple solution used to avoid an expensive disaster. Refer back to Figure 26 to help understand the assembly. A great example of a device that relies on shear pins are snow blowers as a means for protecting the motor if a foreign object of destruction (FOD) gets jammed in the auger. In the case in which the shear pin had to break, the sleeve needed to be able to freely spin within the adapter mount. Once again, this slide-fit must not have been too loose, at which there is any slop when in place. Slop can create extra undesired forces on the shear pin. It was also important that the interior face of the sleeve be pushed back into the securing lip of the mount. This helped prevent extra linear forces on the shear pin. Basically, the only noticeable forces acting on the shear pin would be the rotational forces being transferred from the sleeve to the adapter mount.

The single shear pin, as seen in Figure 26, fits through the entire diameter of the adapter mount, which connected the sleeve to the mount with two connections. These two connecting locations doubled the single shear pin's connecting strength, and it provided symmetrical force applications to the adapter. The size and material of the shear pin was based on a failure torque of approximately 1460 lb-in and the list of available materials. Originally, carbon steels, such as C1018, were going to be used. A C1018 steel rod with a diameter of 0.125 inches and two contact locations would have a safety factor of 1.34. However, at the time this section of the adapter was being dealt with, the best available material with a diameter of 0.125 inches was O2 tool steel. O2 tool steel ended up having a safety factor of approximately 8.5. For initial prototype testing, this was not an issue, because testing speeds and engagement variations were to start in the conservative range due to a lack of experience with this system's dynamics in motion. However, it is recommended that the current shear pin be replaced with a carbon steel material, such as C1018, before extensively testing this prototype.

The shear pin was designed to act as a safety mechanism. If a magnet and an iron core were to collide, it was imperative that the shear pin break at that point. This would prevent further damage to parts such as the adapter system and drive shafts by allowing the rotational motion to continue without rotationally engaging the rotor. While performing bench testing, the shear pin also acts as a safety measure for the motor in case the cogging of the magnets overpower the motor's ability to drive the rotor as the rotor further engages the stator. When implementing the shear pin, there was one other factor that had to be considered which was tearout. Even though the shear pin had high yield strength, the material that the shear pin runs through can be deformed before the shear pin begins to yield. This was not a problem for the C1045 steel adapter mount, but this was an issue for the more malleable bronze sleeve. The tearout calculations can be viewed in APPENDIX 3. This problem was solved by press-fitting a 0.75 inch C1018 steel dowel through the entire diameter of the bronze sleeve at the location of the shear pin. The C1018 steel dowel can also be seen in Figure 27. The steel dowel has no noticeable issues with tearout as the shear pin runs through the center of it. The overall stress acting on the malleable bronze was decreased by providing more contact surface area at the location where the shear force is applied.

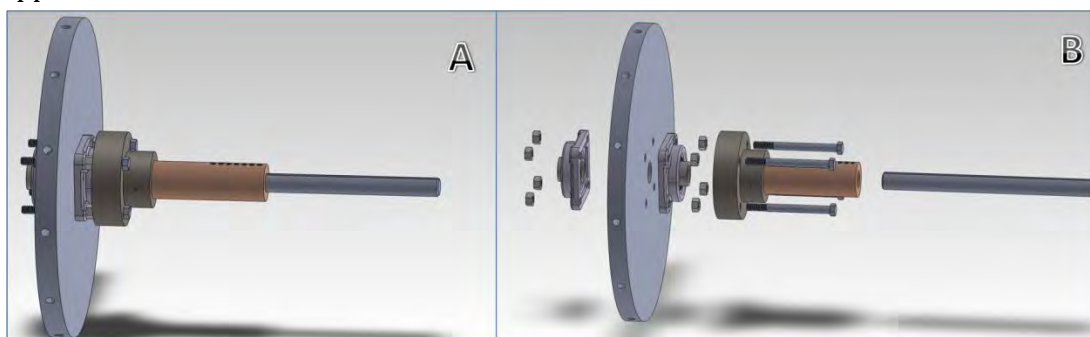


Figure 29: A) Assembled view of adapter with rotor, drive shaft, ball bearings, and required hardware. B) Exploded view of Figure 29.A

Another challenge that existed from the previous VFG group was the device for holding the magnets. The previous group used a large PVC pipe with slots used to hold the magnets after adding epoxy. There were two primary issues that had to be addressed. First of all, the magnets were locked in place once the epoxy was applied; so, each magnet was not capable of being individually adjusted. The other existing problem was that the PVC ring would bend under the stress. These issues are what led to the previous group experiencing a collision of at least one of their magnets with an iron core. It was necessary to design a device that would rigidly hold the magnets in place while allowing each magnet the freedom to be individually adjustable. As seen in Figure 30, each magnet is held in place by an individual magnet mount/placer. For a detailed view of the magnet placer/mount assembly, refer to APPENDIX 3. Each magnet is capable of being adjusted until the entire ring of magnets concentric and then firmly held in place by the use of four steel socket head cap screws.

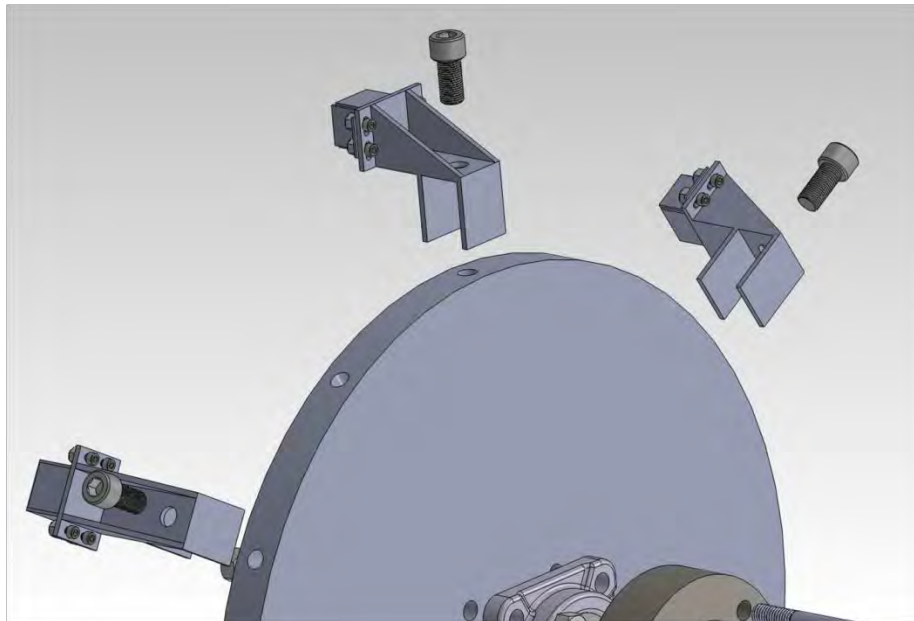


Figure 30: Exploded view of magnets in magnet mounts about the rotor.

With VFG prototype completed, the testing devices could then be added onto the design. A servo motor, with controllable output RPM capability, was coupled to an inline rotary torque transducer that was coupled to the variable length shaft of the VFG. A hydraulic hand pump equipped with two pressure gauges was used to control engagement. The pump's cross sectional area of 3.75 inches (refer to the equipment list in the appendix for a complete list of specifications) and the pressure reading from the pressure gauge was used to determine the pull force at various levels of engagement. The output voltage from 6" LVDT was used to determine the engagement length when calibrated with digital calipers. Pictures of the various experimental setups are displayed in the following images.



Figure 31: Experimental setup for measuring force at different engagements.

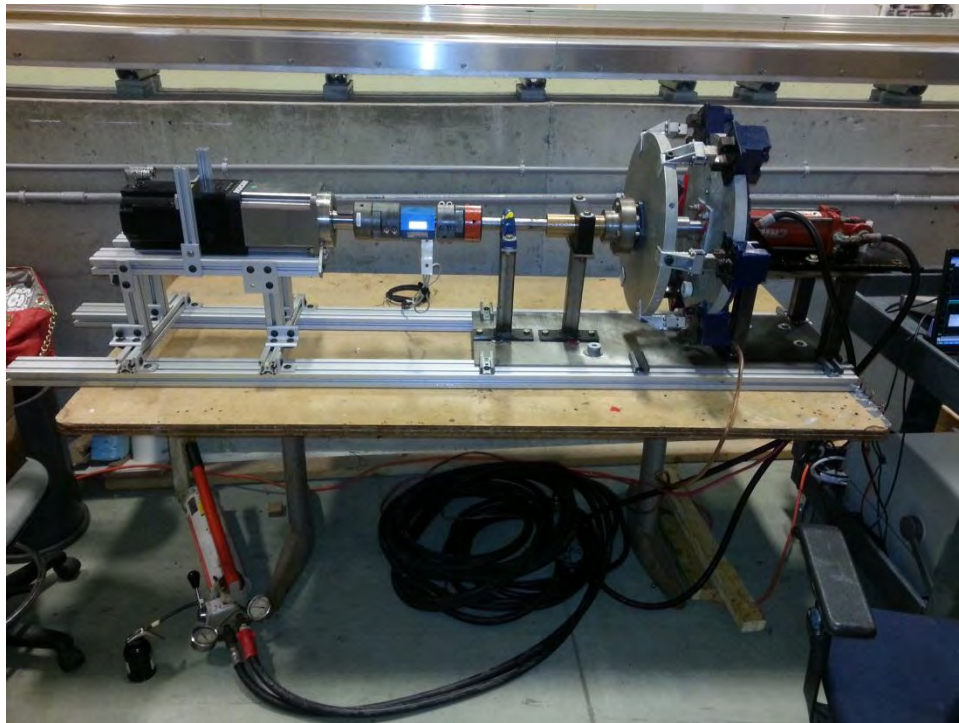


Figure 32: Experimental setup of bench test procedure.

The experimental setup shown in Figure 32 shows the VFG (on the right) clamped onto 8020 aluminum that was also connected to the stand used to hold the servo motor.



Figure 33: Data acquisition board that allowed for data to be recorded.

4.2.4 RESULTS AND DISCUSSION

The first thing accomplished was calibrating the LVDT for various known displacements. The graph of this (shown below) provided a linear equation enabling for displacement to be calculated based upon the LVDT's output voltage.

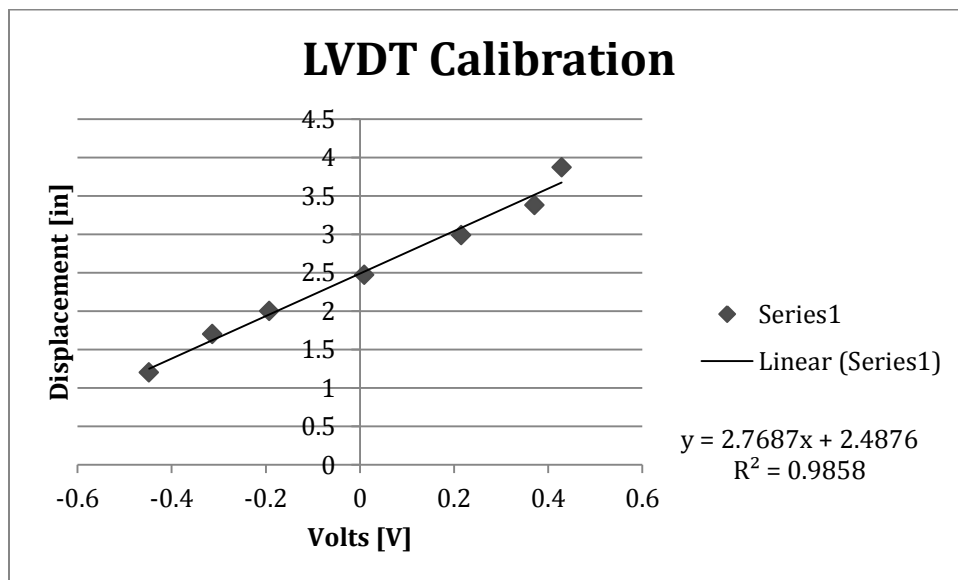


Figure 34: LVDT Calibration

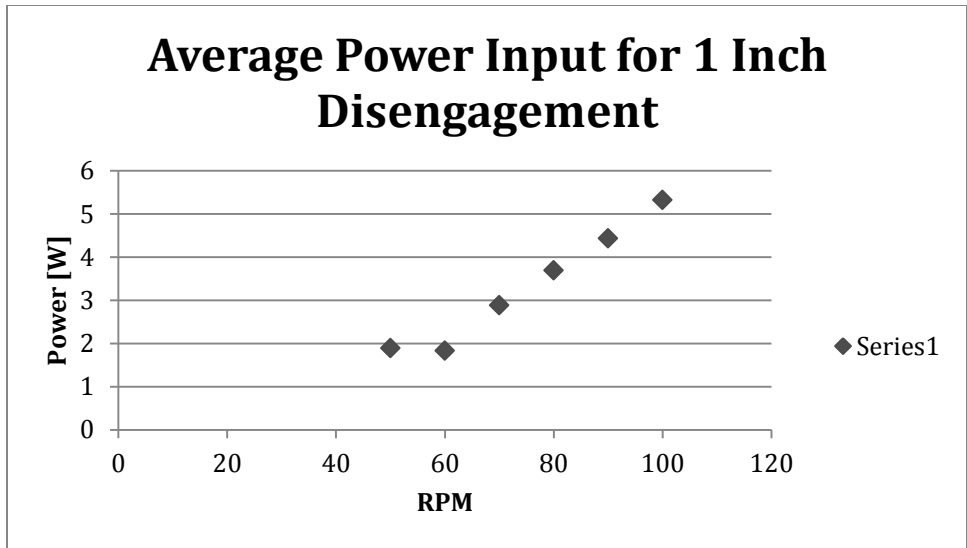


Figure 35: Average input power for engagement of 1 inch.

In Figure 35, the input power for 1 inch disengagement behaves as expected by increasing with increasing RPM speed. Though average generated power (shown in Figure 36) increases as well, but not as linearly.

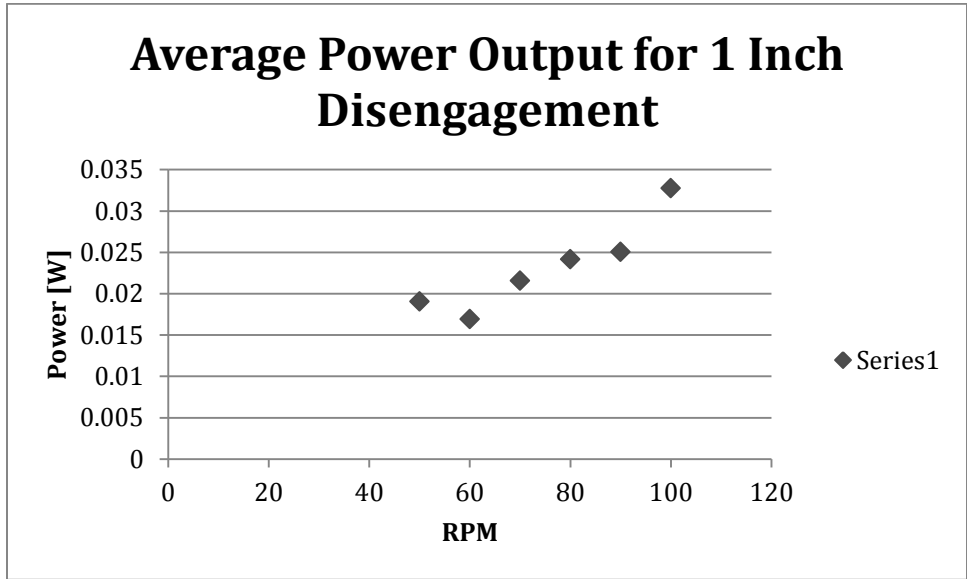


Figure 36: Average power generated by the VFG at 1 inch disengagement.

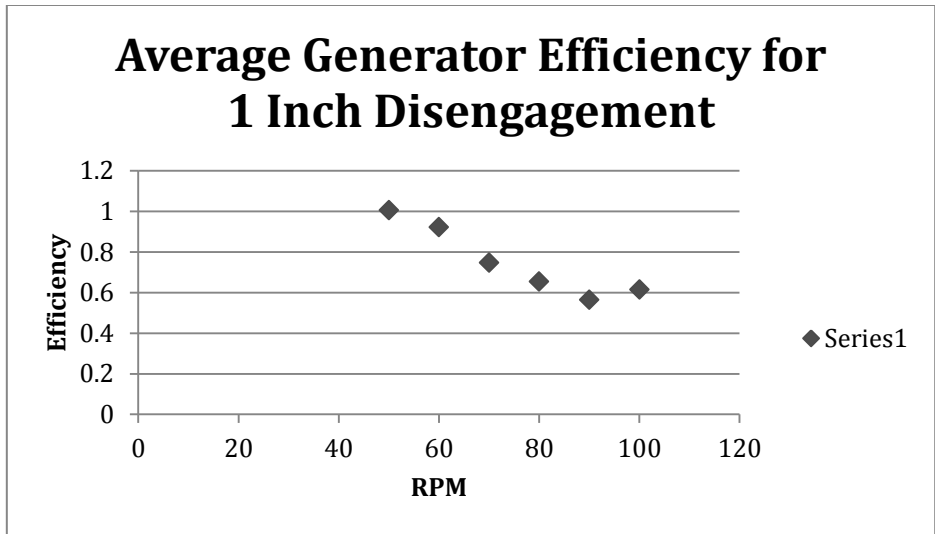


Figure 37: Average VFG efficiency for 1 inch disengagement.

The Generator was not able to be tested for as wide of a range as was hoped for. Due to the inability of acquiring data for engagement distances other than 1 inch, it is impossible to find the maximum efficiency of the generator. While this does limit the conclusions which can be drawn from these results, it is possible to observe trends.

Note that the generator efficiency decreases as the rotational speed increases. There is not enough data over a large enough range of data points to fit a line or curve to the plot. The only thing that can be gleaned from this graph is that as RPM goes up, efficiency goes down. Also note that the efficiency is nearly always less than 1% for this test. The reason for this is because the only magnetic flux passing through the magnet was the fringing. At this level of engagement, the generator is not meant to be efficient, it is meant to decrease the back EMF and reduce the cogging forces.

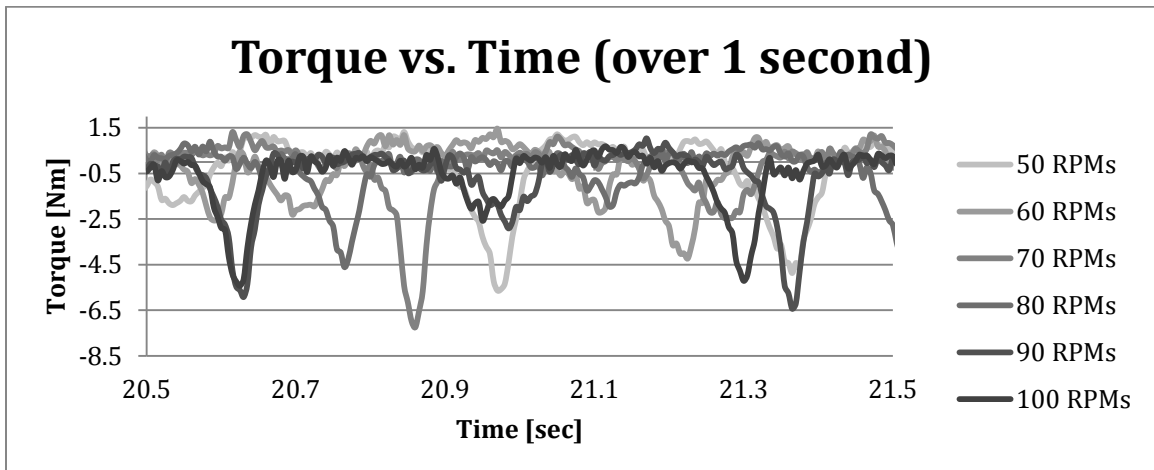


Figure 38: Torque (Nm) measured at each of the 5 RPM speeds over 1 second time interval.

From this graph it is possible to see that the static, or cogging torque, hovers around 5 Nm at its peak regardless of the RPM. This number is relatively small, and makes sense, because the magnets were disengaged. From the graph of efficiency and the graph of torque, it is

possible to conclude that if the magnets are disengaged, the efficiency will be lowered, but the cogging torque will be noticeably lower than if the magnets were fully engaged. Furthermore, the lack of relation between maximum torque and RPM can be attributed to the fact that the generator was operating at a low efficiency. From an energy standpoint, what goes in as mechanical power, must come out as electrical power; so if the electrical power generated is very low, it makes sense that the back EMF will also be very low, and the dampening effect will have a negligible impact on the maximum torque.

Additional data points are required if this generator is to be fully characterized. The initial observations are intuitive; however they are less meaningful without taking data for multiple levels of engagement.

4.3 SUPPORT STRUCTURE ANALYSIS

4.3.1 FINDING THE FORCES AND LOADS

One of the more important factors in designing a support structure for the Memorial Bridge turbine is knowing the loads and forces that act on it. The report from last year’s Memorial Bridge Turbine group provided a few key pieces of information allowing for the calculation of forces acting on a structure in the waters of the Piscataqua River under the Memorial Bridge. The most important was the velocity magnitude profile, which gave a visual representation of the speeds that the water flows at that cross section of the river. An aspect that makes the Memorial Bridge an ideal location to implement a tidal turbine is that this estuary has one of the fastest rated tidal currents in North America. Most other sites, such as the UNH Tidal Energy Test site, do not have the potential energy for this opportunity.

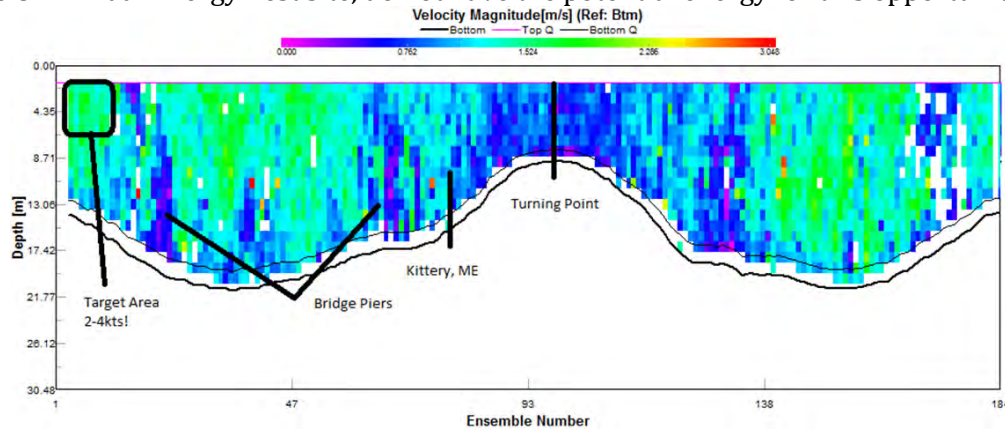


Figure 39: Water velocity profile beneath the Memorial Bridge.

The first force to be considered is that which is imparted by the water. When looking at the velocity profile, the maximum velocity is about 2 or 3 m/s. Due to the fact that the velocity profile can be difficult to read an exact number and is spread over a range, a water velocity of 4m/s (13.124 ft/s) was used to ensure a factor of safety. In order to turn the water velocity into a force, it was converted to a pressure first. To find pressure, section 3 (loads and load factors) of the AASHTO manual was used as a reference. Pressure is given by equation 3.7.3.1-1 from section 3.7 (water loads) and is listed in the following equation.

$$P = C_D \frac{w}{2g} V^2 \quad 38$$

In this equation P is the pressure, w is the specific weight of water, g is the gravitational acceleration constant, C_D is the drag coefficient, and V is the velocity of water. According to this equation, a pressure of 233.6 psf was found. To find the force that acts on the support structure, this pressure needed to be converted into a force (F) using the general equation:

$$F = P \times A \quad 39$$

The symbol A in the equation is area. So the 233.6 psf was then multiplied by the area the water pressure acts upon. Since the frame is almost entirely hollow, the area that was used to calculate force was the area of the turbine, and this was modeled as a solid cylinder to account for the highest possible force giving an additional factor of safety. The turbine is 3 × 3 meters (9.84 × 9.84 ft) which gives an area of 96.8 square feet. Therefore, using Eq. 39, the force due to water pressure in the direction of the flow was found to be 22,618.5 pounds (22.6 kips).

The second major force considered was the drag force on the frame. As a fluid flows past an object it creates turbulence which causes drag. This drag can play a significant role in providing additional forces on the frame. To find the drag force, the textbook for the fluid mechanics course (Engineering Fluid Mechanics 9th edition; Crowe, Elger, Williams and Roberson) was used as a reference. The drag force equation is given by:

$$F_D = C_D \times A \left(\frac{\rho V^2}{2} \right) \quad 40$$

In this equation the drag coefficient, C_D , was found using the referenced book's Table 11.1 – Approximate CD values for various bodies. The density of water, ρ , is 62.4 pcf and the velocity of water, V , is 13.124 ft/s. With these values the resulting drag force was 572,210 lbm×ft/s² (or 575 kip×ft/s²).

In order to add this drag force to the frame, it needed to be converted from foot pounds per second squared to pounds of force. The conversion factor is 1 lb force = 32.17 lbm×ft/s². Dividing the initial calculated force by the conversion factor yielded a drag force with the same units (lbs of force) as the pressure force:

$$F_D = (572209.5 \text{ ft} \times \text{lb} / \text{s}^2) / (32.17 \text{ lbm} \times \text{ft} / \text{s}^2) = 17787 \text{ lbf} = 17.8 \text{ kips}$$

Adding the pressure force and drag force together gives the total force in the direction of flow:

$$\sum F_x = \text{pressure} + \text{drag} = 22.6 \text{ kips} + 17.8 \text{ kips} = 40.4 \text{ kips}$$

The final force that had to be considered was the gravity force, or self-weight of the structure. Since the turbine and frame design had not yet been finalized at the point of load calculation, it was assumed that the weight of the turbine and generator would produce a load of 1 kip at each connection to the frame. This provided an overly conservative estimate of the turbine and frame weight for analytical purposes.

A load that would normally be considered in a project such as this would be impact loading. In this project, the structure is outside the shipping lanes so it was assumed that no water

traffic would come close enough to present an issue. In addition, the portion of the structure that will be outside of the water will be painted either white or yellow in accordance with Coast Guard code to make it easily noticeable to any recreational boats passing by.

4.3.2 GEOMETRIC CONSTRAINTS

A large factor in the frame design was the space constraints of the site. This site is a major shipping lane, so the frame must be outside of the main channel in order to avoid conflicts with vessels. Fortunately one aspect that makes this site feasible is that there is sufficient flow on the outer side of the pier, as shown by Figure 40: Power density vs. depth.

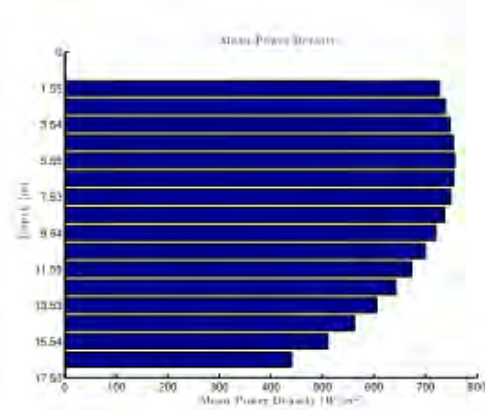


Figure 40: Power density vs. depth.

The flow in the river is not consistent throughout its depth, meaning there is a zone of optimal flow that would produce the most power from the turbine. This meant that the frame must be deep enough to put the turbine in this “sweet spot” of high flow. As shown in the previous figure the zone of highest flow is about 3 meters to 10 meters deep. This is the region in which the turbine will be centered around.

The support will be attached to the side of the pier, meaning it will be underneath the bridge. This causes more constraints with regards to how large the structure is and where it can be placed. From the point where the frame connects to the transfer plate to the bottom of the bridge there is a 14 foot clearance as seen in Figure 41. The frame had to be shorter than this height restriction in order for it to be raised up for maintenance purposes.

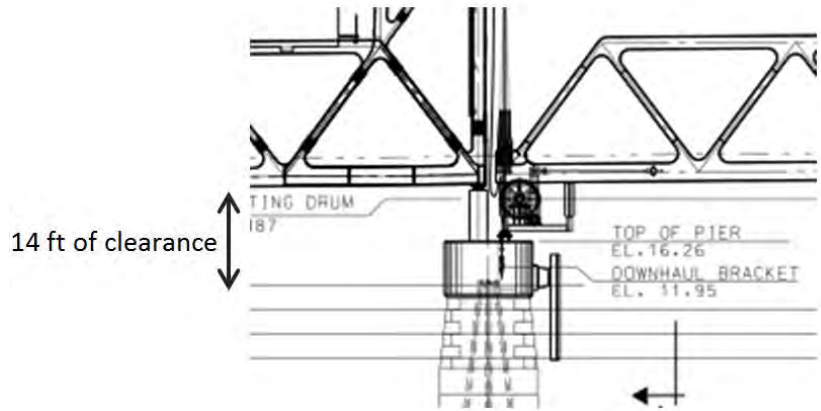


Figure 41: Height clearance of the pier cap to the bridge.

The pier is wider at the base than the top, which in turn creates another constraint. To ensure adequate space between the pin connection on the riverbed and the base of the pier, the beams that the support structure attaches to must span out away from the pier cap (shown below).

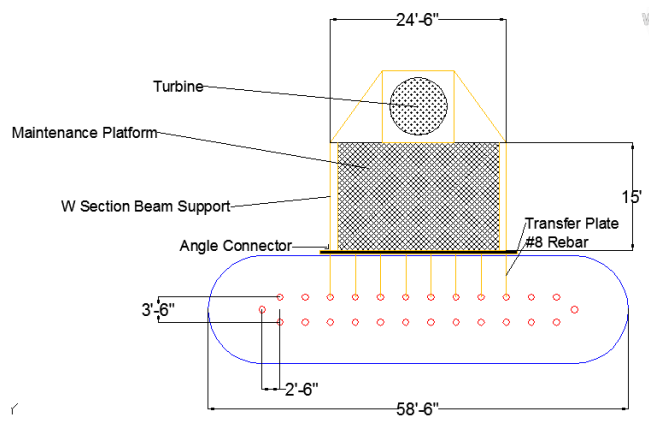


Figure 42: Plan view of the structure.

There were also other factors that had to be considered when looking at the amount of space available. The frame had to be both large enough and with enough free space to include various sensors and monitoring equipment. There will be several sensors including video monitoring and weather/tidal sensors attached to the frame. Due to the adaptability of the frame and its open design, there is plenty of opportunity to attach sensors.

4.3.3 DESIGNING THE FRAME

The frame was designed to be as open as possible to allow optimal flow to the turbine. As previously stated, a comparison was made between using steel or aluminum for the material so that there will be less bracing and more strength for the frame design. If there were more bracing supports, the structure would interfere with the flow going into the turbine.

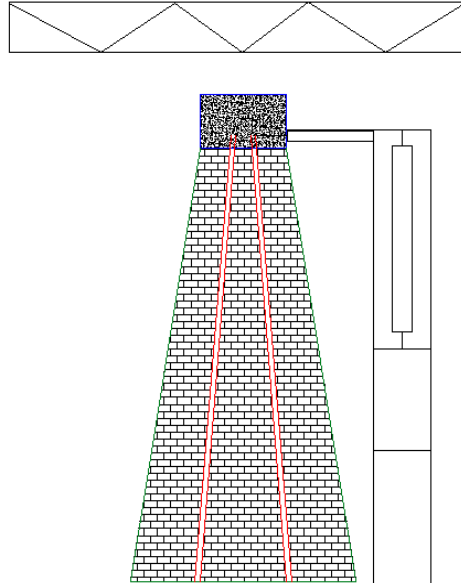


Figure 43: Elevation view.

4.3.3a MAINTENANCE PLATFORM

As previously stated, there will be a transfer plate attached to the rebar connected from the micro piles. From this transfer plate, two W section beams will be attached as pin supports fifteen feet in length. This is required because of the widening of the base of the pier. There will be a pin connection to the transfer plate so that in case of an emergency, the structure can be removed from the water in a fast procedure.

There will also be a steel platform that will be attached to the top of these two W section beams. This will be the maintenance platform where the generator will be located and kept on as well as providing an area for maintaining the turbine if it needs repairs.

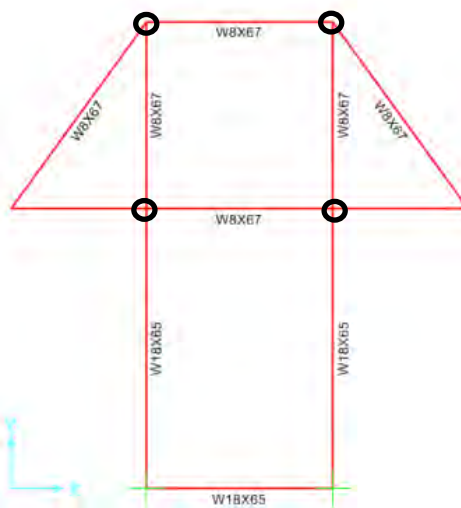


Figure 44: Plan view of the trapezoidal frame.

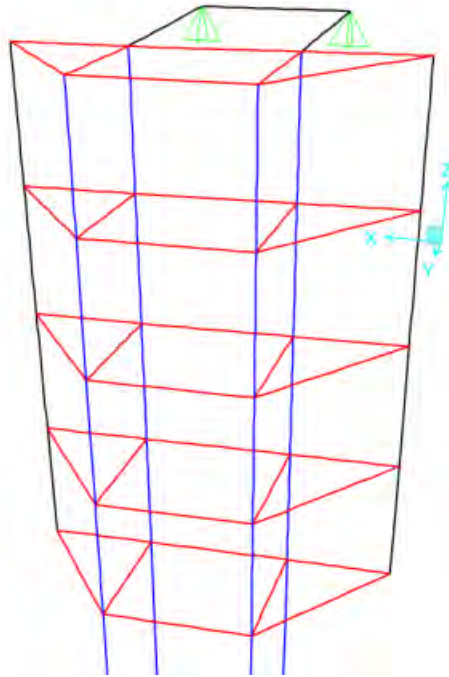


Figure 45: 3D model of the turbine structure.

4.3.3b TRAPEZOIDAL FRAME

From the platform, there will be a trapezoidal frame that will incase the turbine. The trapezoidal structure shown in Figure 44 is four sections spaced at eight foot intervals. We have decided to use I-shaped steel beams for our design. The inner square of the trapezoidal frame is very important. This is where the turbine will be incased during operation. This is shown in Figure 45 as the blue lines as well as in Figure 44 as the black circles. There will be a rubber track over the I-beams in blue that will control the turbine placement. This will be used for maintenance purposes to lift the turbine above the water.

The turbine frame will be supported in two locations. One is the transfer plate described above, and the bottom of the structure will be supported at bedrock. From the end of the trapezoidal structure, the beams in the longitude direction will be extended 43 feet to the bottom of the rock bed. This will be a pin connection so that the structure does not disrupt any wildlife or organisms on the rock bed. The amount of pin connections can vary depending on how many connections the NHDOT and Archer/Western wants to include in the final design of the structure. The structure will have the greatest strength with six or four pins but they can also design for two pins if that was a factor in their design criteria. In this frame, it has been designed with four connection pins. These four pins were located on the inner frame because this is the most critical area of loading due to the turbines weight.

To test the design of the frame, we used SAP2000, a structural analysis program. We designed for the forces stated above; distributed water load, dead load of the structure, turbine weight, and the generator weight. These load cases are shown below with the designated location of the load.

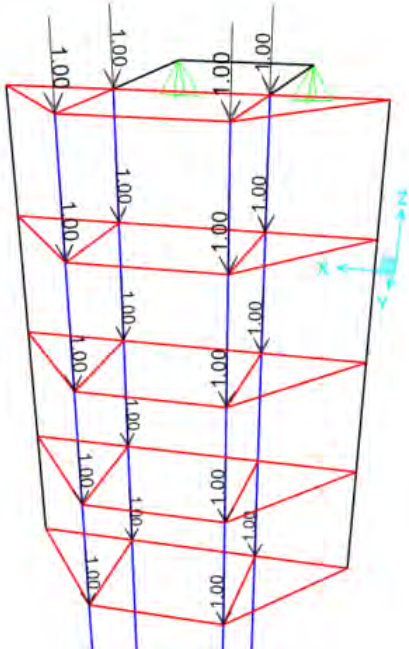


Figure 46: Turbine load.

As shown in Figure 46, the assumed weight of the turbine was one kip, which was distributed to each joint location of the square frame section. All of the joint locations were used because the turbine could be at any one of those locations throughout the operation process.

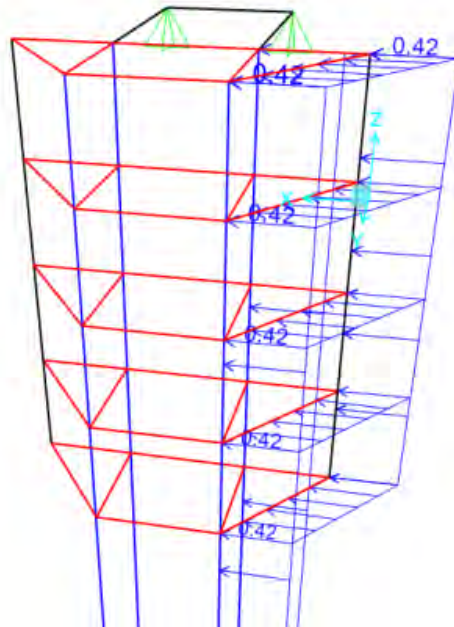


Figure 47: Water load.

As shown in Figure 47, the water load was distributed through the right side of the structure using a distributed load of 0.42 kips of force. This was distributed through every beam location on the right side of the structure.

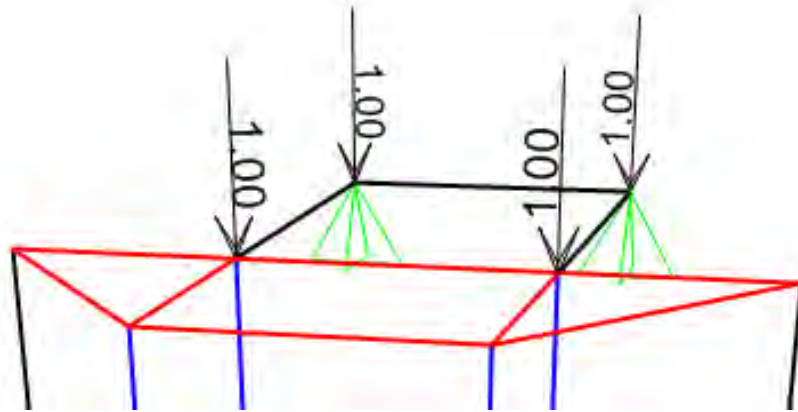


Figure 48: Generator load.

The final load was the generator/steel grate loading. The load assumed for the weight was one kip and was made into point loads throughout the platform area.

4.3.3c SIZING OF THE BEAMS

When determining the sizing of the beams, strength and feasibility were the priorities of design. To maximize power transfer to the turbine, the location of the frame must be as rigid as possible. Member sizes W12×96 were used for most of the middle trapezoid section where the turbine is located (as shown in Figure 49). The longer member that is closer to the pier was chosen to be a W40×362. This member is larger because it has a longer span and is closer to the connection point, therefore taking more of the load. These sizes were adequate enough to ensure that there would be minimal deflection under water loading, which was one of the most critical factors to be achieved in the design.

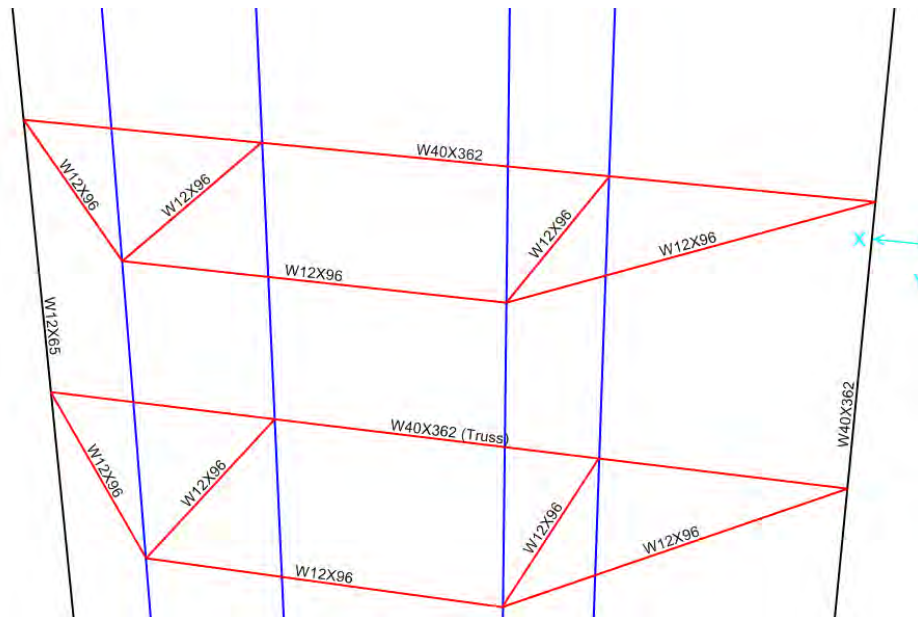


Figure 49: Mid-frame member sizes.

The member sizes were also chosen to be larger on the top, closer to the maintenance platform and transfer plate, because the load path of the forces travels to the two beams that connect to the transfer plate at the top of the structure. That caused the members on the top level, connecting to these two main beams, to be considerably larger than the rest of the frame. The three members that support the maintenance platform are W36×150 members as seen in Figure 50. These beams also connect to the transfer plate, so they will need to be strong enough to handle much of the loads.



Figure 50: Top-level member sizes.

These beams will be providing more support near the top of the structure meaning that less of the force will be transferred to the bottom pin connections. This is necessary because the bottom pin connections are meant less for vertical load support and more as a stabilizing mechanism.

Another factor of the design that made it easy to implement was that it is very symmetrical. The main frame is made of the same trapezoidal shape using the same member sizes. The vertical members are also the same size on either side, so the only members that are really a different size than the bulk of the frame are the top level beams that will be connected to the transfer plate. Having a symmetric structure will make the construction easier and provide less of a chance for installing improper members.

4.3.3d BEAM DEFLECTION

In order to analyze the deflections the structure will undergo, the program SAP 2000 was used. The deflections on the frame are shown as the change in shape caused by the different loadings. The deflected shape is grossly exaggerated in order to see the loading effects. As mentioned previously, the most important issue is to have minimal deflections in the central area where the turbine will be located. As seen by figure__ which shows the deflected shape caused by the force of water, the central trapezoid remains relatively undeformed while the longer support pin members bend to the side. This is acceptable because they do not carry a significant portion of the load.

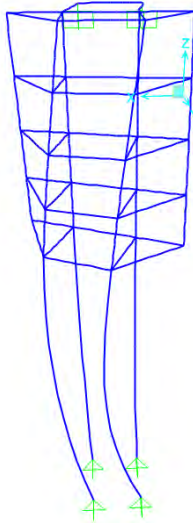


Figure 51: Deflected shape due to water loading.

The second analysis was done on the gravity loading of the turbine. Likewise, the main factor was to have a rigid main frame section so the turbine has optimal power transfer. The gravity load will not be as big of an issue because it would only cause the frame to deform downwards slightly.

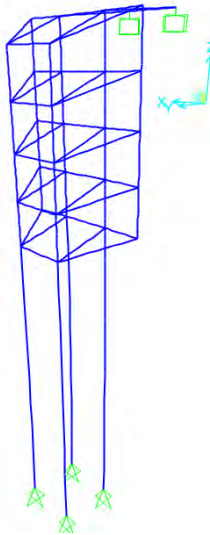


Figure 52: Deflected shape due to turbine load.

As seen by Figure 52 there is only a minimal noticeable deflection even with the largely exaggerated shape. This means the member sizing is sufficient to resist movement of the frame. When comparing the deflection effects of the water pressure and drag force to the turbine gravity load, it is clear that the water has a higher impact.

5 FUTURE WORK

When the size of the turbine was originally determined, it was based upon the size of the test turbine available for use. However, through further analysis, it should be noted that given the power density and proposed turbines cross sectional area perpendicular to the direction of current flow, the power available would only account for about 48% of the bridge's power requirements. Therefore, to generate the power needed, it is suggested that future design account for two of the 2.5m high by 1m diameter Gorlov style turbines. And for more in depth, blade design analysis, the following schematic and equations are provided.

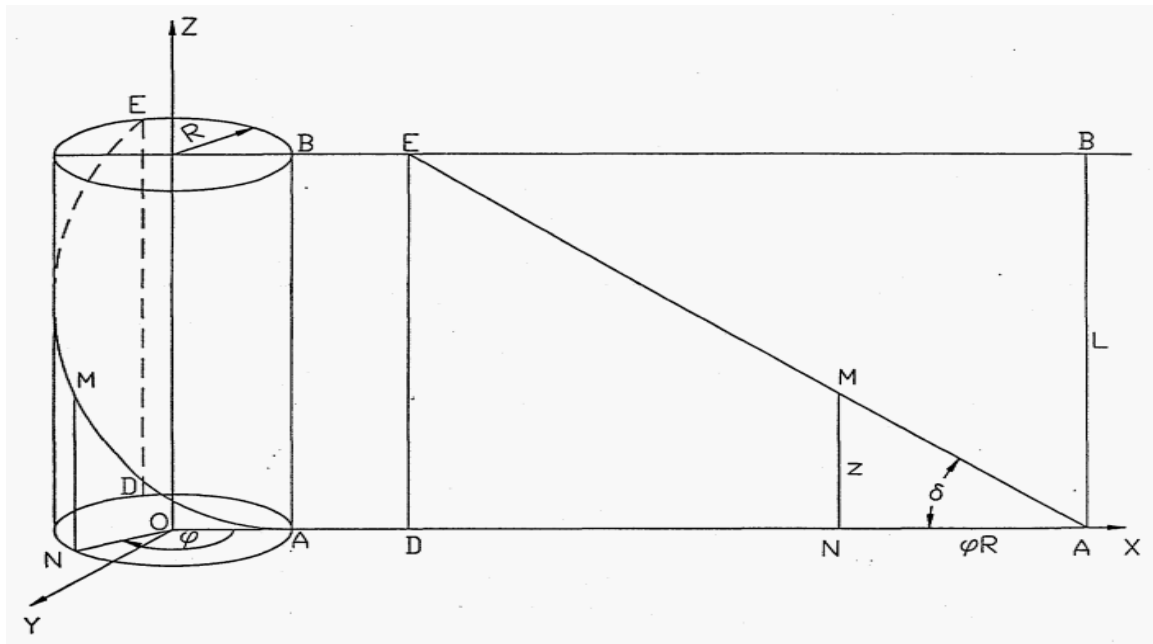


Figure 53: Schematic of Gorlov Turbine Showing Angle of Twist

The length of the turbine, L , is given by:

$$L = R\phi \tan(\delta), \quad 41$$

Where δ is the angle of pitch, R is the radius of the turbine and ϕ is the angle of twist. Torque, T , is then found using the following equation relating the above variables.

$$T = \sqrt{1 + q^2 \sin^2 \left(\frac{L}{R \times q} \right)} \quad 42$$

In addition, it is recommended to keep in mind that the bolts used for securing the hydrofoils have been known to fail.

Tips:

- Use finite element analysis or the magnetic lumped model to analyze generator static forces. Avoid using the method of co-energy for this type of geometry.

- Faraday's law remains an accurate way to predict voltage.
- Do not neglect fringing effects between the bottom edges of the C core and the magnets, other fringing effects may be neglected.
- To alleviate static cogging issues, use an odd number of C cores such that all of the magnets never fully align with the cores.
- Avoid using materials from past projects. They can limit your design, even if they may be more cost effective than buying/making more parts.
- Do not underestimate the power of rare earth magnets. The attractive force of the magnets which we used can reach an astounding 76 lbs of pull force! Forces that high are what caused the previous VFG group's project to break. Use high safety factors for parts dealing with magnetic forces.
- Attempt to make the length of the air gap as small as possible, large gaps are to magnetic systems what resistors are to electrical circuits. The smaller the gap, the better.
- Chase Hall is a relatively corrosive environment for metals. Avoid using any metal which is not stainless in Chase Hall for periods of time longer than 2 days.
- ME courses which are extremely useful and applicable to this project are: Introduction to Finite Elements, Renewable Energy, and Electromechanical analysis. Without those courses, it will be extremely difficult to understand the theoretical aspects of this project.
- Do not use magnetic materials anywhere near the magnets or cores; they may cause additional flux leakage.

6 REFERENCES

- [1] Notes/extra help from Professor Fussell
- [2] Notes/extra help from Professor Wosnik
- [3] Notes/extra help from Professor Korkolis
- [4] Quintal, Alex. "Hydrokinetic Turbine Featuring Variable Flux Generation." *UNH Tech 797 - Ocean Projects* (2010): n. pag. Print.
- [5] Allen, Nathaniel. "Hydrokinetic Turbine Featuring Variable Flux Generation." *UNH Tech 797 - Ocean Projects* (2011): n. pag. Print.
- [6] Khan, M.J., M.T. Iqbal, and J.E. Quaicoe. *Axial flow water and Cross flow turbines*. 2008. Photograph. ScienceDirect, St. John's. Web. 21 Sep 2012.
- [7] Bachant, Peter. Wosnik, Martin. "EXPERIMENTAL INVESTIGATION OF HELICAL CROSS-FLOW AXIS HYDROKINETIC TURBINES, INCLUDING EFFECTS OF WAVES AND TURBULENCE" Proceedings of ASME-JSME-KSME Joint Fluids Engineering Conference 2011
- [8] Bedard, Roger. Previsic, Mirko. Polagye, Brian. Hagerman, George. Casavant, Andre. Tarbell, Devine. "North America Tidal In-Stream Energy Conversion Technology Feasibility Study" EPRI. June 11, 2006.
- [9] <<http://www.sciencedirect.com/science/article/pii/S136403210700069X>>.
- [10] <<http://www.interfaceforce.com/t8-eco-rotary-torque-transducer-p-65.html>>.
- [11] <<http://www.jackxchange.com/catalog/product-chart.cfm?modelnumber=P12>>.

7 APPENDICES

7.1 DATA TABLES

B=0		B=.23		B=.48		B=.52		B=.645			
A (inches)	V (mV)	A (inches)	V (mV)	A (inches)	V (mV)	A (inches)	V (mV)	A (inches)	V (mV)		
0	0.46	0	-0.4	0	-0.4	0	-0.085	0	-0.45		
0.02	1.9	0.02	0.9	0.02	0.2	0.02	0	0.02	-0.2		
0.04	2	0.04	1.6	0.04	0.6	0.04	0.75	0.04	-0.1		
0.06	2.4	0.06	2.1	0.06	1.1	0.06	0.9	0.06	0.1		
0.08	2.9	0.08	2.6	0.08	1.6	0.08	1.05	0.08	0.3		
0.1	3.4	0.1	3	0.1	2.2	0.1	1.35	0.1	0.9		
0.12	3.8	0.12	3.4	0.12	2.5	0.12	1.8	0.12	1.3		
0.14	4.3	0.14	3.8	0.14	3.1	0.14	2.05	0.14	1.7		
0.16	4.8	0.16	4.3	0.16	3.3	0.16	2.3	0.16	2		
0.18	5.2	0.18	4.8	0.18	3.7	0.18	2.6	0.18	2.4		
0.2	5.6	0.2	5.2	0.2	4	0.2	3	0.2	2.75		
0.22	6	0.22	5.5	0.22	4.5	0.22	3.3	0.22	3.2		
0.24	6.4	0.24	5.9	0.24	4.9	0.24	3.55	0.24	3.45		
0.26	6.78	0.26	6.3	0.26	5.2	0.26	3.9	0.26	3.6		
0.28	6.7	0.28	5.9	0.28	5.4	0.28	4.1	0.28	3.9		
0.3	7.5	0.3	7	0.3	5.9	0.3	4.4	0.3	4.3		
0.32	7.7	0.32	7.4	0.32	5.9	0.32	4.65	0.32	4.7		
0.34	7.93	0.34	7.6	0.34	5.7	0.34	4.85	0.34	4.9		
0.36	8.28	0.36	7.8	0.36	6.1	0.36	5	0.36	5.2		
0.38	8.48	0.38	8.2	0.38	6.7	0.38	5.3	0.38	5.5		
0.4	8.88	0.4	8.4	0.4	7	0.4	5.5	0.4	5.75		
0.42	9.1	0.42	8.6	0.42	7.1	0.42	5.7	0.42	6		
0.44	9.4	0.44	8.4	0.44	7.4	0.44	5.9	0.44	6.4		
0.455	9.64	0.455	9	0.455	7.6	0.455	N/A	0.455	6.4		
				<i>Note: 0.237 in between magnet & core</i>							
A (inches)	V (mV)	A (inches)	V (mV)	A (inches)	V (mV)	A (inches)	V (mV)	A (inches)	V (mV)		
0.55	10.3	0.47	8.8	0.47	7.2	0.47	6.9	0.46	5.4		
0.57	11.5	0.49	9	0.49	7.8	0.49	6.5	0.48	5.8		
0.59	11.75	0.51	9.6	0.51	8.2	0.51	6.35	0.5	5.7		
0.61	11.75	0.53	9.6	0.53	8.45	0.53	7.4	0.52	5.4		
0.63	11.9	0.55	9.9	0.55	8.65	0.55	7.8	0.54	6		
0.65	11.9	0.57	10.1	0.57	8.35	0.57	7.3	0.56	6.1		
0.67	11.8	0.59	10.4	0.59	8.5	0.59	7.25	0.58	6.1		
0.69	11.8	0.61	10.5	0.61	8.9	0.61	7	0.6	6.2		
0.71	12	0.63	11	0.63	9.05	0.63	7.3	0.62	6.2		
0.73	12.2	0.65	10.8	0.65	9.1	0.65	7.55	0.64	6.4		
0.75	12	0.67	11.2	0.67	9.2	0.67	7.6	0.66	6.4		
0.77	12.15	0.69	11.3	0.69	9.2	0.69	7.7	0.68	6.45		
0.79	12.2	0.71	11.3	0.71	9.3	0.71	7.75	0.7	6.5		
0.81	11.7	0.73	11.5	0.73	9.35	0.73	7.8	0.72	6.5		
0.83	12.3	0.75	11.5	0.75	9.3	0.75	7.85	0.74	6.5		
0.85	12.3	0.77	11.6	0.77	9.3	0.77	7.8	0.76	6.45		
0.87	12.4	0.79	11.7	0.79	9.3	0.79	7.8	0.78	6.5		
0.89	12.4	0.81	11.8	0.81	9.25	0.81	7.75	0.8	6.2		
0.9	11.65	0.83	11.9	0.83	9.25	0.83	7.7	0.82	6.2		
0.92	11.7	0.85	11.9	0.85	8.8	0.85	7.6	0.84	6		
0.94	11.7	0.87	11.7	0.87	8.7	0.87	7.3	0.86	6		
0.96	11.1	0.89	11.8	0.89	8.8	0.89	7.4	0.88	5.1		
0.98	11	0.91	11.6	0.91	8.7	0.91	7.15	0.9	5		
1	10.3	0.93	11.3	0.93	8.35	0.93	7.05	0.92	4.9		
1.1	5.1	0.95	11.1	0.95	8.25	0.95	6.7	0.94	4.8		
1.2	2.9	0.97	10.6	0.97	7.5	0.97	6.5	0.96	4.6		
1.3	1.5	0.99	9.8	0.99	7.88	0.99	6.15	0.98	4.4		
1.4	1.25	1.1	4.9	1.1	7.3	1.1	2.8	1	4.1		
1.5	0.85	1.2	2.8	1.2	4.4	1.2	1.6	1.1	2.5		
		1.3	1.7	1.3	2.4	1.3	1	1.2	1.3		
		1.4	1.2	1.4	1.5	1.4	0.7	1.3	0.8		
		1.5	0.8	1.475	1	1.5	0.45	1.4	0.6		
				<i>Note: 0.09 in between</i>							

TRIAL 1			
Voltage [v]	Pressure [psi]	Engagement [in]	Force [lbs]
-0.2481	18	0	198.8039
-0.2336	95	0.04014615	1049.243
-0.2156	101	0.08998275	1115.511
-0.1577	106	0.25029048	1170.734
-0.1344	109	0.31480119	1203.868
-0.1106	110	0.38069625	1214.913
-0.0973	112	0.41751996	1237.002
-0.0785	113	0.46957152	1248.047
-0.0387	115	0.57976578	1270.136
-0.002	119	0.68137707	1314.315
0.0234	119	0.75170205	1314.315
0.0672	120	0.87297111	1325.359
0.1258	119	1.03521693	1314.315
0.1777	109	1.17891246	1203.868
0.2313	103	1.32731478	1137.6
0.2734	95	1.44387705	1049.243
TRIAL 2			
Voltage [v]	Pressure [psi]	Engagement [in]	Force [lbs]
-0.2133	101	0.09635076	1115.511
-0.1859	105	0.17221314	1159.689
-0.1578	108	0.25001361	1192.823
-0.1266	111	0.33639705	1225.957
-0.0699	113	0.49338234	1248.047
-0.0352	118	0.58945623	1303.27
0.0035	120	0.69660492	1325.359
0.0664	121	0.87075615	1336.404
0.1875	117	1.20604572	1292.225
0.2106	107	1.27000269	1181.779
0.2766	99	1.45273689	1093.422
TRIAL 3			
Voltage [v]	Pressure [psi]	Engagement [in]	Force [lbs]
-0.2332	20	1.84192916	220.8932
-0.2305	99	0.00747549	1093.422
-0.2016	102	0.08749092	1126.555
-0.1781	105	0.15255537	1159.689
-0.1477	113	0.23672385	1248.047
-0.1117	115	0.33639705	1270.136
-0.0848	118	0.41087508	1303.27
-0.0184	120	0.59471676	1325.359
0.0805	122	0.86854119	1347.449
0.1879	118	1.16589957	1303.27
0.2457	107	1.32593043	1181.779
0.2848	105	1.4341866	1159.689

7.2 EQUIPMENT LIST

- Interface force transducer
Model: SM-100
Capacity: 100lbf
- Chatillon mechanical force gauge
- Portable clamps
- Digital Multimeter
- Neodymium 42 one inch cubic magnet × 7
- Weights ranging from of 0 to 82 lbs
- Digital Calipers
- Block of Wood
- Interface series T8 ECO Rotary Torque Transducer

SPECIFICATIONS

ACCURACY – (MAX ERROR)

Combined Error–% FS ±0.25
Nonrepeatability–% ±0.05

TEMPERATURE

Effect on Zero–% RO/°C ±0.04
Effect on Output–%/°C ±0.02
Rated Range–°C +5 to +45
Operating Range–°C 0 to +60

ELECTRICAL

Torque Output–VDC ±5
Bandwidth, Hz 1 kHz-3dB
Supply Voltage–VDC..... 12 to 28
Supply Current–mA 90
Electrical Connection Integral cable,
3-ft

MECHANICAL

Safe Overload–% RO 180
Cyclic Load Rating–% RO..... ±70 peak
Max Speed - rpm Varies with
capacity,
see table
Shaft..... Stainless steel
Housing Aluminum

OPTIONS

Extra cable length

T8 LC ROTARY TORQUE TRANSDUCER
PERFORMANCE PARAMETERS

CAPACITY (Nm)	MAX RPM	SPRINGRATE (Nm/rad)	MOMENT OF INERTIA, J (Kgxm ²)		MAX. THRUST LOAD (N)
			Drive Side	Test Side	
0.2	8,000	1.6	1.6x10 ⁻⁶	1.0x10 ⁻⁶	20
0.5	8,000	9.6	1.6x10 ⁻⁶	1.0/10 ⁻⁶	30
1	8,000	3.6x10 ²	1.6x10 ⁻⁶	1.1x10 ⁻⁶	40
2	8,000	8.9x10 ²	1.6x10 ⁻⁶	1.1x10 ⁻⁶	40
5	8,000	8.9x10 ²	1.7x10 ⁻⁶	1.1x10 ⁻⁶	50
10	8,000	8.9x10 ²	1.7x10 ⁻⁶	1.1x10 ⁻⁶	50
15	8,000	8.4x10 ³	1.7x10 ⁻⁶	1.1x10 ⁻⁶	50
20	6,000	8.4x10 ³	4.2x10 ⁻⁵	2.1x10 ⁻⁵	1,600
50	6,000	8.4x10 ³	4.2x10 ⁻⁵	2.1x10 ⁻⁵	1,600
100	6,000	2.0x10 ⁴	4.7x10 ⁻⁵	2.7x10 ⁻⁵	3,000
200	6,000	2.0x10 ⁴	4.2x10 ⁻⁵	2.7x10 ⁻⁵	3,000

T8 INTEGRAL CABLE WIRING CODE

Function	Description	Color
Supply (+)	12 to 28 VDC	Brown
Supply (GND)	0 VDC	Green
Signal (+)	±5 VDC	Yellow
Signal (GND)	0 VDC	White
Shield	Shield	Shield

- Servo Motor
- 6" LVDT
- Hydraulic hand pump single speed
Model: P159

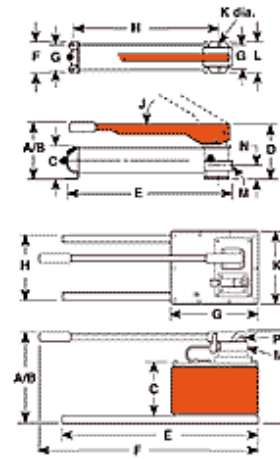
DIMENSIONS (INCHES)

Pump No.	A	B	C	D	E	F	G	H	J	K	L	M	N	P
P12	4.00	—	—	4.00	13.50	3.38	2.19	—	45°	0.19	3.38	—	1.13	—
P19	5.50	14.63	2.88	4.56	13.69	4.00	3.25	11.06	53°	0.31	4.00	½" NPTF	1.41	—
P23	6.25	13.00	3.50	5.56	13.63	4.25		10.31	38°		4.75		1.63	
P55	6.50	21.00		5.00	23.00			4.25			19.75		4.50	
P59	7.00		6.00	23.25	20.25	—			4.50		1.69			
P157/ P159	7.75	20.50	4.88	6.88	22.75	3.88	3.00	19.75	39°	0.31	3.75	½" NPTF	2.25	—
P300	8.25	21.00	4.50		22.63	8.50	7.50 3.00	20.72			2.25			
P460	11.13	31.00	6.75	11.38	24.00	29.25	11.00	9.00	80°	9.50	—	—	—	0.25

ORDERING INFORMATION

See current price list for shipping weights.

For Use With	Order No.	Volume & Pressure			Handle Effort (lbs.)	Reservoir (cu. in.)		Oil Port	Product Weight (lbs.)
		Stage	Volume per Stroke (cu. in.)	Maximum Pressure (psi)		Oil Capacity	Usable Oil Capacity		
Single-Acting Cylinders (Pump includes 2-Way Valve)	P12	1	0.069	10,000	75	12.0	9.0	½" NPTF	5.7
	P19	1	0.305	325	99	24.4	20.0		6.6
		2	0.076	10,000					6.6
	P23	1	0.160	3,000	70	23.8	20.3		12.0
	P55	1	0.160	10,000	145	55.0	45.0		15.8
	P59	1	0.662	325					17.2
			0.160	10,000					17.2
	P59F	1	0.550	325	140	152.0	137.0		14.0
	2	0.130	10,000	14.0					
P157	1	0.650	1,400	140	152.0	137.0	26.7		
2	0.160	10,000	26.7						
P159	1	2.600	325	90	2.5 gal.	460.0	26.2		
2	0.160	10,000	26.2						
P300	1	2.600	325	90	2.5 gal.	460.0	55.3		
2	0.160	10,000	55.3						
P460	1	7.350	325	90	2.5 gal.	460.0	54.9		
Double-Acting Cylinders (Pump includes 4-Way Valve)	P157D	1	0.650	1,400	140	152.0	137.0	28.8	
			0.160	10,000				28.8	
	P159D	1	2.600	325	140	1.5 gal.	310.0	27.9	
			0.160	10,000				27.9	
P300D	1	2.600	325	90	2.5 gal.	460.0	57.0		
2	0.160	10,000	57.0						
P460D	1	7.350	325	90	2.5 gal.	460.0	57.9		
2	0.294	10,000	57.9						



List of Ordered Parts:

Place of order: McMaster-Carr

Please order 1 of these

Item #: 92620A673

Grade 8 Alloy Steel Hex Head Cap Screw Zinc Yellow Pltd, 7/16"-14 Thrd, 1-1/2" L, Fully Thrd

Price: \$13.95

Place of order: McMaster-Carr

Please order 1 of these

Item #: 91257A687

Grade 8 Alloy Steel Hex Head Cap Screw Zinc Yellow-Plated, 7/16"-14 Thread, 4-1/2" Length

Price: \$6.94

Place of order: McMaster-Carr

Please order 1 of these

Item #: 91257A688

Grade 8 Alloy Steel Hex Head Cap Screw Zinc Yellow-Plated, 7/16"-14 Thread, 4-3/4" Length

Price: \$10.34

Place of order: McMaster-Carr

Please order 1 of these

Item #: 94895A817

Zinc & Yellow Plated Grade 8 Steel Hex Nut 7/16"-14 Thread Size, 11/16" Width, 3/8" Height

Price: \$7.52

Place of order: McMaster-Carr

Please order 1 of these

Item #: 91251A194

Black-Oxide Alloy Steel Socket Head Cap Screw 8-32 Thread, 1/2" Length

Price: \$12.15

Place of order: McMaster-Carr

Please order 1 of these

Item #: 90715A009

Type 316 SS Nylon-Insert Hex Locknut 8-32 Thread Size, 11/32" Width, 15/64" Height

Price: \$9.04

Place of order: McMaster-Carr

Please order 1 of these

Item #: 98970A132

Hot Dipped Galvanized Steel Flat Washer USS, 7/16" Screw Size, 1-1/4" OD, .06"-.11" Thk

Price: \$9.55

Place of order: McMaster-Carr

Please order 1 of these

Item #: 92620A667

Grade 8 Alloy Steel Hex Head Cap Screw Zinc Yellow Pltd, 7/16"-14 Thrd, 3/4" L, Fully Thrd

Price: \$10.51

Place of order: McMaster-Carr

Please order 1 of these

Item #: 92620A744

Grade 8 Alloy Steel Hex Head Cap Screw Zinc Yellow Pltd, 1/2"-20 Thrd, 1" L, Fully Thrd

Price: \$14.13

Place of order: McMaster-Carr

Please order 1 of these

Item #: 94895A825

Zinc & Yellow Plated Grade 8 Steel Hex Nut 1/2"-20 Thread Size, 3/4" Width, 7/16" Height

Price: \$8.41

Place of order: McMaster-Carr

Please order 1 of these

Item #: 6527K324 (Please select the 3 foot length)

Low-Carbon Steel Square Tube 1-1/2" W, 1-1/2" H, .120" Wall Thickness

Price: \$21.22

Place of order: <http://www.motionindustries.com/motion3/jsp/mii/index.html>

Please order 2 of these

Item #: 03193750 (Motion Part Number)

FYH Bearings

UCF205-16E 1 4-BOLT FLANGE BRG

Place of order: McMaster-Carr

Please order 1 of these

Item #: 2722T21

Even-Grip Cast Iron Base-Mnt STL Ball Bearing Base-Mount for 1" Shaft Diameter

Price: \$74.40

Place of order: McMaster-Carr

Please order 1 of these

Item #: 1388K177

Low-Carbon Steel Sheet 1/4" Thick, 12" X 36", Ground Finish

Price: \$171.86

Place of order: McMaster-Carr

Please order 1 of these

Item #: 91251A014

Black-Oxide Alloy Steel Socket Head Cap Screw 1/2"-20 Thread, 1-1/4" Length

Price: \$9.11

Place of order: Provided by New England Wire Technologies

High-grade Hardened Steel Pins 1/4" diameter, 5/8" long

Place of order: Provided by New England Wire Technologies

O2 Tool Steel Used for shear pin, 1/8" diameter, 3.1" long

Place of order: Provided by New England Wire Technologies

Steel Plate, 11" x 10" X 1/2"

Place of order: Provided by New England Wire Technologies

Steel Plate, 13" x 11" X 1/4"

Place of order: Provided by New England Wire Technologies

Steel Plate, 9" x 8" X 1/2"

Place of order: Provided by New England Wire Technologies

Square Steel Tube, 1.5" X 1.5" X 36"

Other parts ordered/bought that weren't factored into the budget:

- 2 Hydraulic couplings
- L090 LoveJoy Jaw Coupling with 1 inch bore
- L110 LoveJoy Jaw Coupling with 1 inch bore
- 29/64" metal cutting drill bit
- 7/16" metal cutting drill bit
- 9/16" metal cutting drill bit
- Epoxy

Materials and Costs				
Item	Quantity	Unit Price	Cost	
Oil-Impregnated Bronze for Adapter Sleeve	1	81.4	81.4	
Drive Shaft	1	34.06	34.06	
Steel Stock for Adapter Mount	1	74.81	74.81	
Spring Pins	1	3.53	3.53	
Magnets	15	23.28	349.2	
Ball Bearing (vertically mounted)	1	103.14	103.14	
Total Shipping/Handling	1	15.15	15.15	
Magnet Mount	7	44	308	Total:
Magnet Placer	7	20	140	448
Magnet Mount	15	40	600	Total:
Magnet Placer	15	15	225	825
Miter Gear	2	70.3	140.6	
Screws (7/16"-14 -- .75" long)	1	10.51	10.51	
Screws (7/16"-14 -- 1.5" long)	1	13.95	13.95	
Screws (7/16"-14 -- 4.5" long)	1	6.94	6.94	
Screws (7/16"-14 -- 4.75" long)	1	10.34	10.34	
Nuts (7/16")	1	7.52	7.52	
Screws, Socket Cap (8-32 -- .5" long)	1	12.15	12.15	
Screws, Socket Cap (1/2" -- 1.25" long)	1	9.11	9.11	
Locknuts (8-32)	1	9.04	9.04	
Washers (7/16")	1	9.55	9.55	
Steel Tube (square) - 1.5"x1.5" -- 3 ft	1	21.22	21.22	
Base Plate (12" x 36" x 1/4")	1	171.86	171.86	
Delrin Bushing Material	1	38.29	38.29	
Ball Bearing (horizontally mounted)	2	22.47	44.94	
LoveJoy L110 Jaw Coupling w/ 1" Bore	1	36.7	36.7	
Delrin Bushing Machining	1	80	80	
		Total Cost (Before Magnet Holders):	1284.01	
		Total Cost (W/ 7 Magnet Holders):	1732.01	
		Total Cost (W/ 15 Magnet Holders):	2109.01	

7.3 SAMPLE CALCULATIONS

Shaft torque: $C_p = .27$

$$\lambda = \frac{\omega D}{2U_\infty} \quad \lambda = 2.1$$

$$P = T\omega \quad P = 1027 \frac{\text{kg}}{\text{s}}$$

$$C_p = \frac{P}{\frac{1}{2} \rho A U_\infty^3} \quad D = 1 \text{ m}$$

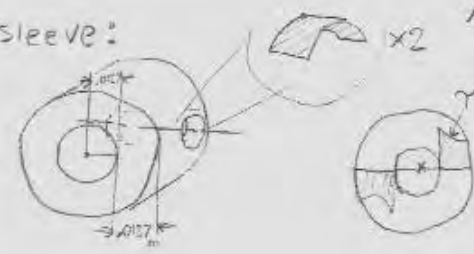
$$\quad \quad \quad \downarrow \quad H = 1.25 \text{ m}$$

$$\quad \quad \quad D \cdot H \quad U_\infty = 2 \text{ m/s}$$

$$\frac{2\lambda U_\infty}{D} = \omega, \quad P = C_p \cdot \frac{1}{2} \rho D H U_\infty^3 \quad T = \frac{P}{\omega}$$

$$T = \frac{C_p \cdot \rho D^3 H U_\infty^2}{4\lambda} = \frac{.27 \cdot 1027 \cdot 1^2 \cdot 1.25 \cdot 2^2}{4 \cdot 2.1} \approx 165 \text{ N}\cdot\text{m}$$

sleeve: $A = \frac{\pi}{4} L d = \frac{\pi}{4} \cdot .0127 d \approx .001 d \text{ m}^2$



$$T = P \cdot X \rightarrow P = \frac{T}{X}$$

$$P = \frac{165}{.0127} \approx 13000 \text{ N}$$

$$\tau = \gamma = \frac{P}{A} \text{ (pure shear)}$$

$$\sigma = \frac{13000}{.001 d} = 1.3 \cdot 10^7 \frac{1}{d}$$

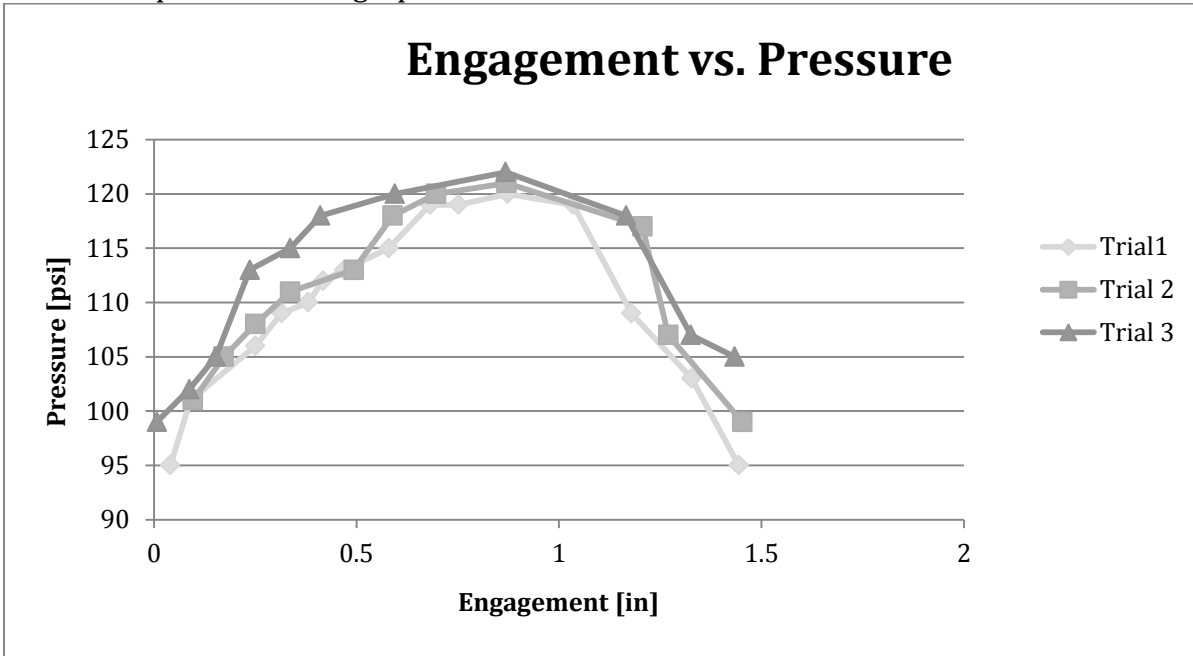
assume γ_s bronze or equivalent = 11000 psi = $7.584 \cdot 10^7 \text{ Pa}$

$$\frac{\gamma_s}{\sigma} = S_f = \frac{7.584 \cdot 10^7}{\frac{1.3 \cdot 10^7}{d}} = 5.833 d, \text{ but there are 2 holes,}$$

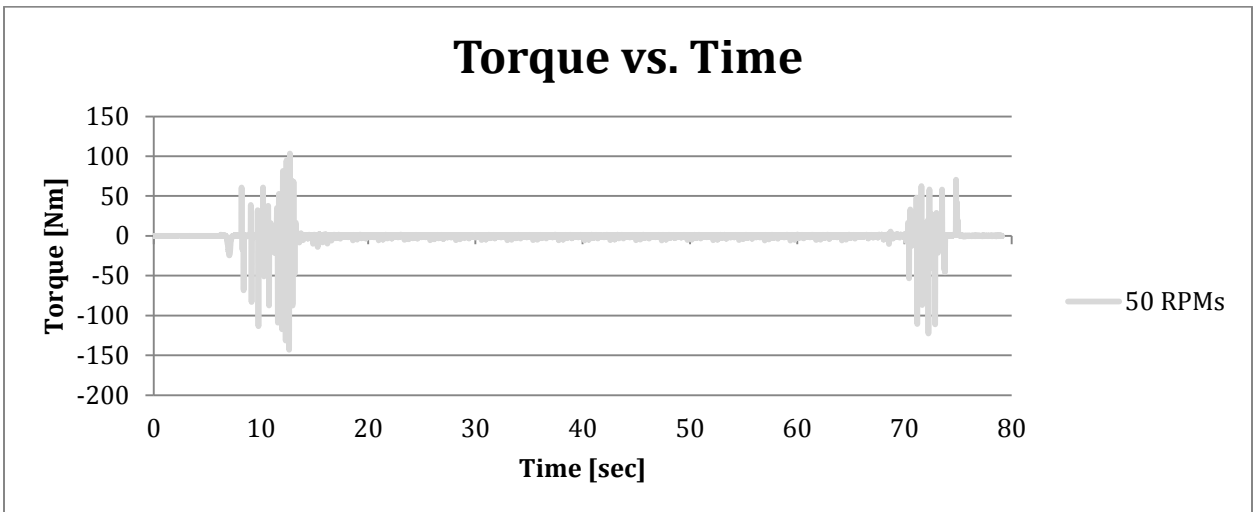
so $S_f = 2 \cdot 5.833 d = 11.668 d$

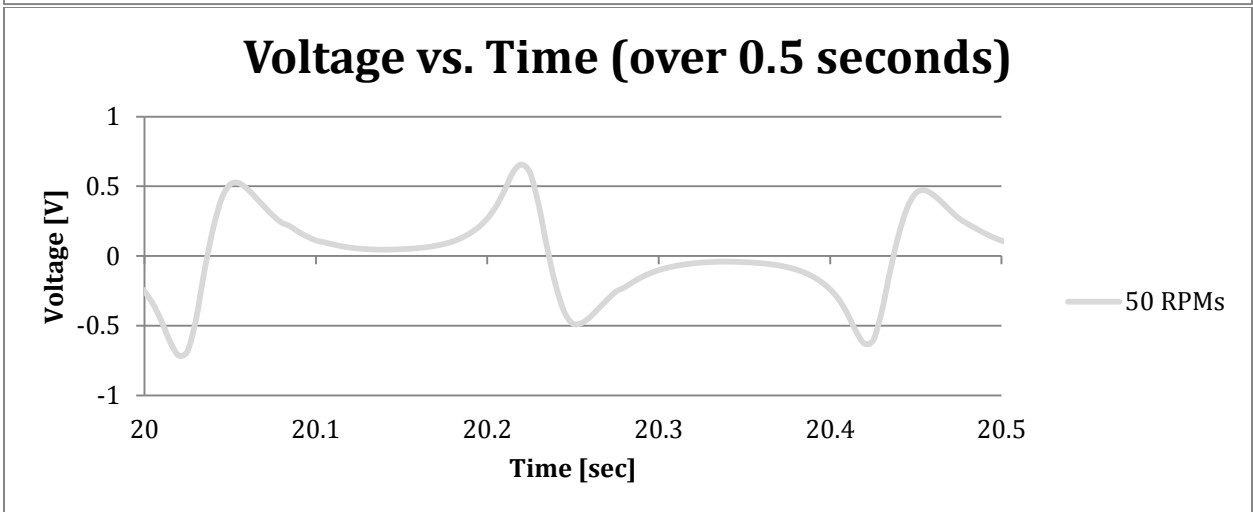
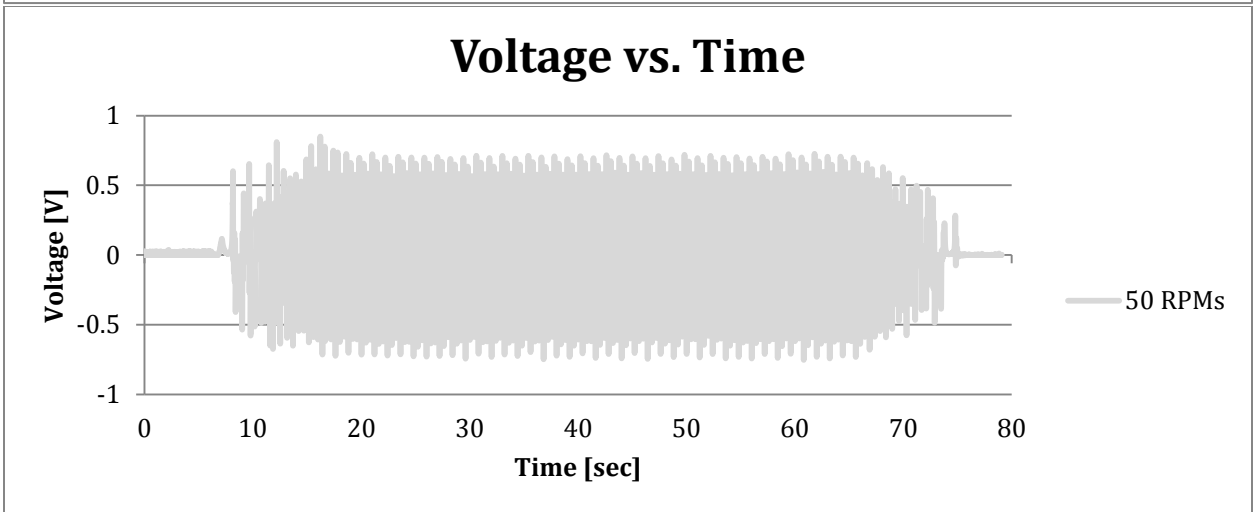
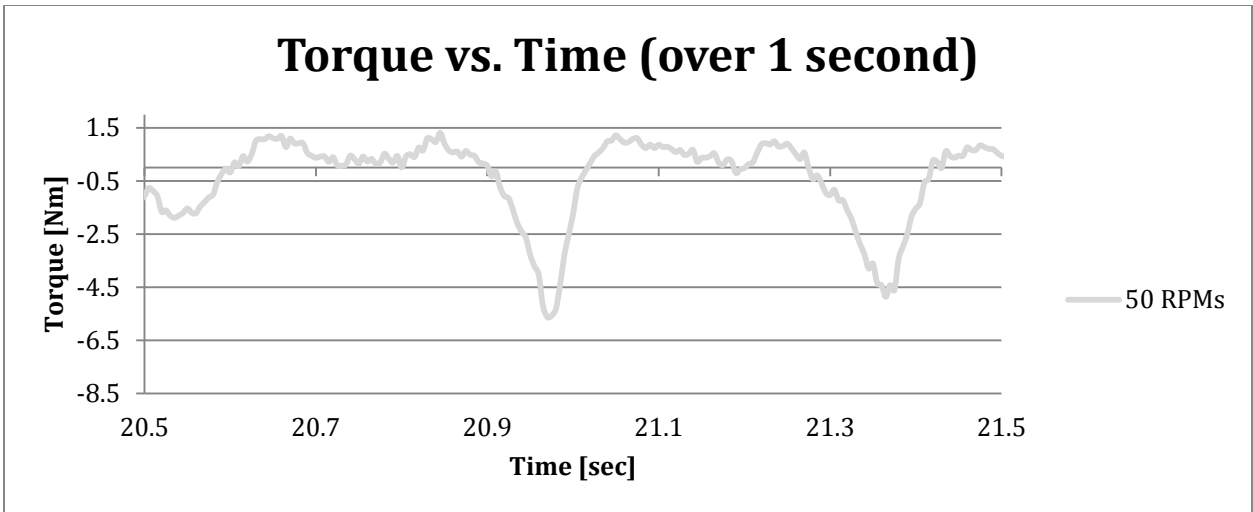
assume $S_f = 1 \rightarrow d = .0857 \text{ m} \rightarrow \text{problem,}$
 shaft dia = .0508

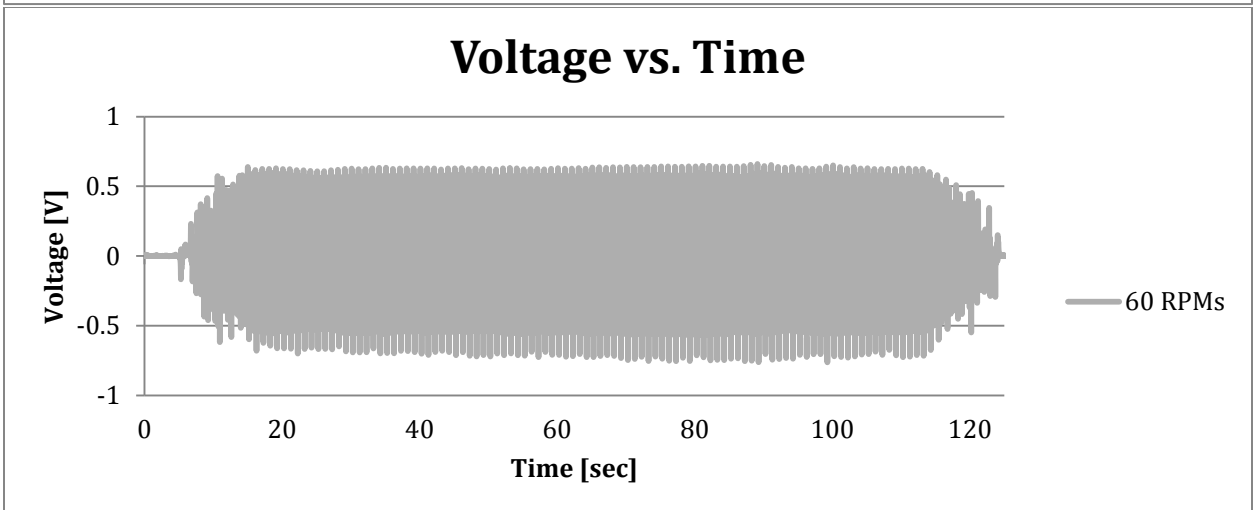
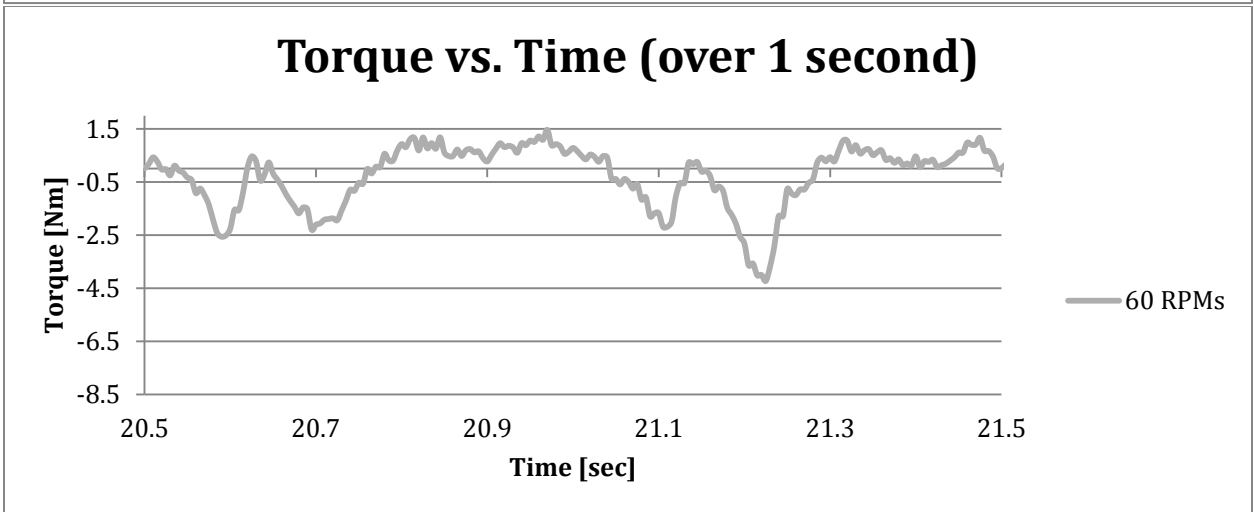
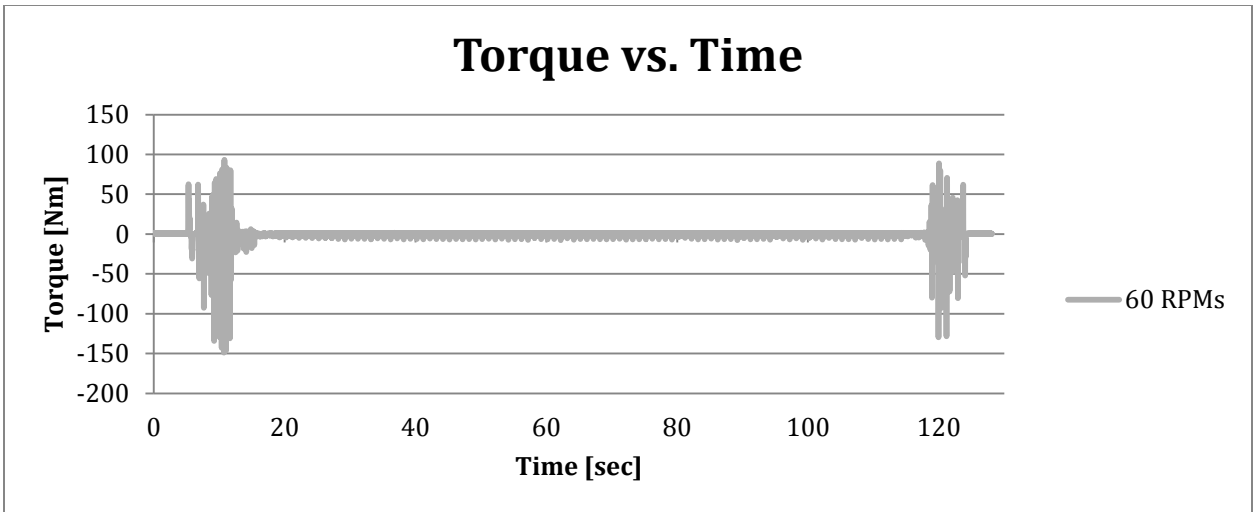
Pressure was found in terms of engagement displacement using the hydraulic actuator for three trials in which the process was repeated to ensure consistency in the results provided. The graph of this is shown below.



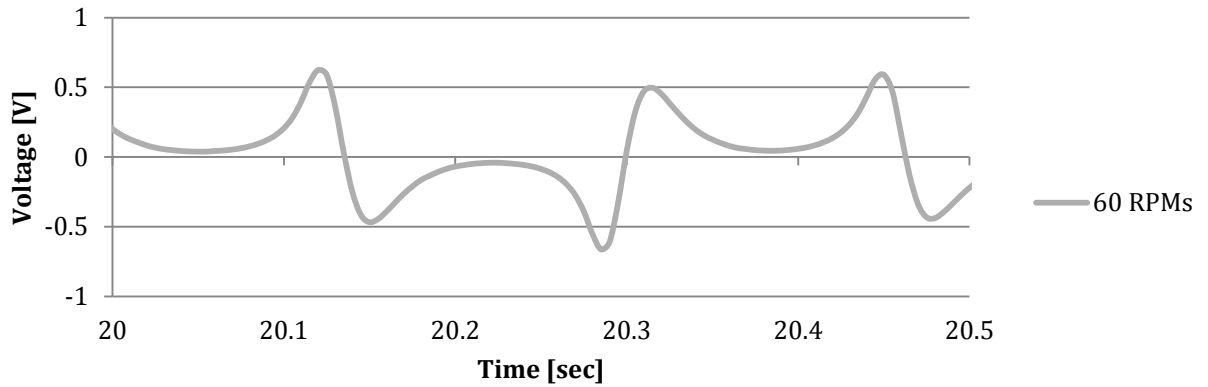
With this data and the hydraulic pump specifications (diameter of the cylinder was 3.75 in), a plot of engagement vs. force was found and shown in the following figure. Once the entire experimental setup was assembled, torque, rpm, and output voltage were recorded over a 4 Ω resistor (using the resistor bank) at an engagement of 1 inch and frequency of 200 Hz. The first graphs show data gathered from the 50 rpm run.



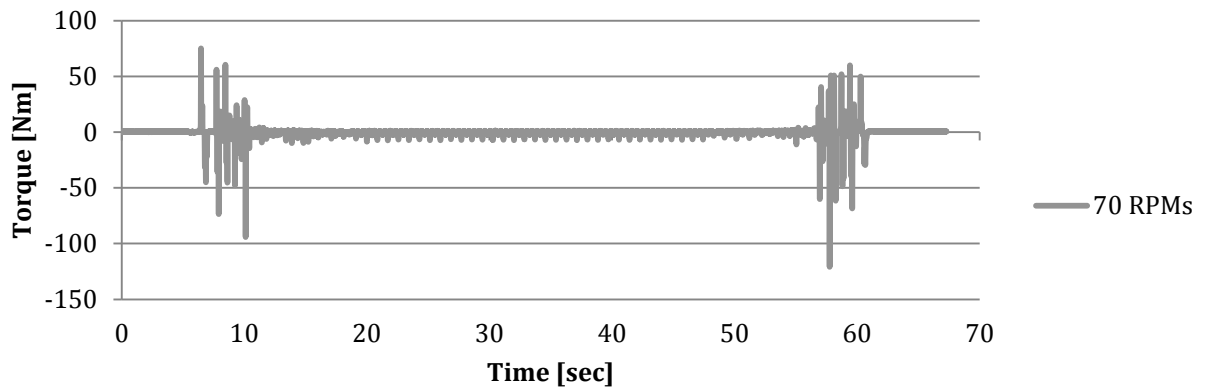




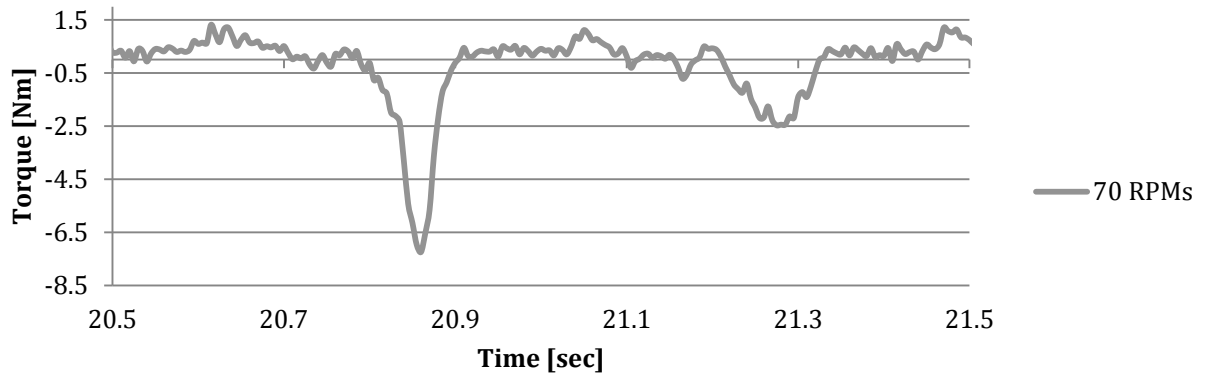
Voltage vs. Time (over 0.5 seconds)

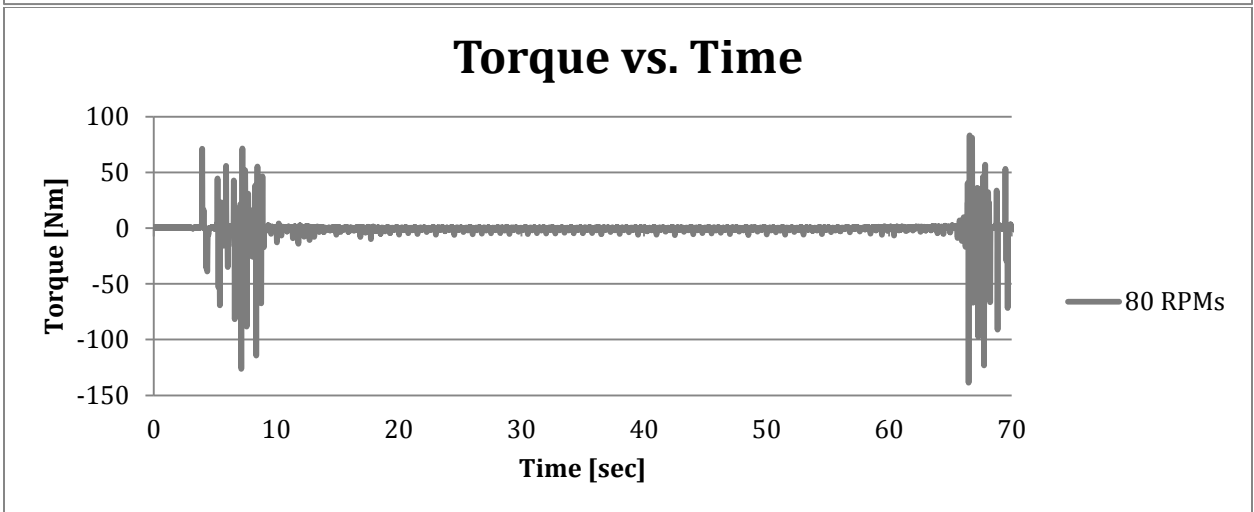
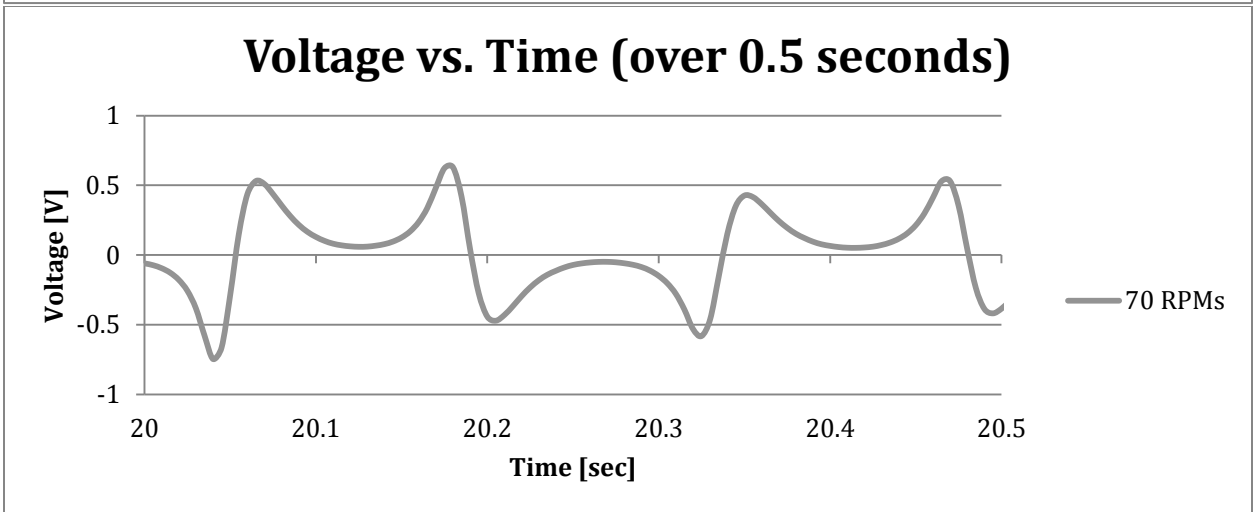
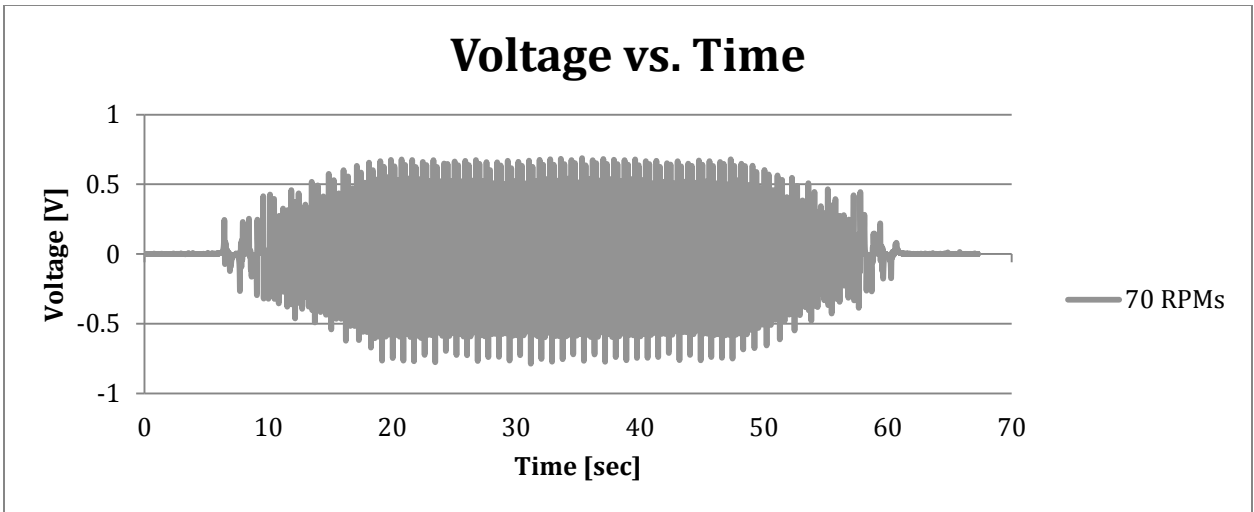


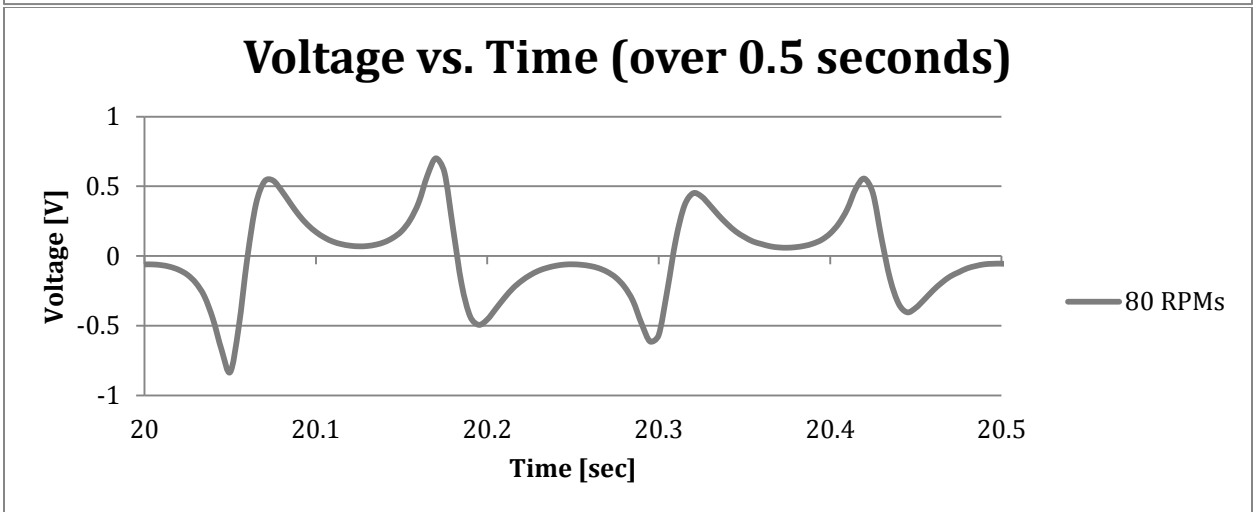
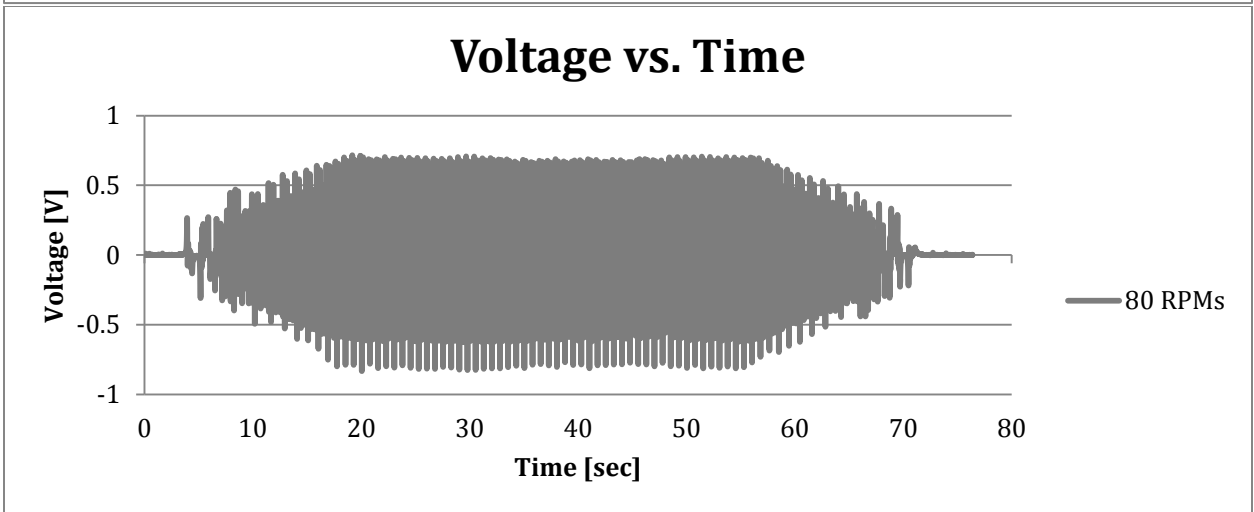
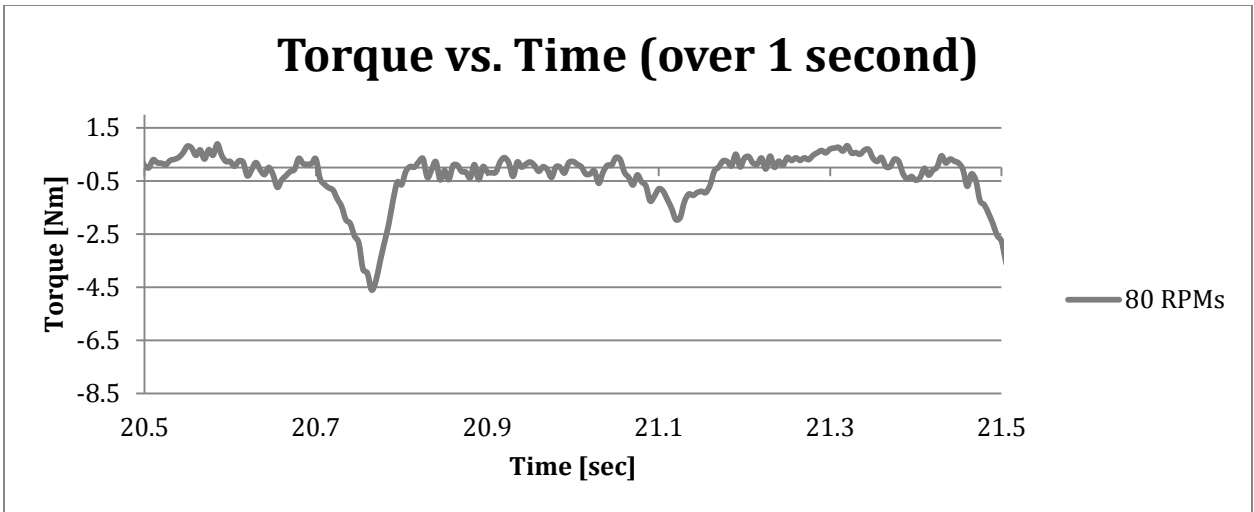
Torque vs. Time

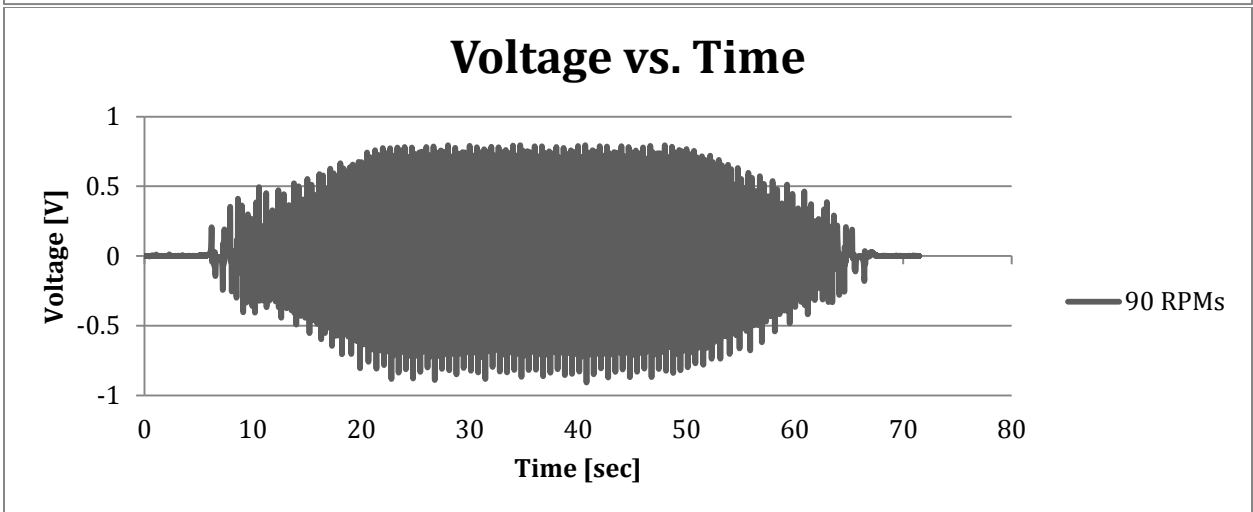
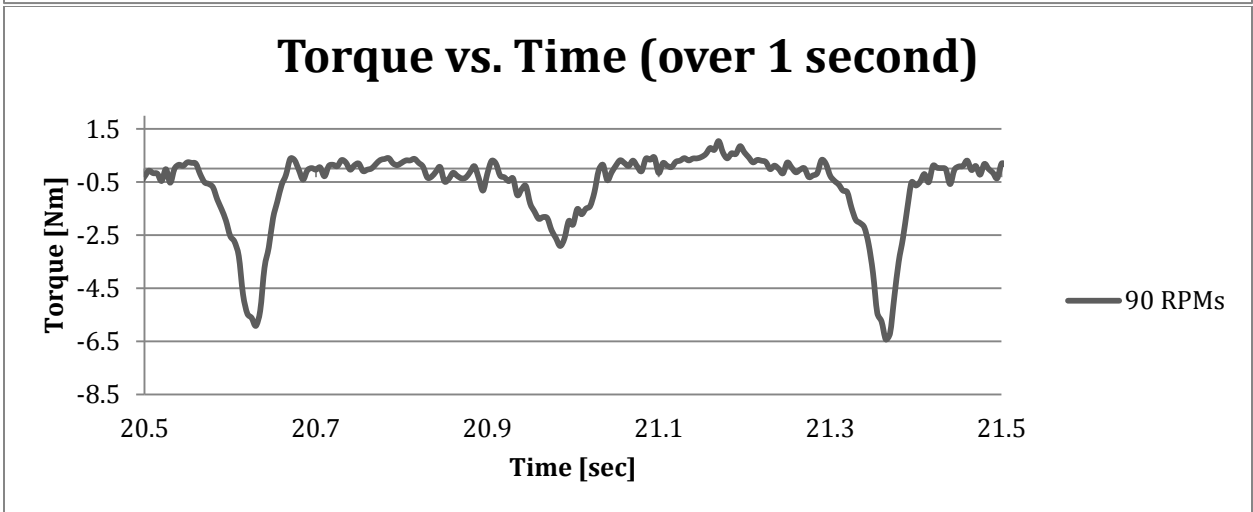
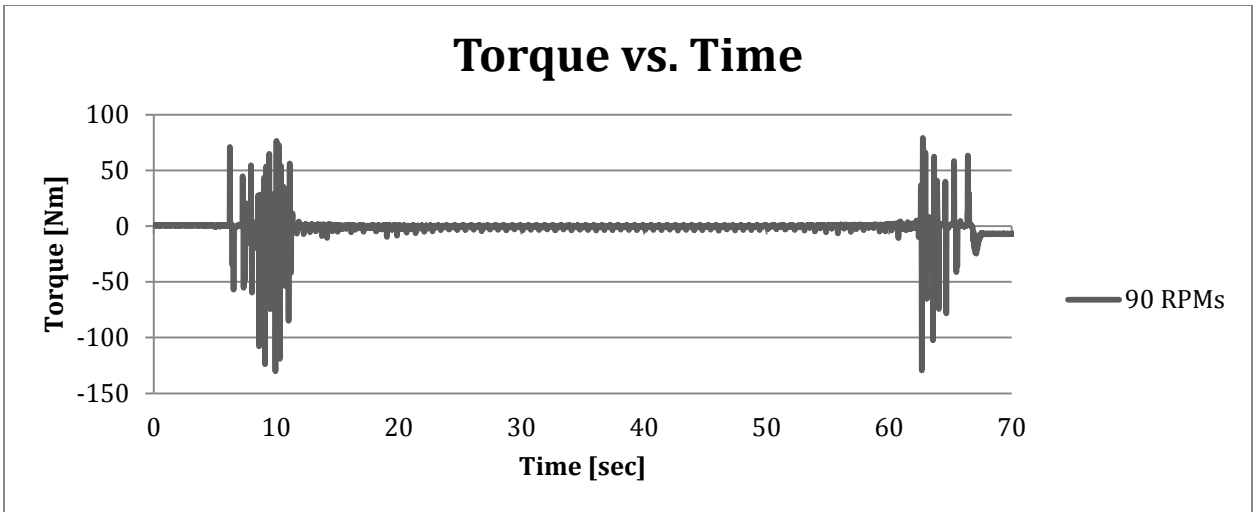


Torque vs. Time (over 1 second)

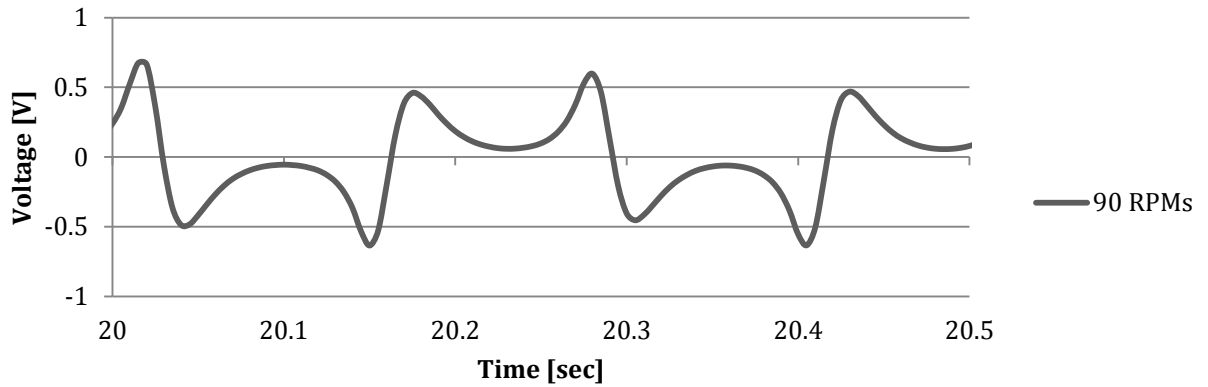




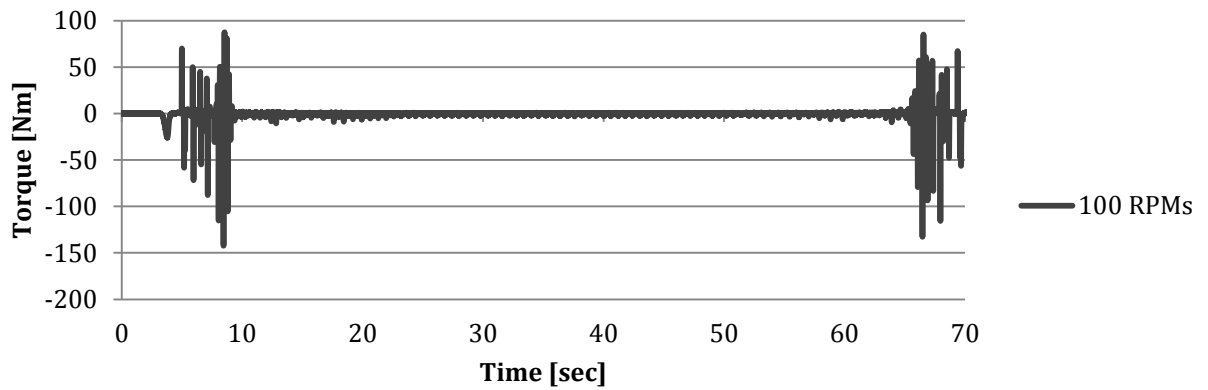




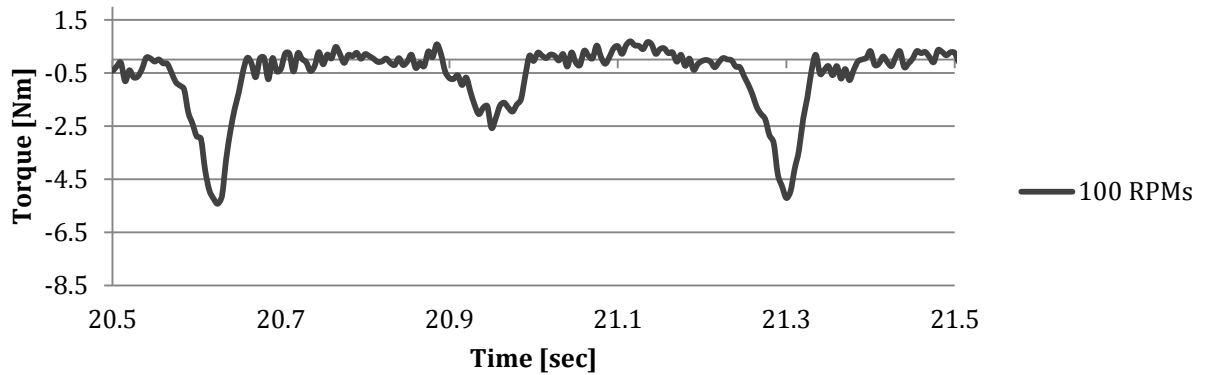
Voltage vs. Time (over 0.5 seconds)

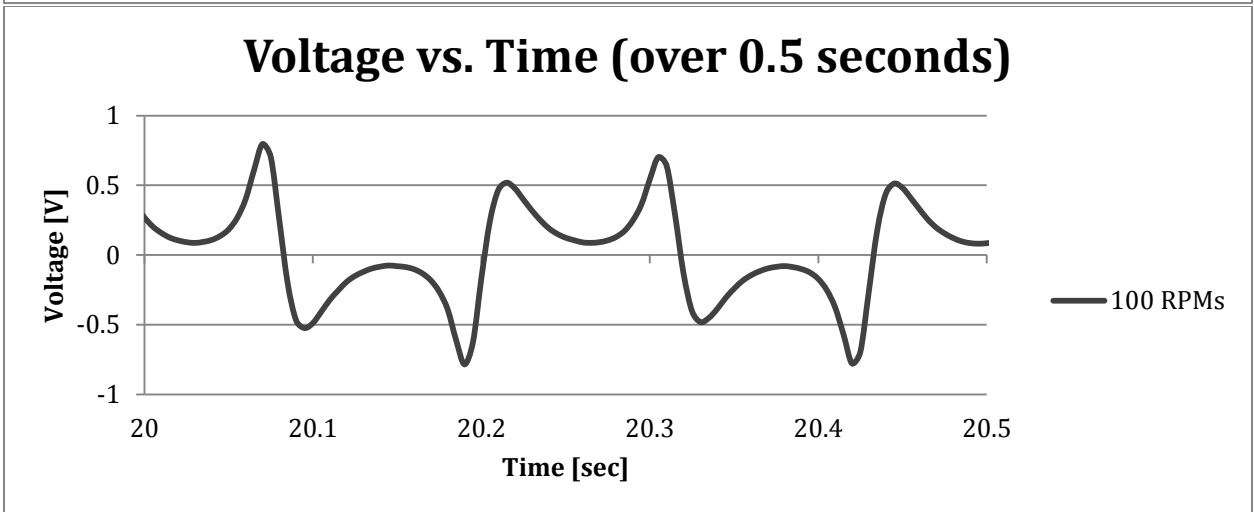
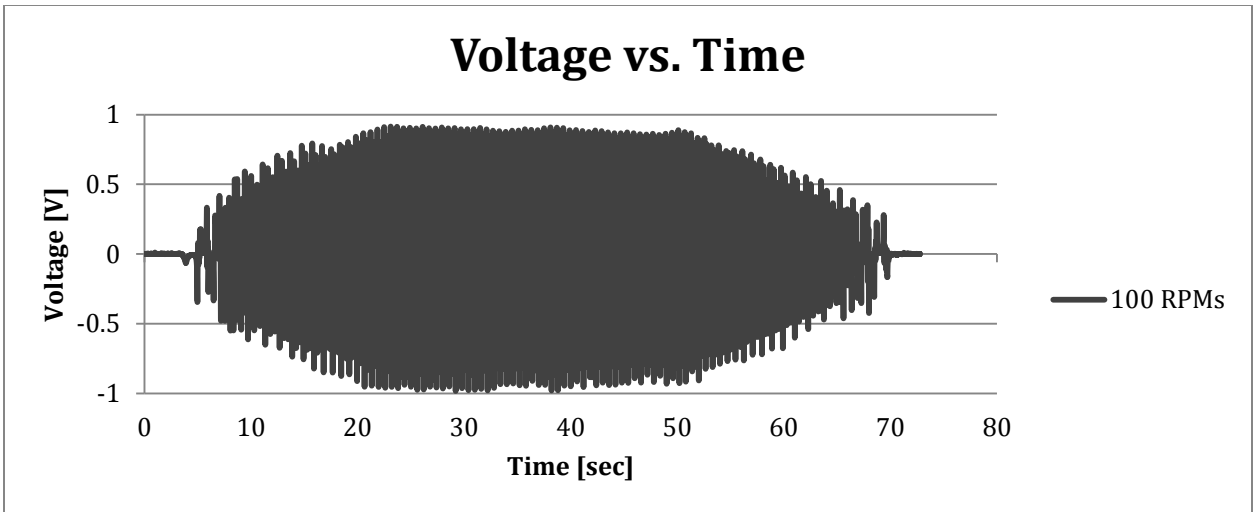


Torque vs. Time



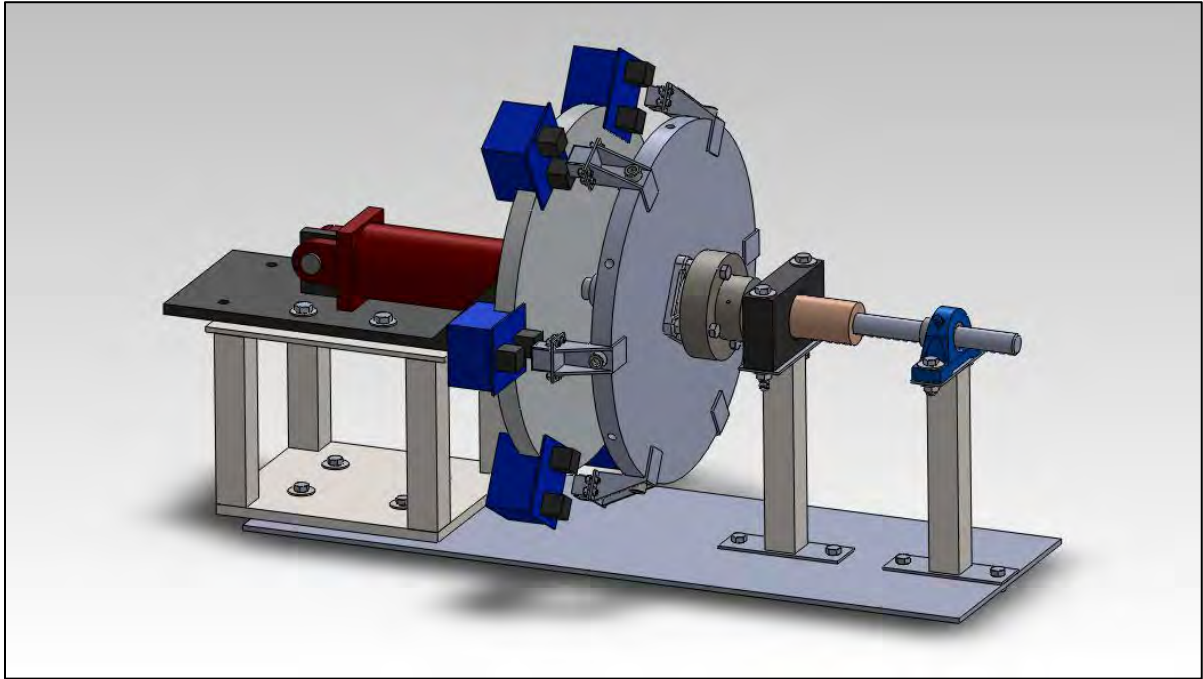
Torque vs. Time (over 1 second)



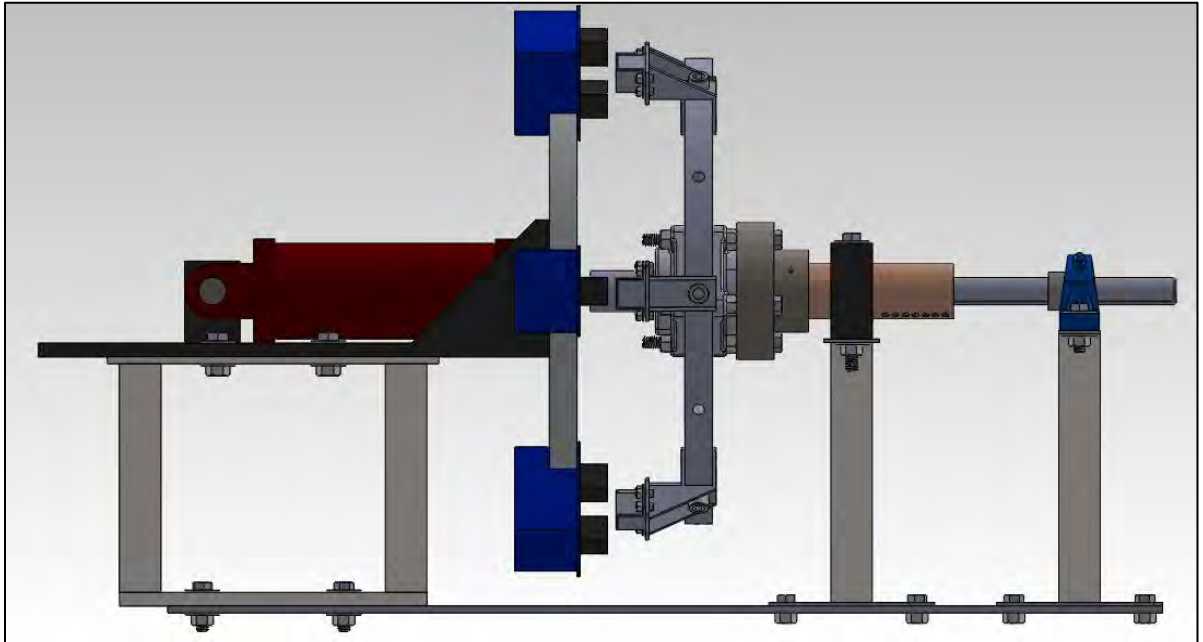


7.4 SOLIDWORKS DRAWINGS

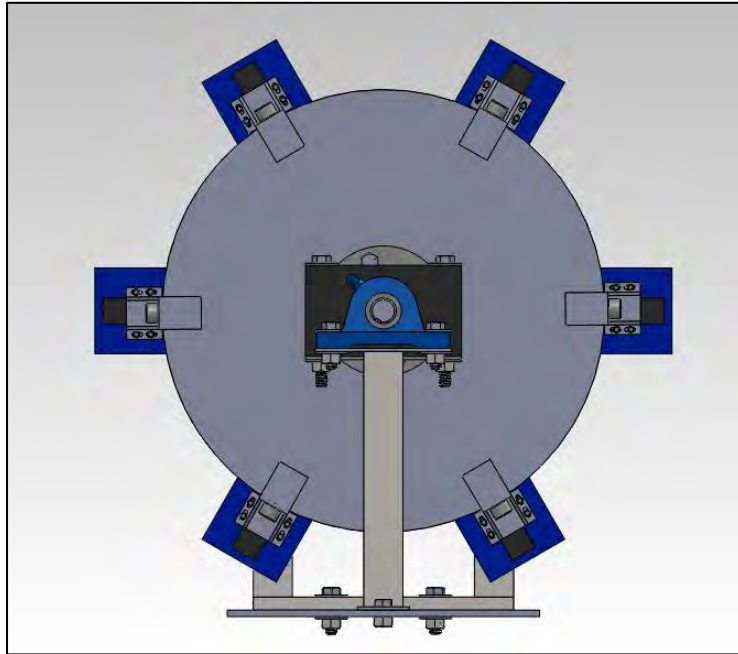
Isometric View



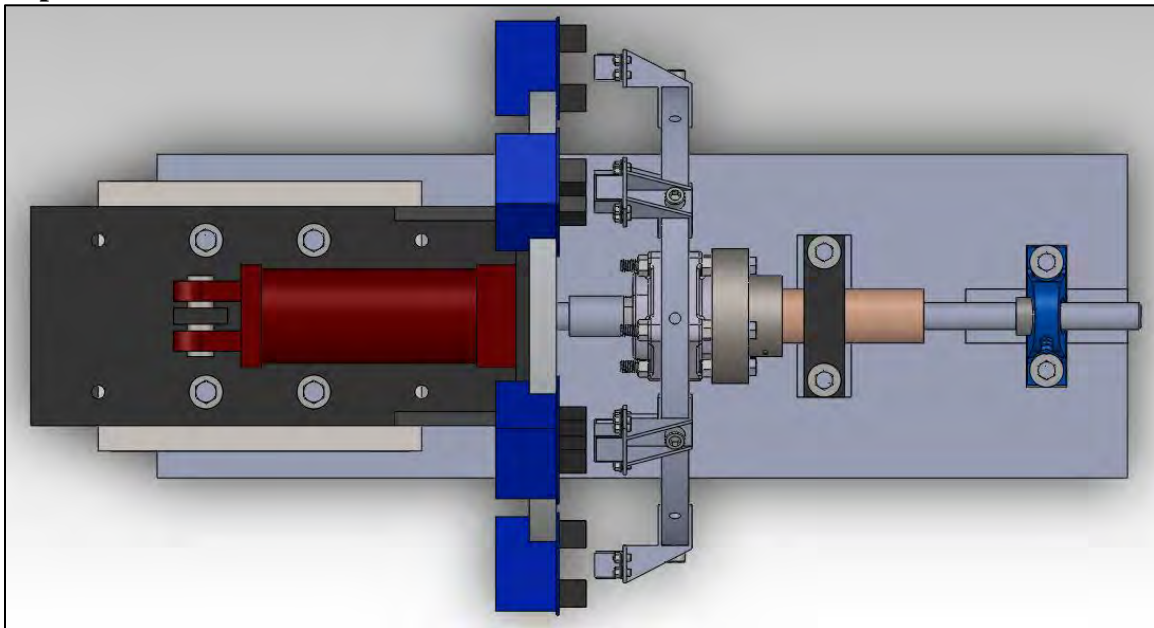
Side View



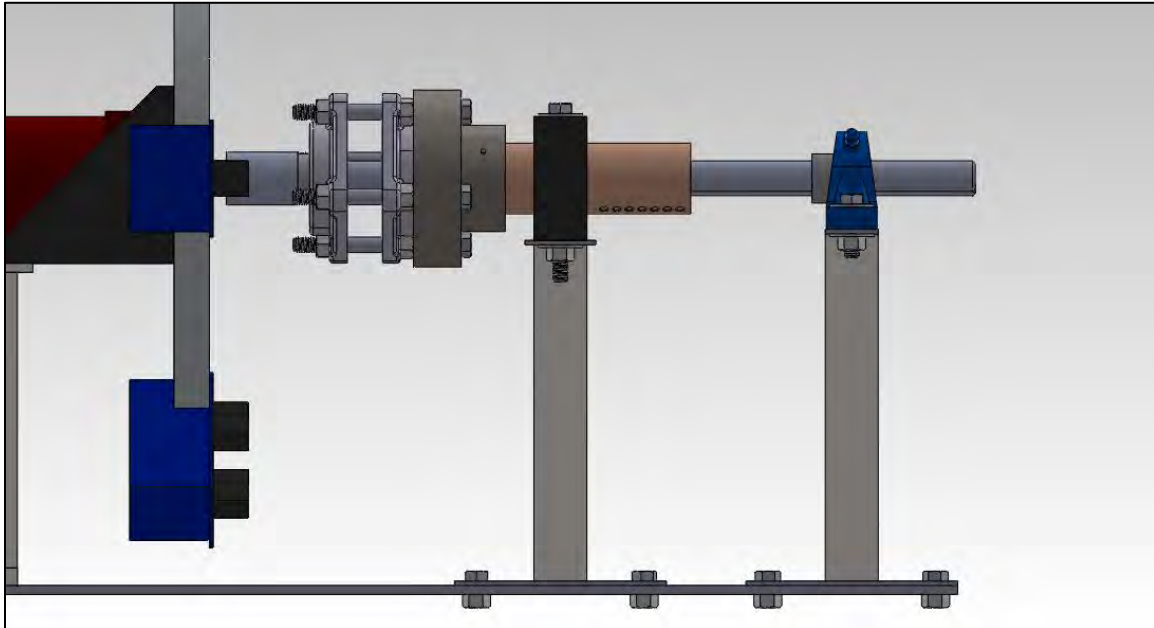
Front View



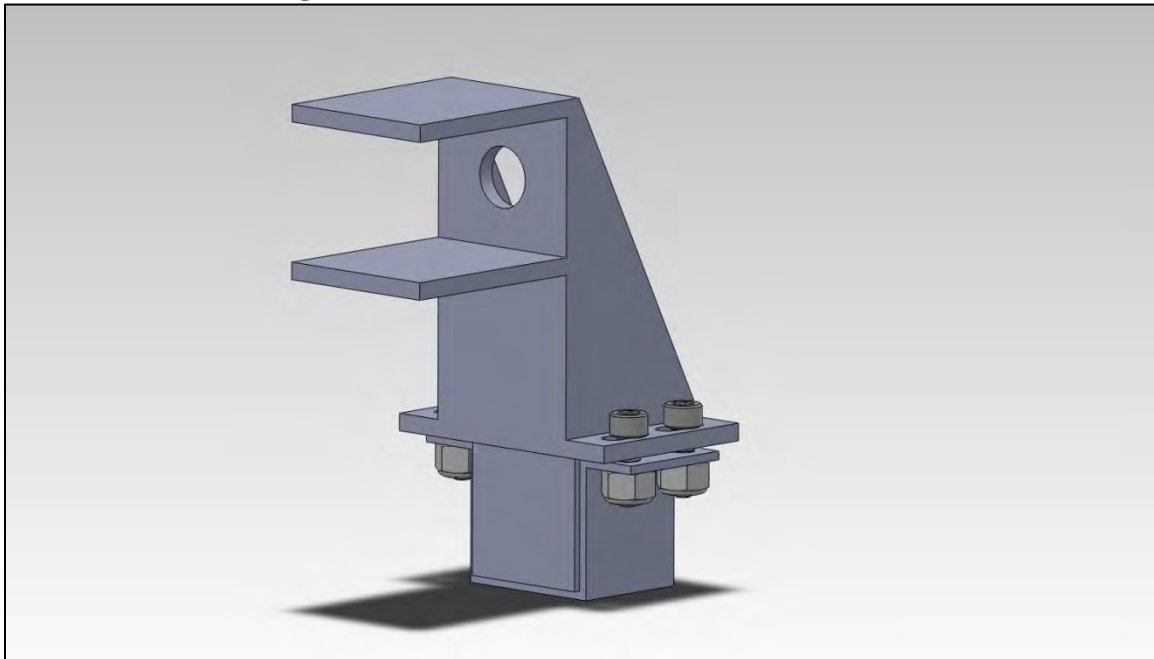
Top View



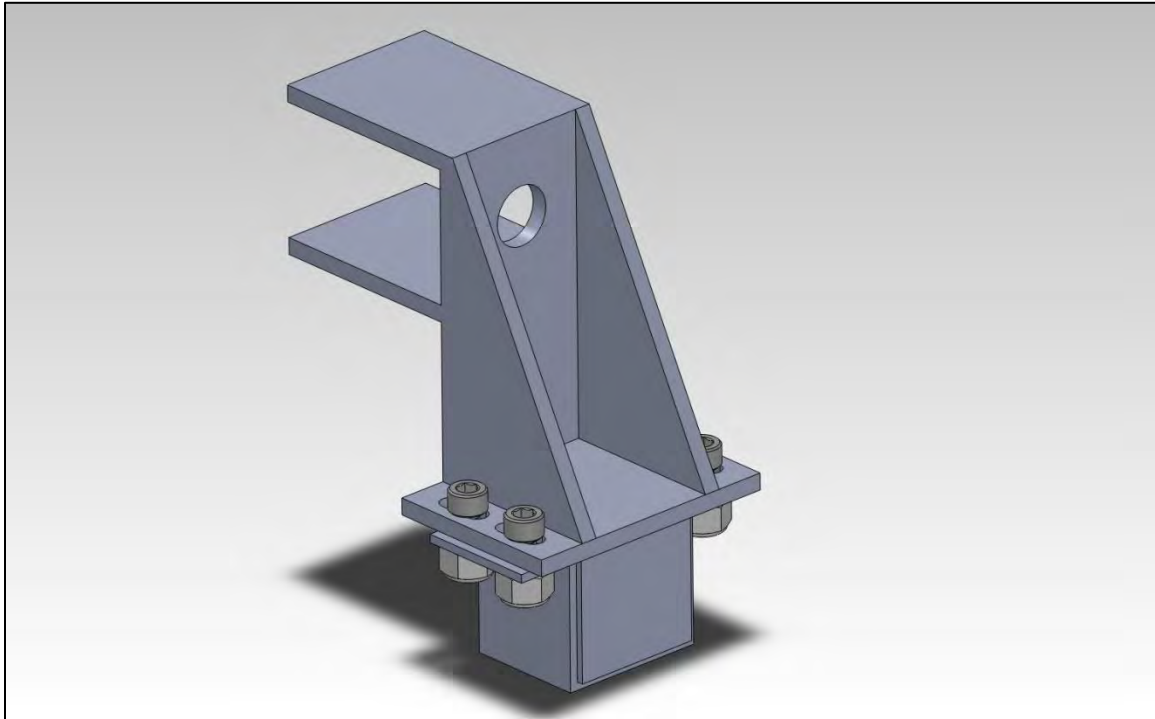
Side View without Rotor Disk



Isometric View of Magnet Mount/Placer



Isometric View of Magnet Mount/Placer



Exploded View of Magnet Mount/Placer Assembly

